Johannes W.F. Bekker
4231058 (TU Delft)
499930 (NTNU)

Radial Piston Pumps: Performance and Efficiency

Thesis Work

Delft, August 2019

Chair: Dr. ir. H. Polinder
Supervisor: Dr. ir. R.A.J. van Ostayen
Supervisor: Dr. ir. Zhen Gao
Supervisor: Dr. ir. A. Jarquin Laguna
Daily Supervisor: ir. J.P.A. Nijssen
Company Supervisor: Dr. ir. N.F.B. Diepeveen

Department of Offshore Engineering, TU Delft
Department of Maritime Engineering, NTNU

TU Delft

NTNU – Trondheim
Norwegian University of
Science and Technology

Preface

This thesis work is done as partial fulfillment of my studies, the European Wind Energy Master, Offshore track, for which the Norwegian University of Science and Technology (NTNU) awards the title M.Sc. Technology - Wind Energy, and for which the Delft University of Technology (TU Delft) awards the title M.Sc. Offshore Engineering. This thesis work has been a part of my mandatory graduation project which I carried out in Delft in the spring semester.

The work is done in cooperation with Delft Offshore Turbine B.V. (DOT), which offered me a place to work and support while I was working on this project. I would like to express my gratitude to them for the help and hospitality I have received over the past months. Special thanks to Dr. Ir. Niels F.B. Diepeveen, my supervisor at DOT, for the received guidance. I would like to thank Dr. Ir. Zhen Gao for helping me in Norway to find a thesis subject, and all of the support I've received since. I would also like to thank my supervisors at the TU Delft, Dr. Ir. Henk Polinder, Dr. Ir. R. van Ostayen, Dr. ir. Antonio Jarquin Laguna and PhD. Candidate ir. Joep P.A. Nijssen, for the supervision and help provided.

Furthermore I would like to thank the people with which I had the pleasure to share this experience over two years in three different countries. In particularly Wichert, Jelle, Matthijs, Sara and Sanne. We always managed to motivate each other to produce to the best of our abilities, and shared welcome company during the dark Scandinavian months.

Delft, 15-08-2019

Johannes W.F. Bekker

Abstract

The modeling method for the performance of positive displacement pumps of hydraulic pumps is based on collecting operational data of the pump for its operational envelope and using equations with empirical fitting parameters and fit these equations to the data. This way values for the fitting parameters are obtained, with which the equations can be used as model for the operating performance of this specific pump. By implementing this modelling method no information about the contribution of each component present in the pump to the performance losses is obtained. A model which analyzes each component and estimates its contribution to the total power losses would be beneficial in the design of pumps. Therefore the answers to the following research questions are sought after in this work:

- What are the components critical to performance within hydraulic pumps?
- To what accuracy can a component-wise, analytical model for pump performance be created?
- How sensitive to certain parameters used in the equations is the model?
- What are the possibilities of implementing this model into pump design?

After the pump system was analyzed and the internal interactions found, the components which effect pump performance the most were identified. These include bearings, rollers, seals, springs, valves and leakage flow which is dependent on gap size, piston movement and viscosity of the hydraulic fluid. For these components analytical equations are presented which are incorporated in the model.

The accuracy of the model is tested by comparing its results to test data of an experimental camring driven radial piston pump. The model predicts leakage flow to an average difference of 3% relative to the data, but outliers up to 49% for high pressures and -35% for low pressures are observed. Input torque is predicted to an average difference of -19% relative to the data. This difference is mainly caused by the inaccuracy of the predictions below 30 bar operating condition, where outliers up to -61% are observed. These results are compared to an empiric modelling method and are found to be more accurate for leakage flow for the entire operational envelope, yet on average less accurate for input torque.

The sensitivity of the model to certain parameters is tested. The parameters investigated are the rolling resistance coefficient of rollers and bearings, bearing lubricant viscosity, hydraulic fluid temperature, piston-cylinder alignment and the corresponding forces resisting piston motion and the assumption of laminar leakage flow.

To show the possibilities of the model in pump design the rollers and appurtenant bearings present in the pump are replaced with hydrostatic bearings. The design is discussed and a hydrostatic bearing with an orifice restrictor is designed of which implementation will approximate the total efficiency of the pump with rollers. The Reynolds number of the flow necessary is found to be too high for capillary restrictors. To approximate the same total efficiency for each operating condition the average bearing flow is found to be 0.0016 L/s, which corresponds to an average fluid film height of 12 μm. The orifice restrictor diameter which allows this flow is found to equal 0.24 mm.

This work shows the possibilities of such a model, yet there is plenty room for improvement of the accuracy of the predictions made. Recommendations to this end are given in the conclusion and recommendations of the report.

Contents

Chapter 1

Introduction

1.1 Background

To meet the global demand for renewable energy the concept wind energy is more and more utilized. Bigger and better wind turbines are being developed and wind farms are popping up everywhere, both onshore and offshore. Wind turbines utilize the wind to create electricity. Multiple different wind turbine concepts have been developed, but the only one that is being used now for commercial purpose is the horizontal axis wind turbine (HAWT). Within this type of wind turbine, two different drivetrain types are being utilized; the gearbox drivetrain and the direct drivetrain. Other types of drivetrains are under development and might prove promising for commercial use in the future. This work focuses on an alternative to those drivetrains, the hydraulic drive train.

1.2 Hydraulic drive train

An alternative to the direct and gearbox drivetrains could be the hydraulic drivetrain. This concept utilizes the torque and rotation of the wind turbine blades to power a pump which pressurizes a hydraulic fluid. This pressurized fluid can consequently be used to generate electricity.

One of the obstacles for designing this drivetrain is the operational conditions to which the pump will be exposed. The wind turbine blades transfer high torque but slow rotational speed to the pump present in the wind turbine nacelle. New designs are necessary to realize this type of drive train.

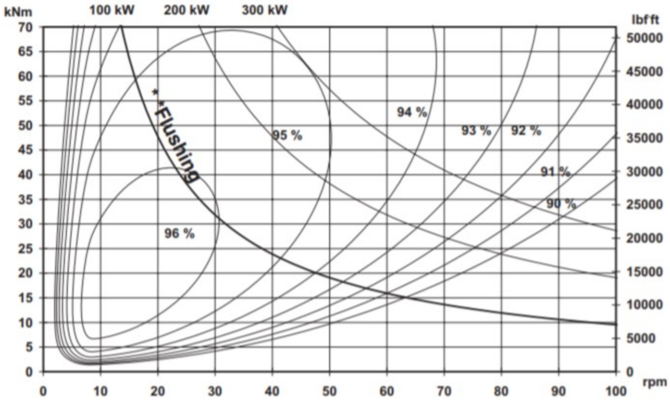

Figure 1.1: The efficiencies of the Hägglunds CA 210 motor throughout it operational envelope [1]

Industry has already shown that it is possible to design a high torque, low rotational speed pump with high efficiency. The radial piston pump/motor CA 210 developed by Hägglunds, shown in figure 1.2, for example. Figure 1.1 above shows the efficiencies of the pump at different operating conditions. It is seen that high efficiencies are obtained at low rotational speeds, which is necessary for the hydraulic drive train concept. Also, figure 1.3 shows that these kind of pumps are already coming near the high rated powers close to the operating conditions of wind turbines.

Figure 1.2: The Hägglunds radial piston pump/motor [2]

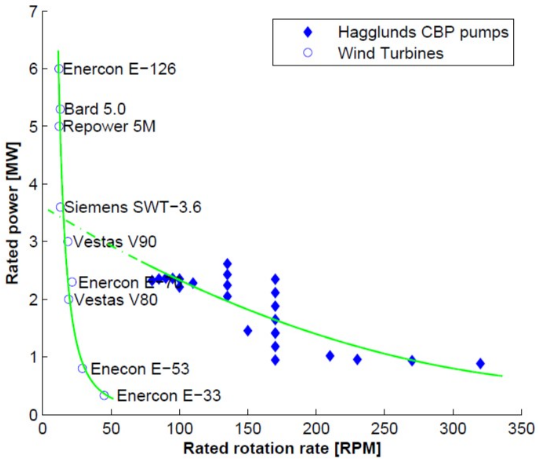

Figure 1.3: Pumps developed by Hägglunds tend towards higher rated power at lower rotation speeds [3]

1.3 Radial piston pumps

Radial piston pumps can be camshaft driven or camring driven. The basics of piston pumps are discussed briefly and some examples of radial piston pumps are given. Then the radial piston pump used in this work is discussed more thoroughly.

1.3.1 Basics of radial piston pumps

Two different concepts for preventing backflow are discussed. Backflow is an unwanted flow in reverse direction. The first principle works as depicted in figure 1.4. A piston is forced up and down into an cylinder. When the piston is moving to the left side of the cylinder in figure 1.4, the cylinder is filled with water from the inflow line with feeding pressure. The high pressure in the discharge line forces the check valve shut so that no water from the high pressure discharge line will flow back into the cylinder. The checkvalve is in this figure represented as a ball check valve, where a ball is forced into the open or closed position in the valve, but different types of checkvalves exist.

When the piston is moving to the right in figure 1.4, the high pressure in the cylinder forces the checkvalve to the inflow line shut. The water is forced under high pressure into the discharge line.

Furthermore, leakage between the piston head and the cylinder wall occurs. The magnitude of this leakage mainly depends on the gap size between the piston head and the piston, the hydraulic fluid used and the pressure reached in the cylinder. This leakage flow has to be removed, and therefore a leakage line is depicted on the left side of the cylinder.

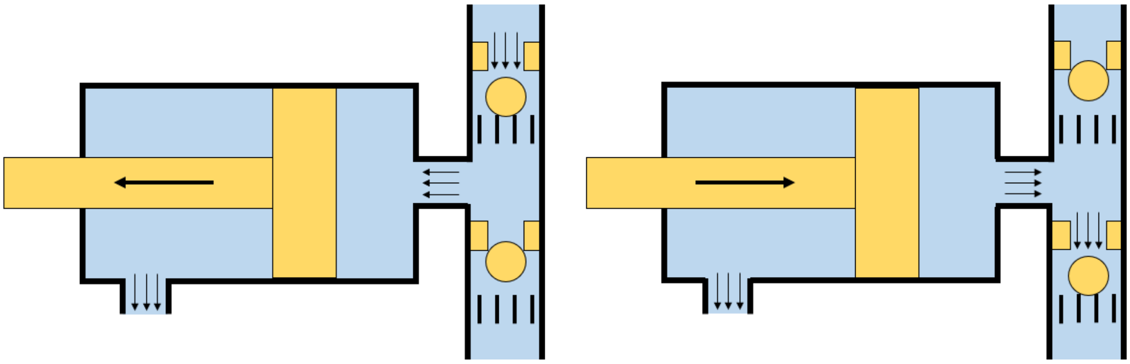

Figure 1.4: The working principle of a piston-cylinder configuration in a piston pump

Another way to prevent water from flowing back into the inflow line is by using a port plate. In figure 1.5 an axial piston pump with a port plate is presented. Through rotation of the input shaft the pistons rotate and cycle between the two positions depicted. During this rotation, the cylinders move over the port plate, which is seen on the right of the image. The two ports seen are the inflow and discharge ports. The inflow port feeds hydraulic fluid to the cylinder at feeding pressure, and in the discharge port this fluid is extruded at high pressure. With this solution check valves are not necessary. In addition to leakage between the piston and cylinder walls this solution introduces extra internal leakage between the cylinder block, being the block driven by the input shaft containing the pistons, and the port plate.

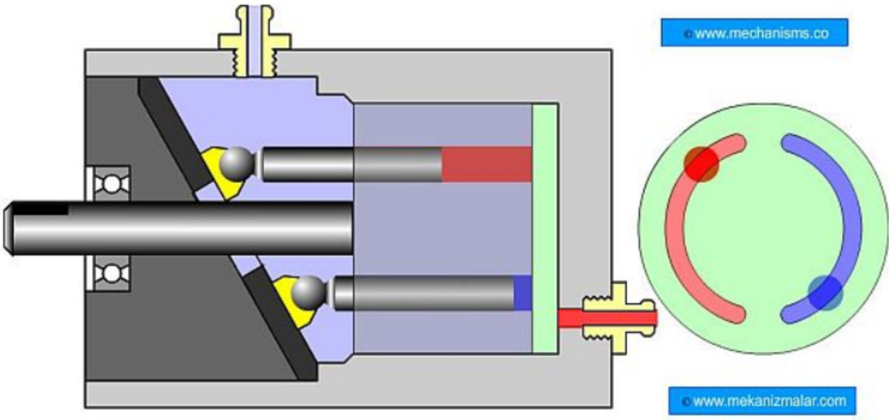

Figure 1.5: Axial piston pump with a port plate preventing backflow [4]

The difference between radial piston pumps and other types of piston pumps is the orientation of the pistons. In a radial piston pump, the pistons are distributed radially around the shaft in the middle of the pump.

How a rotation is transferred to the translational motion of the pistons, depends on the pump. One type is shown in figure 1.6. The pump depicted here is a camshaft driven radial piston pump. The pistons are forced into motion because the driving shaft has an eccentric shape.

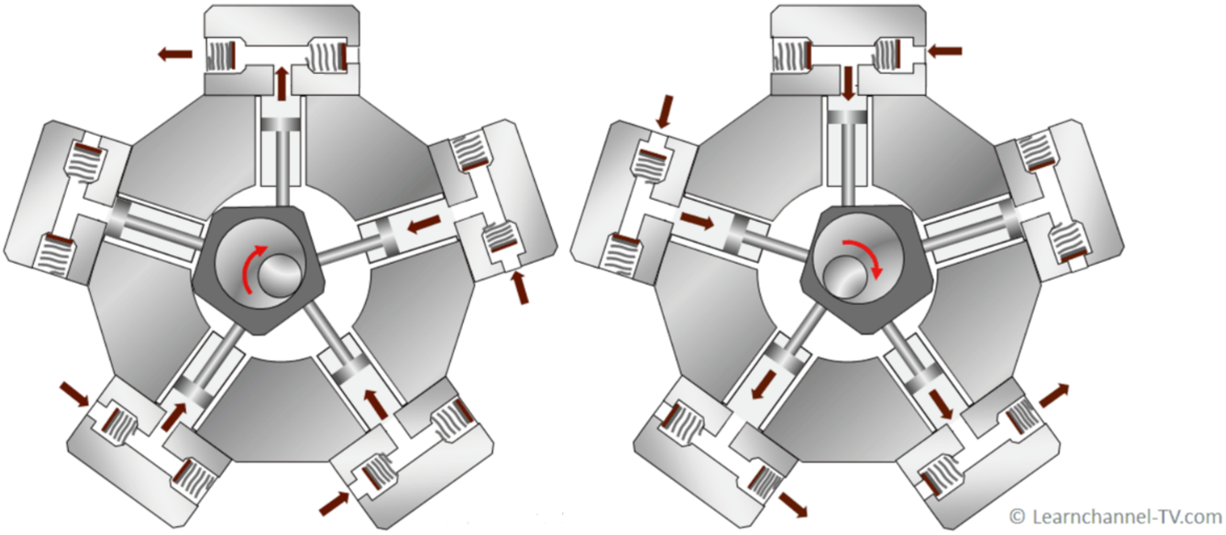

Figure 1.6: Overview of the inner working of an camshaft driven radial piston pump [5]

Another way of transferring motion to the pistons is by having an eccentric camring around the pistons. This type of pump is depicted in figure 1.7 below. The inflow and discharge lines are now in the center of the pump instead of on the outside. The pistons are guided over the sinusoidal shape of the camring by rollers, which transfers the rotational pump motion into the translational piston motion.

Also, the pump depicted in figure 1.7 is not driven by the axial shaft but by the camring. This pump however would also work if it was driven axially.

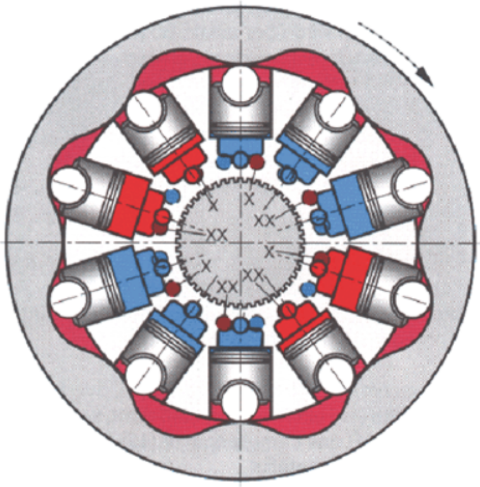

Figure 1.7: Schematic view of the inner working of a camring driven radial piston pump [6]

The Hägglunds radial piston pump/motor in figure 1.2 works with an camring and is driven by an axial shaft, and without checkvalves. It utilizes a system like the port plate which is presented in figure 1.5 for an axial piston pump, modified to work for a radial piston pump. Figure 1.8 shows a cross section of the Hägglunds with its components named.

The cylinder block, indicated with number 4, is stationary and contains the inflow and discharge lines. The distributor, indicated with number 3, rotates and draws water from the inflow line and extrudes water into the discharge line. Due to this rotation the cylinders are alternately exposed to the inflow and discharge line. This distributor is designed so that a inflow line crosses a cylinder when it is filling up with water and a discharge line crosses the cylinder when it is extruding water.

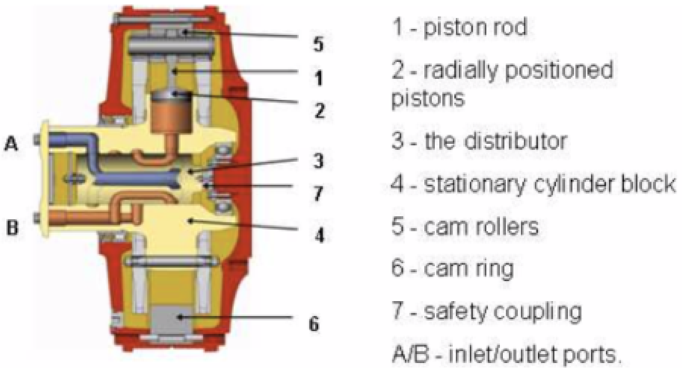

Figure 1.8: Cross section of the Hägglunds radial piston pump/motor [2]

1.3.2 The DOT camring driven radial piston pump

The type of radial piston pump used in this work is a camring driven radial piston pump. This pump is designed by Delft Offshore Turbine B.V. (DOT) for use as hydraulic drivetrain in an offshore wind turbine. A cross section of a part of this experimental camring driven radial piston pump designed by DOT is presented in figure 1.9.

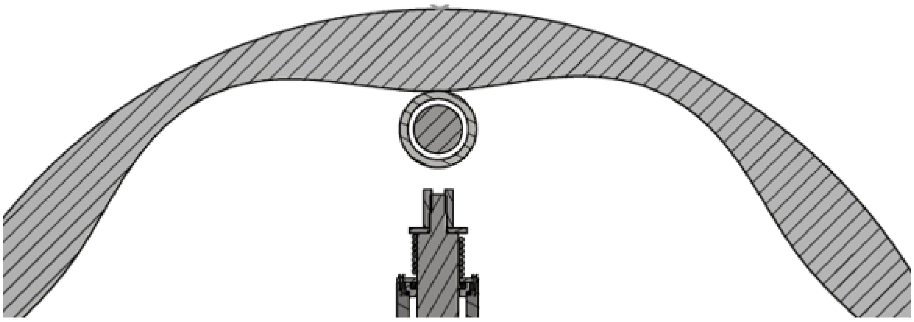

Figure 1.9: Cross section of part of a camring and a roller of a camring driven radial piston pump

The eccentric camring is rotated by an input shaft with a certain rotational speed and torque. Due to this rotation the piston seen in the figure is forced into a translational motion through the roller that move over the camring.

Because of the shape of the camring the rollers are also subject to an unwanted side force perpendicular to the piston axis. This side force is mitigated by the side force mitigation (SFM) system developed by DOT. This system contains rollers which mitigate the side forces by which friction or jamming between the piston and cylinder surfaces is prevented. Due to confidentiality the exact working of this system cannot be presented.

Furthermore the checkvalves used in the system which prevent backflow are of the ball checkvalve type, as visualized in figure 1.4. The DOT pump can be seen in figure 1.10 below.

Figure 1.10: A picture of the DOT pump connected to its test bench

1.4 Proposed new model for use in pump development and approach taken

The total performance of a pump can be described by two segments; the volumetric efficiency and the mechanical efficiency. The volumetric efficiency describes the power losses that result due to internal leakages and compressibility of the fluid. The mechanical efficiency describes the power losses that result due to fluid shear and internal friction. The total efficiency is found by multiplying the volumetric efficiency with the mechanical efficiency.

To analyze the volumetric, mechanical and total efficiency of a pump a model of the performance can be created, but there are two problems with the state of the art modelling methods used for pumps. In order to create the model, a physical pump is necessary for which test data needs to be collected. This data is then used to fit equations with empiric fitting parameters to. This way the empiric parameters are obtained with which the empiric equations best approximate the actual performance of the pump, but there is no way of predicting those empiric parameters without having test data. Thus there is no way of predicting the pump performance in the design phase, before the pump is actually built.

Another problem is the identification of components which are critical to the pump performance. With the fitting method, the fitting parameters get assigned a value for which the equation best approximates the test data. Yet they say nothing about the contribution of each component to performance reduction. To maximize the efficiency of a pump it would be beneficial to have an overview of the estimated power loss contributions of each component. This way it will be simpler to determine where the greatest opportunities lie for efficiency improvements.

To this end the following research questions are investigated in this work:

- What are the components critical to performance within hydraulic pumps?

- To what accuracy can a component-wise, analytical model for pump performance be created?
- How sensitive to certain parameters used in the equations is the model?
- What are the possibilities of implementing this model into pump design?

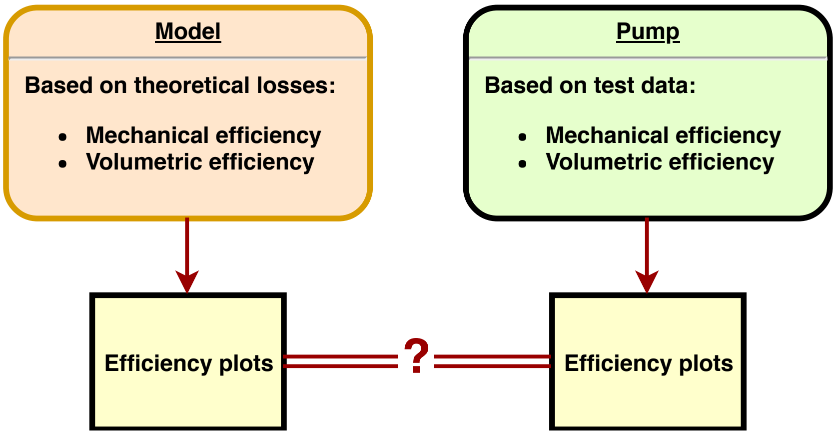

Figure 1.11: Comparing efficiencies obtained analytically and by testing to investigate model accuracy

To answer the research questions, first a literature review has been performed into pump modelling and components present in hydraulic pumps. Based on this review, the following structure is followed to reach the research goals.

In chapter 2 the pump used for this work, the DOT pump, is analyzed. All of the components present in the pump are identified and their interactions depicted. Also the hydraulic phenomena are identified, like flow resistance and leakage flow. Each of these components and phenomena are discussed thoroughly and analytical equations for estimating their losses are presented.

Chapter 3 is built up as a paper in which the model is presented and discussed. Essential equations in the model are repeated and explained. In addition to this model, a way to fit the model to test data to find some unknown parameters is introduced. Furthermore a state of the art, empiric modelling method is introduced to test the model and the model using fitted parameters to. All three methods are compared to the leakage flow and input torque of the test data, after which the findings are discussed.

In chapter 4 the sensitivity of equations used in the model to certain parameters are discussed. First the contribution of each component to the total power loss is presented to point out which components are the most important and should be investigated more thoroughly. Then equations which contain parameters of which their value is uncertain are discussed and the difference in outcome for altering values for those parameters are depicted.

In chapter 5 the potential of this model is demonstrated by substituting a component in the DOT pump. The camrollers with bearings inside can potentially be replaced by hydrostatic bearings. The design steps of the hydrostatic bearing are explained and constraints are found for which implementing the hydrostatic bearing will actually improve the performance of the pump.

In chapter 6 the conclusions of each chapter are summed up to form the final conclusion of this work. Consequently, recommendations are made for further research and improvements

The Appendix contains information and figures which were not directly important for the structure of the report but are practical for more in depth knowledge of how the model is built up. The following points are appended:

- Checkvalve testing
- DOT pump testing
- Testdata processing
- Model plots

Chapter 2

Identification of Performance Critical Components in Piston Pumps

2.1 State of the art performance models in pump development

The performance of a pump can be divided into volumetric efficiency and mechanical efficiency, which combine to equal the total pump efficiency. For the efficiency calculations, the power flows within the pump system need to be known. These are depicted schematically in figure 2.1 below.

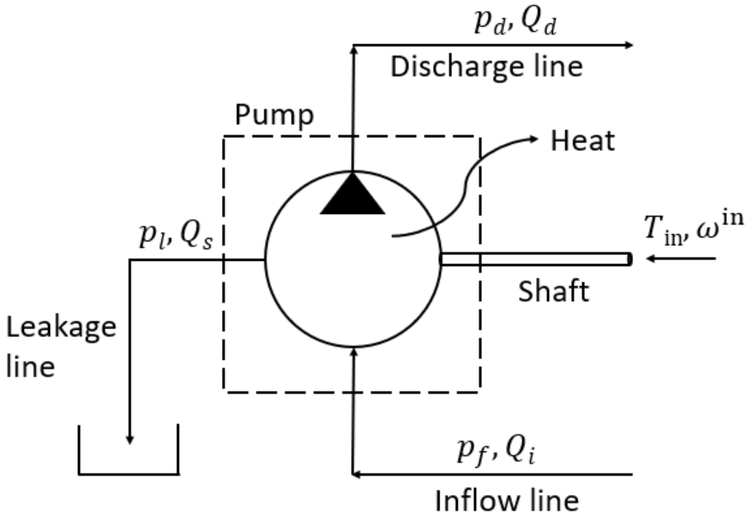

Figure 2.1: A schematic overview of the power flow to and from a pump [7]

With these power flows known, the following calculations can be performed [7]. The volumetric efficiency is found with (2.1) with Q_d [m^3/s] as discharge flow, Q_i [m^3/s] as ideal discharge flow or feed flow, Q_s [m^3/s] as the leakage flow, D_p [m^3/rad] as ideal volumetric displacement and ω^{in} [rad/s] as input shaft angular frequency.

$$\eta_v = \frac{Q_d}{Q_i} = \frac{Q_i - Q_s}{Q_i} = \frac{D_p \omega^{in} - Q_s}{D_p \omega^{in}} \tag{2.1}$$

The mechanical efficiency can be expressed as in (2.2) with T_{in} as the torque of the input shaft and Δp_p as the pressure difference between the inflow and discharge lines.

$$\eta_m = \frac{D_p \Delta p_p}{T_{in}} \tag{2.2}$$

The total efficiency η_{tot} can consequently be found with the volumetric and mechanical efficiencies as in (2.3).

$$\eta_{\text{tot}} = \eta_m \eta_v \tag{2.3}$$

To calculate these efficiencyies measurements are performed for different operational conditions. With those measured values (2.1), (2.2) and (2.3) are used to calculate the efficiencies at those operational conditions.

In the literature study, several empiric equations have been proposed. These are used to fit the data to the fitting parameters in order to get a working model. The empiric equation for the volumetric efficiency η_v used in this work equals the following [7]

$$\eta_v = 1 - C_l \frac{\Delta p_p}{\mu \omega^{\text{in}}} - C_t \sqrt{\frac{\Delta p_p}{\mu \omega^{\text{in}}}} \tag{2.4}$$

where C_l accounts for the compressibility of the hydraulic fluid and low Reynolds number leakage and C_t is a factor which is determined for high Reynold number leakage. The empiric mechanical efficiency equation can be taken to equal the following

$$\eta_m = 1 - C_{st} - C_c \frac{\mu \omega^{\text{in}}}{\Delta p_p} - C_h \sqrt{\frac{\mu \omega^{\text{in}}}{\Delta p_p}} \tag{2.5}$$

where C_{st} stands for starting torque losses, C_c accounts for the torque losses caused by Coulomb friction which are correlated to the loads in the pump and C_h is a factor which is used to approximate the hydrodynamic torque losses which are the result of fluid shear.

Yet with this modelling method a lot of information is lost. Each component in the pump operates at a certain efficiency and thus stands for some efficiency loss of the complete pump. The fitting parameters say nothing about the contribution of each component present in the pump to the performance losses of the pump. Therefore, in this chapter, an analysis of the pump system is performed to identify all components critical to pump performance and their interaction with each other inside the system.

2.2 Analysis of the pump system

Many components in the system interact with each other, meaning that a false approximation of one component will lead to a false approximation of the components which interact with this component. To show in which order and how different components in the pump interact with each other, a schematic overview of the pump is presented in figure 2.2 below and the interactions discussed.

Through the drive shaft the camring is rotated with in input angular velocity ω_{in} [rad/s] and torque T_{in} [Nm]. The camring is supported by two internal bearings. These bearings are loaded by the camring weight with a normal force F_n^b [N] and rotated with angular velocity ω^b, which equals ω^{in}. Power P_b [W] is lost in the bearings.

The camring induces a normal force F_n^r [N] on the rollers and gives them rolling velocity v_r^r [m/s]. Power P_r is lost due to rolling resistance. The bearings present in the rollers are loaded with a normal force F_n^b and rotated with angular velocity ω^b, which causes a power loss P_b. The side force mitigation system in the DOT pump also consists of rollers and bearings. The rollers are loaded with a force F_{side} and roll with the vertical velocity of the piston, U^p [m/s], which cause rolling loss P_r. The bearings present are loaded with a normal force F_n^b and rotate with an angular velocity ω_b, causing a power loss P_b.

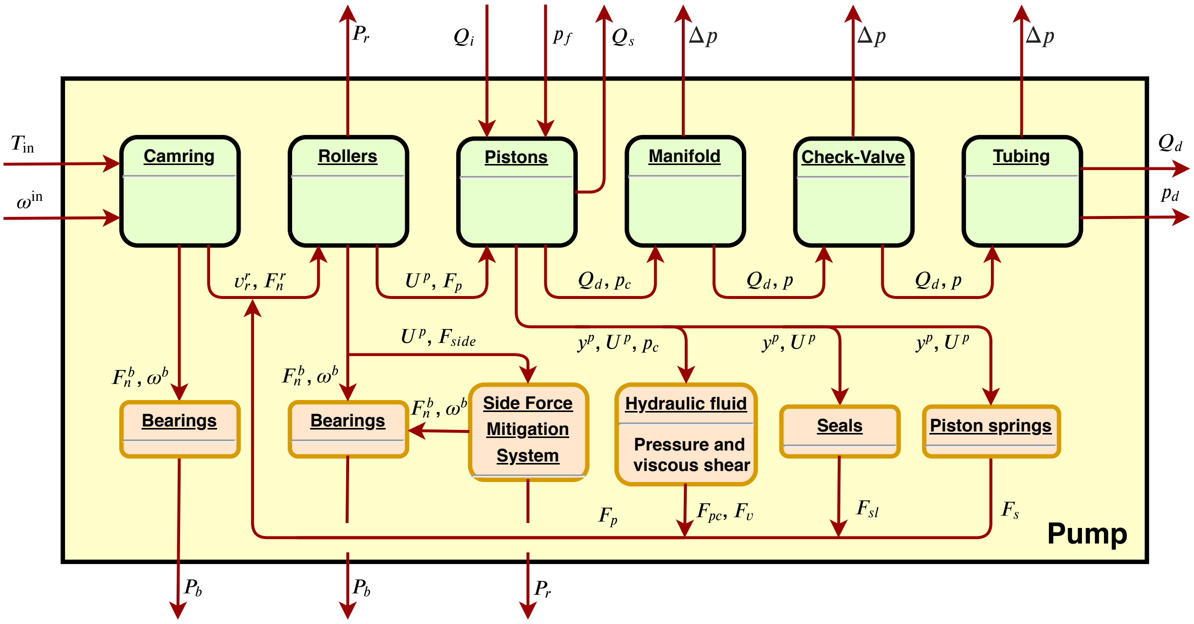

Figure 2.2: A schematic overview of all the components and their interaction in the DOT pump

Through the rollers the rotation of the camring is transferred to the translational motion of the pistons. The translational velocity U^p is given to the pistons, which requires piston force F_p to be overcome. The cylinders are filled with water at flowrate Q_i [m^3/s] with feeding pressure p_f [Pa], and during operation leakage flow Q_s [m^3/s] occurs. The resistance to piston motion F_p is built up out of pressure force F_{pc} [N] and viscous shear force F_v [N] of the hydraulic fluid, seal friction F_{sl} [N] and resistance from the piston springs F_s [N]. These are determined with the cylinder chamber pressure p_c [Pa], piston location y^p [m] and piston velocity U^p. The sum of these forces is fed back to the connection between the camring and rollers, since F_p together with camring-roller angle α determines roller normal force F_n^r.

Discharge flow Q_d [m^3/s] with chamber pressure p_c leaves the cylinder to the manifold. Here a pressure drop Δp occurs due to flow resistance. The same discharge flow goes to the check valves at a new pressure p. In the check valves, another pressure drop occurs due to flow resistance. Lastly, in the tubing another pressure drop occurs with the same discharge flow. Flow leaves the pump system at discharge flow Q_d with discharge pressure p_d [Pa].

With the components and their interactions in the pump system known, these components are discussed more thoroughly and their modelling methods are proposed.

2.3 Rollers

The movement of the pistons of the test pump inside the cylinders is caused by a rotating camring which is connected to the rotor shaft with an inner sinusoidal profile over which the end of the piston moves guided by rollers. This way the piston follows the sinusoidal movement of the camring which translates back into vertical movement of the piston. High forces will occur at the contact area of the rollers and the camring, since the fluid in the chamber will be forced into the high pressure line. The movement of the rollers over the camring will perform some work which means that it influences the performance of the pump. The energy lost in these rollers needs to be determined to determine the pump efficiency.

The work done by the roller moving over the camring can be described by the following

$$P_r = F_f^r v_r^r \tag{2.6}$$

in which P_r [W] is the performed work, F_f^r [N] is the rolling resistance and v_r^r [m/s] is the speed with which the roller moves over the surface of the camring [8]. The rolling resistance can be expressed as following [9]

$$F_f^r = F_n^r C_r^r \tag{2.7}$$

in which F_n^r [N] is the normal force between the roller and the surface and C_r^r [-] is the rolling resistance coefficient. These equations are quite simple and it is uncertain if they will suffice for the model. They are only dependent on the normal force F_n^r, velocity v_r^r and the rolling resistance coefficient C_r^r. A big assumption in using this equation will be the rolling resistance coefficient C_r^r. There is no mathematical way to determine this coefficient, it has to be obtained by testing. Since the losses increase linearly with increasing C_r^r, with a doubling of the rolling resistance coefficient resulting in double the losses P^r, a wrong coefficient C_r^r may have massive impact on the accuracy of the model. How much this will impact the model depends on the contribution of the rollers to the total mechanical losses of the pump. Since the roller and camring are both made of steel, the first estimate is to use the rolling resistance of train wheels on rails, which equals $C_r^r = 0.001$ [10].

Something to consider for the test pump is that the force which is exerted on the roller by the camring changes constantly. The sinusoidal shape of the camring causes the angle the normal force makes with the piston shaft to change constantly. Since the vertical downward force in the piston should remain large enough to force the fluid into the high pressure line, the resultant force will vary. This means, the horizontal component of the normal force exerted on the roller will vary with the camring shape. The camring shape also forces the velocity of the rollers v_r^r to vary. The movement of the rollers over the camring will be further discussed in the modelling part.

A great uncertainty is to what temperature the rollers and camring will rise during operation. This is of importance since the rolling resistance coefficient C_r^r is dependent on temperature [9]. Rolling resistance decreases with increasing temperature. This does not necessarily means that a higher temperature is beneficial for the pump performance. Higher temperatures can change material properties which can cause components to damage more quickly. Materials are known to fail faster due to fatigue at higher temperatures ([11], [12]). The rolling resistance coefficient can also be dependent on the rolling velocity [9].

Furthermore it is of importance that the rollers will be able to endure the forces acted upon them. For this it is important to check that deformations under operational loading remain in the elastic regime. A method for this is found incorporating the curvatures and material properties of the two interacting objects [13].

First the effective modulus of elasticity $E^{'}$ is determined. This combines the modulus of elasticity of the two objects into one as in (2.8)

$$\frac{1}{E'} = \frac{1-v_1^2}{2E_1} + \frac{1-v_2^2}{2E_2} \tag{2.8}$$

with E as modulus of elasticity and v as the Poisson's ratio. Next off the effective radius R' should be determined. How this is determined depends on the shapes of the objects in contact. Two types of contact are depicted in figure 2.3 below.

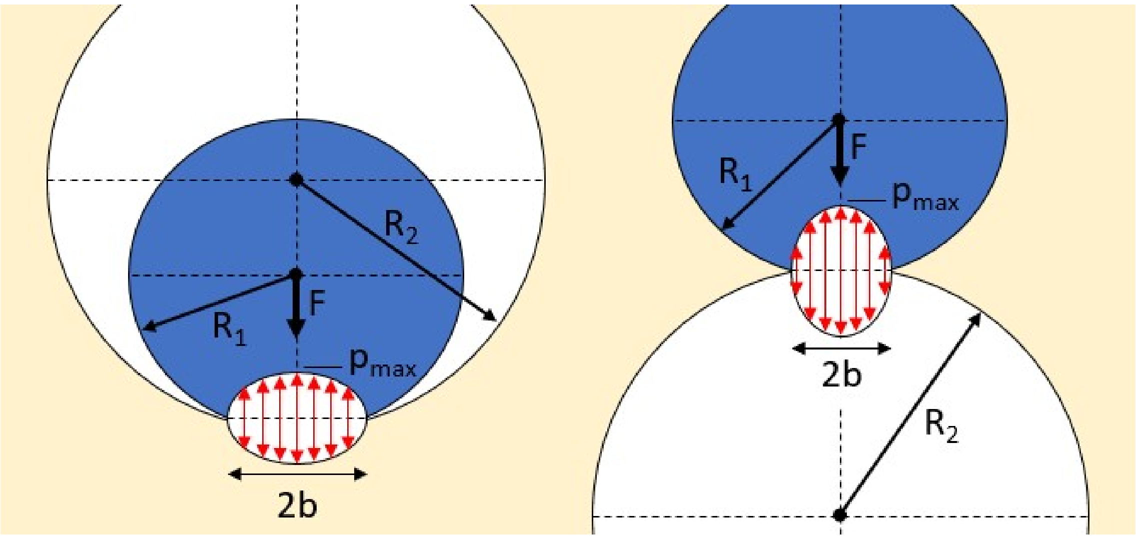

Figure 2.3: Nominal contact line of a concave surface (left) and of two cylinders (right)

The effective radius is determined using (2.9). For the scenario on the left side of image 2.3, with a concave contact surface, R_2 should be inserted as a negative value in (2.9). For the scenario at the right side of the image both R_1 and R_2 should be inserted positively.

$$\frac{1}{R'} = \frac{1}{R_1} + \frac{1}{R_2} \tag{2.9}$$

The nominal contact line equals $2b$ and is dependent on the effective modulus of elasticity and radius, the force with which the objects are forced together, F, and the length of the contact surface, l. Half of the nominal contact line b is found with (2.10).

$$b = 2\left(\frac{2}{\pi}\right)^{\frac{1}{2}}\left(\frac{F}{l}\right)^{\frac{1}{2}}\left(\frac{R'}{E'}\right)^{\frac{1}{2}} \tag{2.10}$$

The mean contact pressure between the two objects is then determined with (2.11).

$$p_m = \frac{F}{2bl} \tag{2.11}$$

The maximum contact pressure $p_{\max}$ is found in the middle of the contact line and correlates to the mean contact pressure p_m as in (2.12).

$$p_{\max} = \frac{4}{\pi} p_m \tag{2.12}$$

As the contact scenario on the left side of figure 2.3 will have a larger nominal contact line, force F is distributed over a larger area and thus the contact pressures will be lower than in the other scenario.

2.4 Pump bearings

Although bearings are designed to be as efficient as possible, they will still generate some heat during operation. To determine the efficiency of the pump system, the energy lost in the bearings need to be accounted for.

The heat generated by bearings is equal to the loss of power. Power equals to force times velocity or to torque multiplied with rotational speed. The power loss in bearings can be calculated as following

$$P_b = M^b \omega^b \tag{2.13}$$

with P_b [W] being the power loss, ω^b [rad/s] the rotation speed of the bearing and M^b [Nm] as the torque lost by the friction moment. How this friction moment is obtained depends on the type of bearing. In this section it is described how the torque loss in bearings can be estimated to calculate the corresponding power loss.

2.4.1 Bearings analyzed as rollers

The working principle of bearings are the same as that of rollers. The rolling elements present in the bearing, for example the cylinders in a cylindrical roller bearing, oppose a certain resistance against the rotation of the bearing. This resistance is caused by the cylinders resistance to rolling. Thus the resistance to rotation can be expressed with a rolling resistance coefficient. The following is found [14]

$$M^b = C_r^b F_n^b \frac{d^b}{2} \tag{2.14}$$

with C_r^b as the rolling resistance coefficient of the bearing, F_n^b the radial force exerted on the bearing and d^b the bearing bore diameter. The actual arm to find the moment is a little bit larger than the bore radius, $r^b = \frac{d^b}{2}$, but this is neglected. Figure 2.4 schematically shows the rolling forces due to rotation and the important geometries inside a caged cylindrical roller bearing.

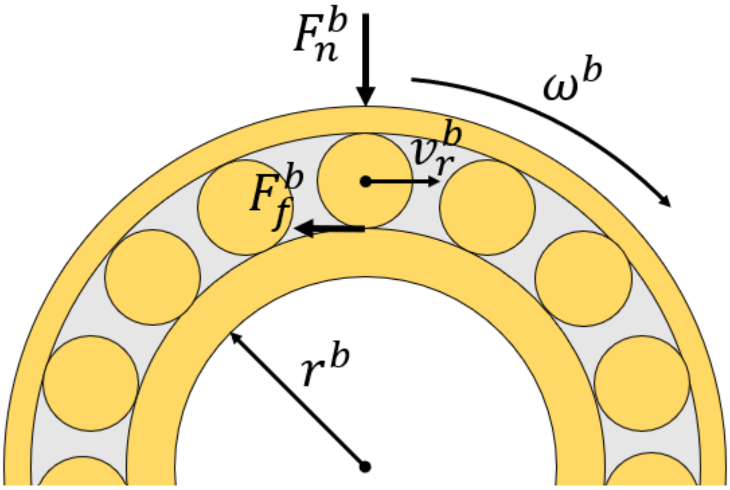

Figure 2.4: A simple schematic overview of the rolling forces and geometries in a caged cylindrical bearing

Radial force F_n^b is exerted on the outer housing, which transfers it to the rollers present in the bearing. If the outer housing is subject to rotation ω^b, it will cause the rolling elements to assume a velocity v_r^b. If pure rolling is assumed, that is without slip, this velocity of the cylinders will equal the velocity of the outer housing. Since there is no relative motion, no work is done here.

The inner housing seen in figure 2.4 is assumed to be stationary. Thus the rolling elements inside the bearing will have a velocity v_r^b relative to the inner housing, while the rolling elements are forced upon the inner housing with a certain force. Radial force F_n^b is divided upon some of the rolling elements present in the bearing, closest to where the load is exerted. Rolling resistance coefficient C_r^b in (2.14) represents the rolling resistance of all loaded elements combined, and multiplied with F_n^b equals rolling friction force F_f^b.

However, rolling resistance is not the only phenomenon causing resistance to the rotation of the outer housing. Slip between the housing and the rolling elements may occur, sliding occurs between the cage holding the elements apart and the elements and shearing of the lubricant between the bearing parts, among others. To account for all these types of power losses in the bearing, empiric equations have to be used to get a sensible estimation of the total power losses inside bearings. These empiric equations give an estimation of the torque lost by rotating the bearing, after which (2.14) can be used to calculate the corresponding rolling resistance coefficient C_r^b. Consequently (2.6) and (2.7) from the roller section can be used to determine the total power lost in the bearing.

Following it is explained how the empirical equations can be used to estimate the friction moment in ball bearings and cylindrical roller bearings ([15], [16]). The parameters used in this method are normally given by the manufacturer. In chapter 4 the sensitivity of the rolling resistance coefficient C_r^b to different operating conditions is discussed.

2.4.2 Ball bearings

The total friction moment M^b of a ball bearing under moderate speed and load conditions can be acceptably approximated by the sum of the load friction torque M_1 [Nmm] and the viscous friction torque M_v [Nmm]. This gives (2.15) for the total friction moment.

$$M^b = M_1 + M_v \tag{2.15}$$

The first component is the torque due to applied load, M_1. The method to calculate this is empirical and is dependent on bearing type specific constants. The following is found to calculate M_1

$$M_1 = f_1 F_B d_m \tag{2.16}$$

in which F_B [N] is the load on the bearing dependent on direction and magnitude of the applied load and d_m [mm] is the mean diameter of the bearing. Load F_B can be determined as following

$$F_B = 0.9F_a^b \cot(\alpha) - 0.1F_n^b \qquad \text{or} \qquad F_B = F_n^b \tag{2.17}$$

with F_a^b [N] and F_n^b [N] being the axial and radial load the bearing is subject to. The part of (2.17) yielding the higher load is used in further calculations.

Factor f_1 depends on the bearing design and the relative bearing load. It can be determined as following

$$f_1 = z(F_{st}/C_s)^y \tag{2.18}$$

in which F_{st} [N] is the static equivalent load, C_s [N] is the basic static load rating, and table z and y are bearing type specific constants. The values and types are listed in table 2.1.

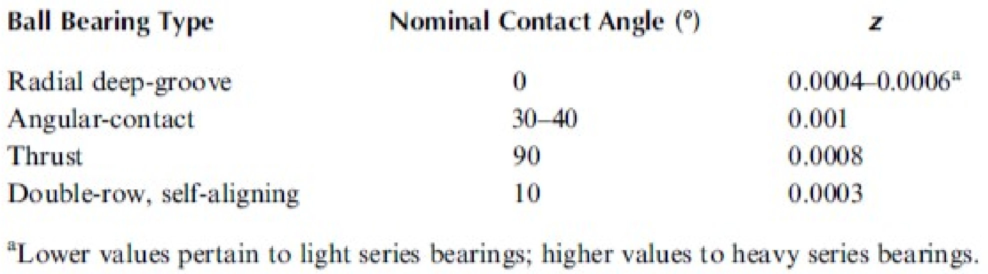

Ball Bearing Type	**Nominal Contact Angle (°)**	***z***	***y***
Radial deep-groove	0	0.0004–0.0006[a]	0.55
Angular-contact	30–40	0.001	0.33
Thrust	90	0.0008	0.33
Double-row, self-aligning	10	0.0003	0.40

[a] Lower values pertain to light series bearings; higher values to heavy series bearings.

Table 2.1: The values of y and z for different ball bearing types [15]

The value for C_s is usually provided by the manufacturer. The value of F_{st} can be determined by information that usually is provided by the manufacturer. With the data provided by the manufacturer F_{st} can be calculated as

$$F_{st} = X_s F_n^b + Y_s F_a^b \tag{2.19}$$

where constants X_s and Y_s can be picked from table 2.2 with bearing data that should be provided by the bearing manufacturer.

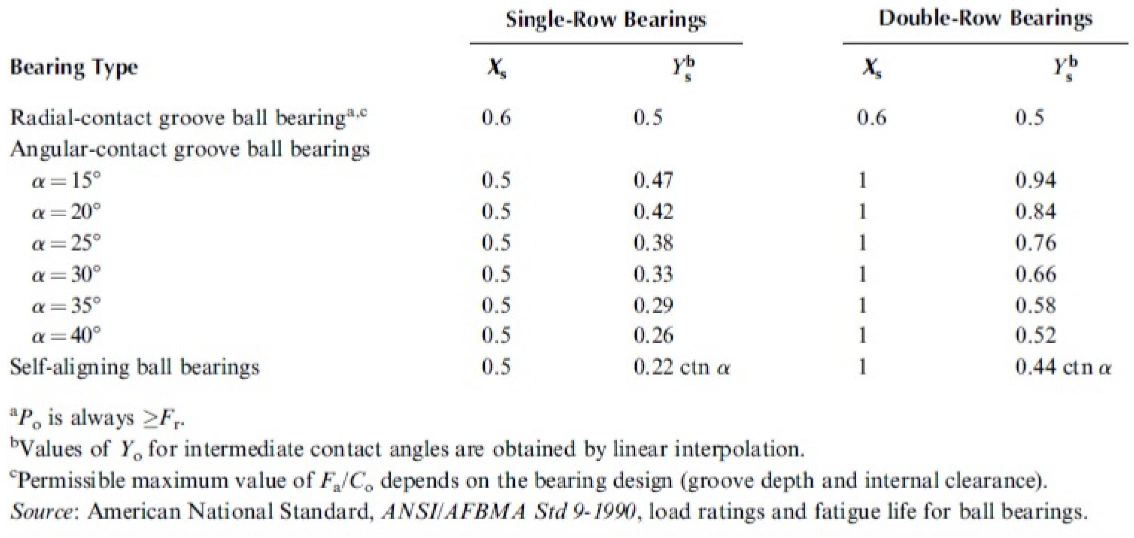

	Single-Row Bearings		Double-Row Bearings	
Bearing Type	X_s	Y_s^b	X_s	Y_s^b
Radial-contact groove ball bearing[a,c]	0.6	0.5	0.6	0.5
Angular-contact groove ball bearings				
$\alpha = 15°$	0.5	0.47	1	0.94
$\alpha = 20°$	0.5	0.42	1	0.84
$\alpha = 25°$	0.5	0.38	1	0.76
$\alpha = 30°$	0.5	0.33	1	0.66
$\alpha = 35°$	0.5	0.29	1	0.58
$\alpha = 40°$	0.5	0.26	1	0.52
Self-aligning ball bearings	0.5	0.22 ctn α	1	0.44 ctn α

[a] P_o is always $\geq F_r$.
[b] Values of Y_o for intermediate contact angles are obtained by linear interpolation.
[c] Permissible maximum value of F_a/C_o depends on the bearing design (groove depth and internal clearance).
Source: American National Standard, *ANSI/AFBMA Std 9-1990*, load ratings and fatigue life for ball bearings.

Table 2.2: The values of X_s and Y_s for different ball bearing designs [15]

The viscous friction torque M_v is dependent on the rotation speed of the bearing. Dependent on the rotational speed, either (2.20) or (2.21) is used.

$$M_v = 10^{-7} f_o (v_o n_b)^{2/3} d_m^3, \qquad v_o n_b \geq 2000\,\mathrm{cSt/min} \tag{2.20}$$

$$M_v = 160 \cdot 10^{-7} f_o d_m^3, \qquad v_o n_b \leq 2000\,\mathrm{cSt/min} \tag{2.21}$$

The kinematic viscosity is denoted as v_o [cSt] and f_o [-] is the bearing lubrication factor. Factor f_o is dependent on the type of ball bearing used and the type of lubrication. The different values of f_o can be found in table 2.3.

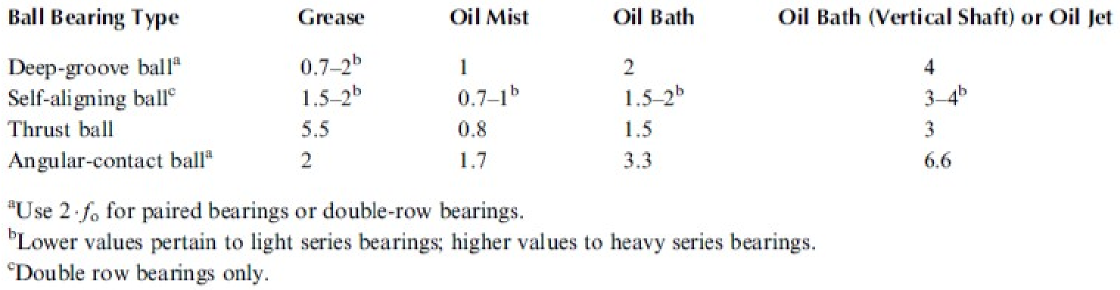

Ball Bearing Type	Grease	Oil Mist	Oil Bath	Oil Bath (Vertical Shaft) or Oil Jet
Deep-groove ball[a]	0.7–2[b]	1	2	4
Self-aligning ball[c]	1.5–2[b]	0.7–1[b]	1.5–2[b]	3–4[b]
Thrust ball	5.5	0.8	1.5	3
Angular-contact ball[a]	2	1.7	3.3	6.6

[a] Use $2 \cdot f_o$ for paired bearings or double-row bearings.
[b] Lower values pertain to light series bearings; higher values to heavy series bearings.
[c] Double row bearings only.

Table 2.3: The values of f_o dependent on bearing type and lubrication type [15]

2.4.3 Cylindrical roller bearings

The friction moment for cylindrical roller bearing consists of the same components as for ball bearings, with the addition of end-flange friction torque M_f [Nmm] which is induced by axial loads. Thus the total friction moment can be expressed as in (2.22).

$$M^b = M_1 + M_v + M_f \tag{2.22}$$

The torque due to applied load, M_1, can be calculated as for ball bearings, according to (2.16). The load F_B is determined slightly different as in (2.23) below.

$$F_B = 0.8F_a^b \cot(\alpha) \qquad \text{or} \qquad F_B = F_n^b \tag{2.23}$$

Also, f_1 is found by selecting it from table 2.4 based on the bearing properties.

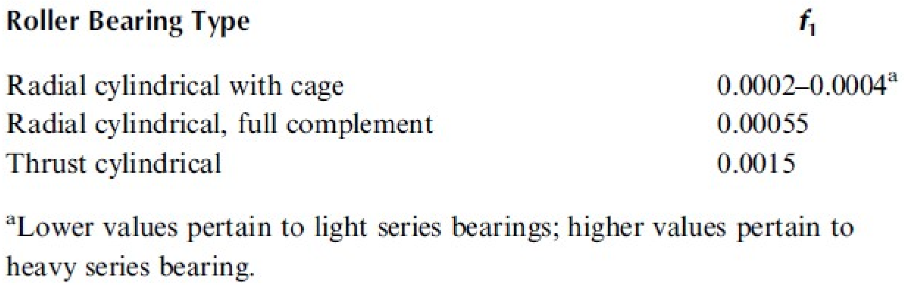

Roller Bearing Type	f_1
Radial cylindrical with cage	0.0002–0.0004[a]
Radial cylindrical, full complement	0.00055
Thrust cylindrical	0.0015

[a] Lower values pertain to light series bearings; higher values pertain to heavy series bearing.

Table 2.4: Values for f_1 for different cylindrical roller bearing types [15]

Viscous friction torque M_v is also determined using the same equations as for ball bearings, (2.20) and (2.21). The necessary bearing lubrication factor f_o can be found in table 2.5 below.

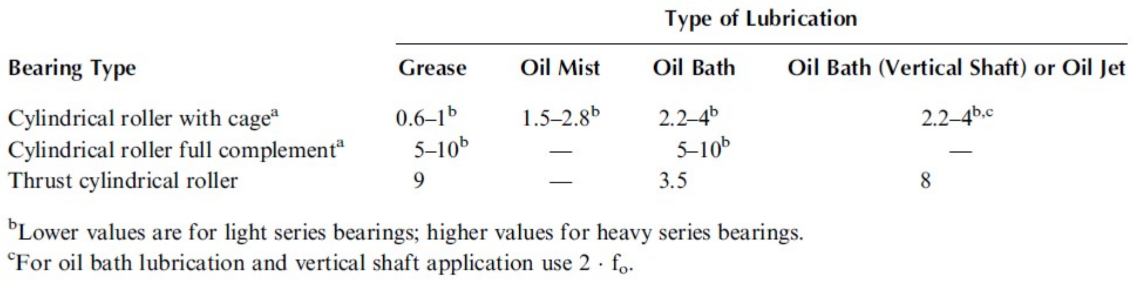

	Type of Lubrication			
Bearing Type	Grease	Oil Mist	Oil Bath	Oil Bath (Vertical Shaft) or Oil Jet
Cylindrical roller with cage[a]	0.6–1[b]	1.5–2.8[b]	2.2–4[b]	2.2–4[b,c]
Cylindrical roller full complement[a]	5–10[b]	—	5–10[b]	—
Thrust cylindrical roller	9	—	3.5	8

[b] Lower values are for light series bearings; higher values for heavy series bearings.
[c] For oil bath lubrication and vertical shaft application use $2 \cdot f_o$.

Table 2.5: Values for f_o for different cylindrical roller bearing types with different types of lubrication [15]

The last component to be determined is the roller end-flange friction torque M_f. This can be done by using (2.24).

$$M_f = f_f F_a^b d_m \tag{2.24}$$

Values for factor f_f can be found in table 2.6 below. Do note that this friction torque is due to friction between the rollers and one flange of the bearing, induced by axial loads. In absence of axial loads, thus if $F_a^b = 0$ [N], the bearing friction torque equals $M_f = 0$ [Nmm].

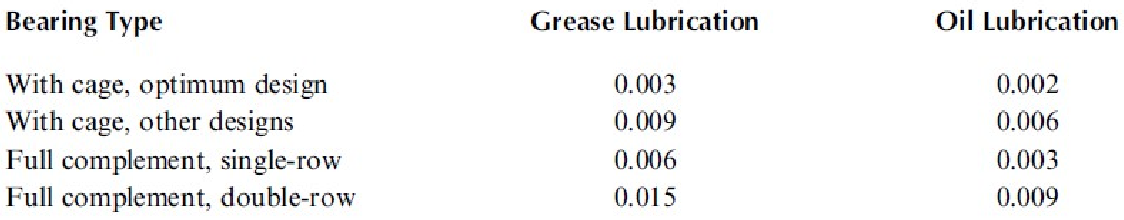

Bearing Type	Grease Lubrication	Oil Lubrication
With cage, optimum design	0.003	0.002
With cage, other designs	0.009	0.006
Full complement, single-row	0.006	0.003
Full complement, double-row	0.015	0.009

Table 2.6: Values for f_f for different cylindrical roller bearing types with different types of lubrication [15]

2.5 Pressure drop in check valves

The DOT high pressure pump utilizes two check valves internally. One which prevents the water to flow into the low pressure line when the cylinder is being pressurized, and one to prevent water to flow from the high pressure line back into the cylinder when the cylinder is being filled with water. The pressure drop for both ends is of importance. The pressure drop at the inlet should be known to make sure the pressure at the inlet is sufficient to fill the chambers with water. The pressure drop at the outlet causes a drop in pump efficiency which is of importance for this research.

The reason of this pressure drop is because the valve forms an obstacle which induces a resistance to flow. To overcome this resistance, energy is taken from the fluid, and thus decreasing the system efficiency. To determine the pressure drop over the check valves, tests have to be performed. Assuming that the pressure drop is only dependent on the flow rate [17], the following equation correlating the pressure drop with the flow rate is found [18]

$$\Delta p_{cv} = S_g \frac{(Q^{cv})^2}{K_v^2} \tag{2.25}$$

in which Δp_{cv} [Pa] is the pressure drop, S_g [-] is the specific gravity of the fluid, Q^{cv} [m^3/s] is the flow rate through the valve and K_v [-] is the valve flow coefficient. Flow characteristic K_v is a constant for a valve, which can be found by testing the valve. By measuring the pressure drop over the valve for a certain flow, (2.25) can be used to calculate K_v. With K_v known (2.25) can be used in the efficiency model to incorporate the pressure drop over the check valves for variable values of the pump flow rate.

The specific gravity S_g is the density of a substance normalized to another reference substance. The most common substance used for this is the density of water at a temperature of 4^oC. In the test set-up for the pump, fresh water will be used. Since the density of substances change with alternating temperature, the specific gravity will also change with alternating temperature. Therefore it should be checked how big the influence of temperature will be on the specific gravity of water, to check in what magnitude this could effect the pressure drop. The dependency of the specific gravity of fresh water and temperature is depicted in figure 2.5 below.

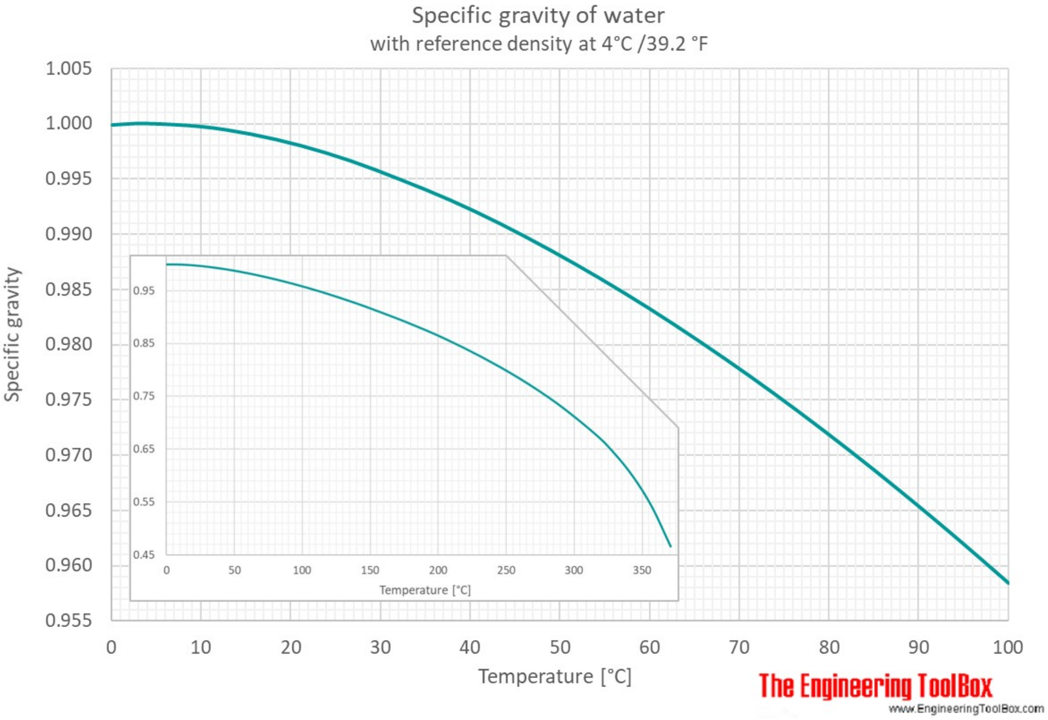

Figure 2.5: The specific gravity of fresh water as function of temperature [19]

It can be seen that the changes in specific gravity are quite small. At a temperature of 50^oC, the specific gravity of water equals $S_g = 0.988$. This means that if (2.25) is used to determine the pressure drop with a specific gravity of $S_g = 1$, assuming a water temperature of 4^oC, the error in the pressure drop caused by the specific gravity equals 1.2% if the water temperature is actually 50^oC. Since, especially for the inflow, low water temperatures are expected (outside temperature), this change in specific gravity will probably be neglected.

2.6 Leakage

Due to cavities between working parts of the pump leakages will occur. In the case of radial piston pumps, the only components between which leakage will occur are the cylinder and the piston. When the cylinder is filled with water and the piston is loaded, leading to a high pressure in the chamber, most of the water is expelled through the outlet port to the high pressure line. Because there is a small gap between the piston and the cylinder, some water will also escape through this cavity. This leakage of all pistons and chambers combined is what forms the slip flow Q_s [m^3/s]. This slip flow, together with possible compressibility, is what lowers the volumetric efficiency of the hydraulic system, since the discharge volumetric flow rate Q_d of the pump will be lower than the ideal volumetric flow rate.

This leakage flow through the clearance between piston and chamber can be assumed to be laminar ([20],[21]). It can be approximated by treating the leakage flow as a flow through a gap between two flat plates. For higher pressures this flow might become turbulent [20]. To determine whether a flow is laminar or turbulent, the Reynolds number is used. The Reynolds number can be determined as following [22]

$$Re = \frac{\rho V D_H}{\mu} = \frac{V D_H}{\nu} \tag{2.26}$$

in which Re is the Reynolds number, ρ [kg/m^3] the density, V [m/s] the flow velocity, D_H [m] the hydraulic diameter, μ [Pa s] the dynamic viscosity and ν [m^2/s] the kinematic viscosity. Flow will be laminar when the Reynolds number is below 2300 [23], but cases have been seen where flows with higher Reynolds numbers still acted laminar.

2.6.1 Flow between two parallel plates

The flow can be described as steady, two dimensional viscous flow between two perpendicular plates which are located a distance c apart [24]. This case is depicted in figure 2.6 below.

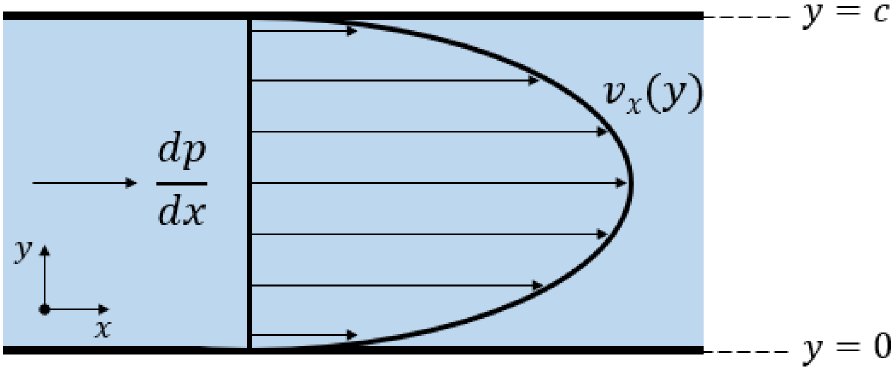

Figure 2.6: Viscous flow between two perpendicular plates

It is assumed that the pressure only varies in the direction of x. The effective pressure gradient in the x direction can be written as

$$\frac{dp}{dx} = -G \tag{2.27}$$

with G [Pa/m] as constant. This pressure gradient can be found by finding the difference in pressure between the chamber and the area above the piston, and dividing it by the length of the 'contact' area between piston and cylinder. The area above the piston is connected to a leakage line to extract the leakage flow.

Since the piston will be moving down into the cylinder, by which the high pressure is caused, the movement of the piston needs to be taken into account in the flow approximation. One of the two flat plates is assumed to move. Following the no slip boundary condition this means that the velocity of the flow at the moving plate will be equal to the velocity of the plate. The lower plate at $y = 0$ is assumed to be the piston and thus the moving plate. If this plate moves with velocity U [m/s], the following condition must apply

$$v_x(0) = U \tag{2.28}$$

with v_x [m/s] being the flow velocity in the x direction. The velocity of the flow as function of y is found in [24] as in (2.29).

$$v_x(y) = \frac{G}{2\mu} y(c-y) + U(\frac{c-y}{c}) \tag{2.29}$$

To obtain the total flow over the clearance with width c per unit width in the z-direction, (2.29) has to be integrated over the gap. The following is obtained

$$q_x = \int_0^c v_x dy = \frac{Gc^3}{12\mu} + \frac{1}{2}Uc \tag{2.30}$$

with q_x [m^2/s] the flow rate in the x direction per unit width in the z direction. For this method, the flow is assumed to be incompressible.

2.6.2 Clearance size

Using these Poiseuille Couette flow equations to find the leakage flow, the importance of the gap size between the piston and cylinder can be found. Using the dimensions of the piston-cylinder gaps of the test pump the importance of precision engineering the pistons and cylinders can seen. The test pump uses water as hydraulic medium. Because of the low viscosity of water, the gaps need to be as small as possible to minimize leakage flow as leakage flow will increase exponentially with an increasing gap size. This correlation is depicted in figure 2.7 below.

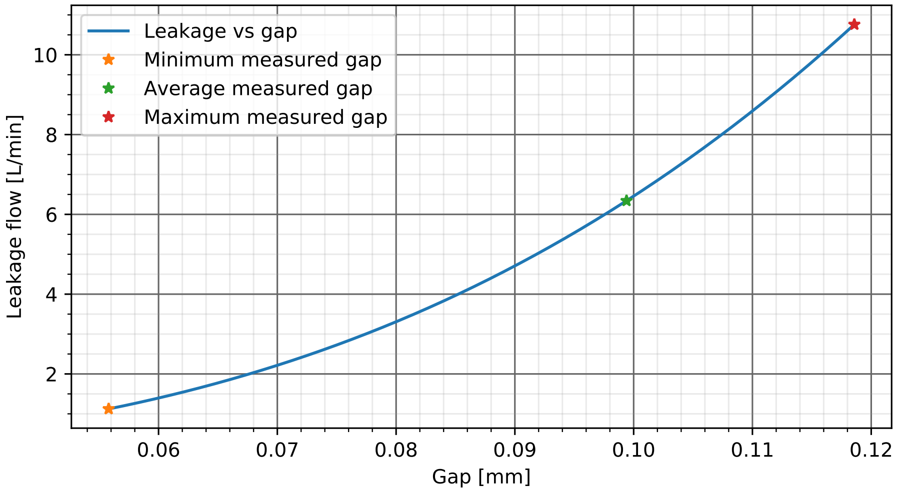

Figure 2.7: The leakage flow increasing exponentially with increasing gap size in the test pump

Not only the accuracy of the engineered parts influence the gap between the pistons and cylinders. The alignment of the piston within the cylinder is also of great importance. The ideal scenario is that the piston is aligned perfectly in the middle of the cylinder, maintaining an uniform gap size between the piston and the cylinder. If for some reason though the piston makes contact with the cylinder wall, this will cause a larger gap size on one side, reaching zero at the contact location. This can result in an larger leakage flow and unwanted friction losses through piston cylinder interaction.

The ideal scenario is depicted in figures 2.8 and 2.9 below. Figure 2.8 shows the real dimensions of the average gap between piston and cylinder for the test pump. Figure 2.9 visualizes an schematic view of the scenario.

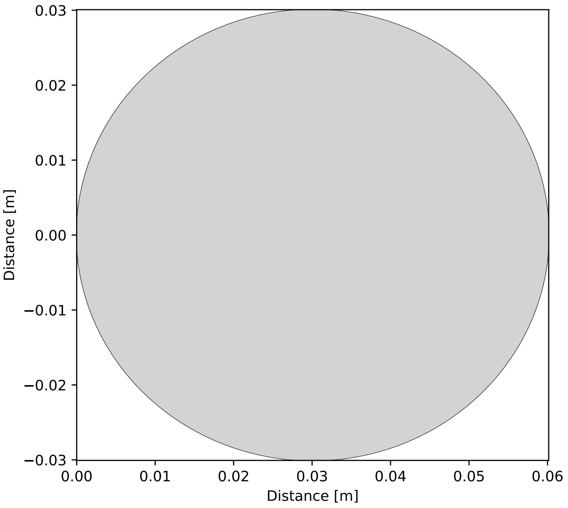

Figure 2.8: Real view of the magnitude of the gap at uniform gap size

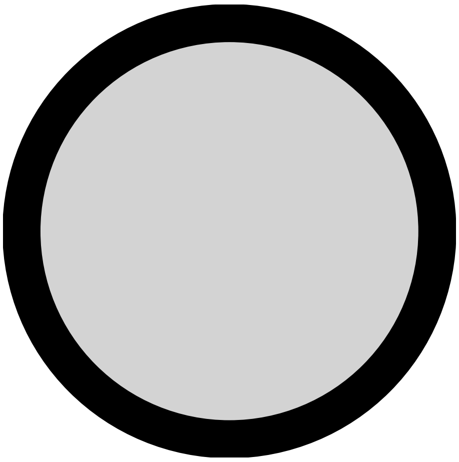

Figure 2.9: Schematic overview of the ideal uniform gap size

It is clear that the gap size is uniform during this ideal scenario and can be determined as in (2.31), with the cylinder and piston diameters d^c and d^p or radii r^c and r^p.

$$c = \frac{d^c - d^p}{2} = r^c - r^p \tag{2.31}$$

The worst case scenario for piston-cylinder interaction is depicted in figures 2.10 and 2.11 below. It is obvious that the leakage flow calculations will be harder in this case due to the non-uniform gap width as the gap size differs with circumference. The effect of this possible misalignment is discussed in chapter 4.

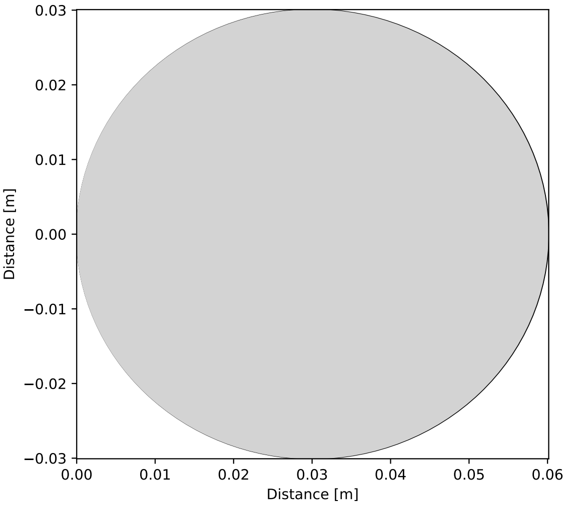

Figure 2.10: Real view of the magnitude of the gaps at misalignment

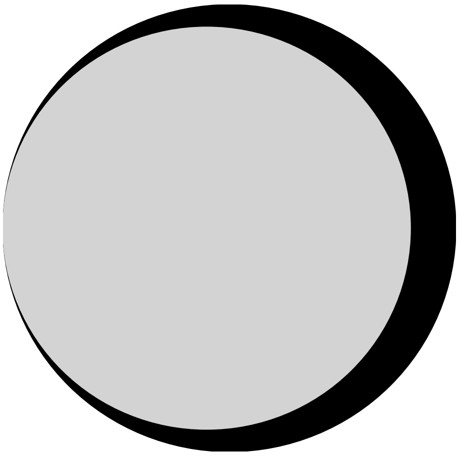

Figure 2.11: Schematic overview of how the misalignment can occur

2.7 Piston cylinder interface

The pistons are forced in an up and downward motion in the cylinders. For the test pump this is done by the rotating camring. As described the rollers move over the sinusoidal camring shape to cause the up and downward piston motion. It is discussed that the shape of this camring causes the angle of contact with the roller to change constantly and thus also the resulting normal force changes. This resultant normal force has a component which forces the piston down into the cylinder, but also a horizontal component which forces surfaces upon each other, leading to higher friction losses. This horizontal force is highly undesirable since it only causes losses. To minimize these losses in the test pump, the side forces are mitigated by a side force mitigation system containing rollers. The desired consequence is that the piston-cylinder interface will be ideal, as depicted in figure 2.9, with an uniform gap size. If this system fails, however, the scenario shown in figure 2.11 might occur, possibly leading to higher friction losses, volumetric losses and wear.

2.7.1 Uniform fluid film

For the ideal scenario the friction losses are limited to the friction resulting from the shearing of viscous fluid [25]. This scenario is depicted schematically in figure 2.9 above. The shear stress of a Newtonian fluid in a parallel flow can be deducted from the gradient of velocity in the direction perpendicular to the flow direction [26]. The shear stress is given by the following

$$\tau = \mu \frac{dv_x}{dy} \tag{2.32}$$

with τ [Pa] being the shear stress, μ [Pa s] the viscosity of the Newtonian fluid and $\frac{dv_x}{dy}$ the velocity gradient in the direction perpendicular to the flow. In figure 2.12 a parallel flow $v_x(y)$ over a flat plate is presented. This flow has a positive velocity gradient $\frac{dv_x}{dy}$ in the direction perpendicular to the flow direction of v_x. Flow increases in velocity with distance y above the plate. To find the shear stress it induces on the plate, the velocity gradient $\frac{dv_x}{dy}$ has to be found just above the plate, at $y = 0$.

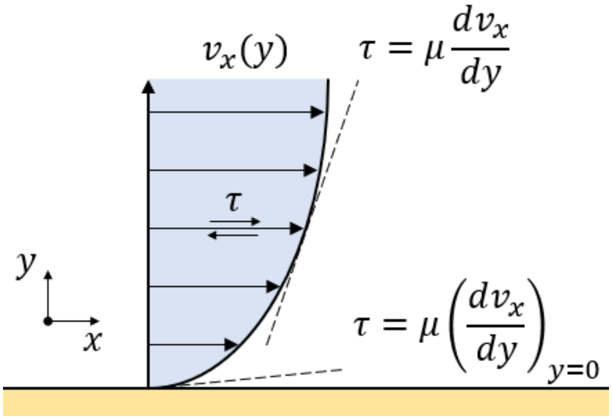

Figure 2.12: Shear stress induced by flow over a flat plate

To determine the viscous shear the hydraulic medium induces on the piston in the test pump, (2.29) is used. For this equation the piston velocity and the pressure gradient for one piston strike need to be known, together with the fluid viscosity.

Finally the values for the viscous shear τ on the piston surface is found using (2.32). Next the viscous friction force F_v this viscous shear causes is determined using (2.33) with A_w^p being the wetted piston area.

$$F_v = \tau A_w^p = A_w^p \mu \frac{dv_x}{dy} \tag{2.33}$$

The viscous shear acts as a resistance to piston movement and thus will be further taken into account when the piston forces are being discussed.

In all flow equations viscosity μ of the hydraulic fluid has been an important parameter. It can be concluded from (2.33) that the force due to viscous shear F_v changes linearly with viscosity, and thus it is important to use accurate values for the viscosity. This will be discussed further in subsection 2.9.

2.7.2 Non-uniform fluid film due to misalignment

In the misaligned scenario, which is depicted schematically in figure 2.11 above, viscous shear is not the only force resisting movement. Due to the surfaces of the piston and cylinder being forced into each other, additional friction forces occur. This is depicted schematically in figure 2.13 below. As a normal force F_n forces the two bodies together and a force F tries to put the upper body in motion, a friction force F_f equal to F resists motion.

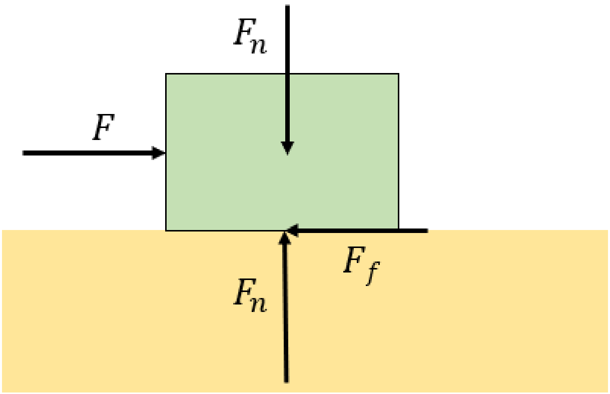

Figure 2.13: Free body diagram of friction between two bodies depicted schematically

To determine the friction force this interaction creates, the simple method of Coulomb's law of friction is used [27]. The friction force is determined by the normal force working on the body, consisting of the force which acts on it plus the gravitational force, together with a friction coefficient μ_k, as in (2.34).

$$F_f = \mu_k F_n \tag{2.34}$$

Friction coefficient μ_k specifically stands for the kinematic friction coefficient. When a body is static it requires more force to be set in motion than to keep a moving body in motion. Thus a static friction force $F = \mu_s F_n$ needs to be overcome. Since these static moments, however, are very short and thus are expected to not raise the power loss that much, they are neglected and only μ_k is used.

2.8 Seal friction

To reduce the amount of leakage rubber seals can be used around the piston and piston rod. These seals close off the small gaps between the moving components to prevent hydraulic fluid from slipping away through those clearances. By doing so these seals are in contact with moving surfaces, resisting the movement by friction.

The friction caused by a seal can be separated into two components; the seal friction due to seal compression F_C and the seal friction due to hydraulic pressure on the seal F_H ([28], [29]). These sum up the total seal friction as defined in (2.35).

$$F_{sl} = F_C + F_H \tag{2.35}$$

The friction due to compression F_C is dependent on the seal rubbing length, L_p for a piston seal and L_r for a piston rod seal, and the friction due to O-ring compression per length of rubbing surface f_c, which is dependent on the hardness of the seal and the percentage of compression designed for. The left side of figure 2.14 shows the correlation from which f_c should be taken. The friction due to compression is then obtained with (2.36).

$$F_C = f_c \cdot L_p, \quad F_C = f_c \cdot L_r \tag{2.36}$$

The friction due to hydraulic pressure on the seal F_H is dependent on the projected area of the seal, A_p for a piston seal and A_r for a piston rod seal, and the friction due to fluid pressure per magnitude of projected area f_h. Variable f_h is dependent on the pressure of the fluid it is resisting, and is found with the right side of figure 2.14. The total friction due to hydraulic pressure on the seal is found with (2.37).

$$F_H = f_h \cdot A_p, \quad F_H = f_h \cdot A_r \tag{2.37}$$

The values for L_p, L_r, A_p and A_r can be found in the Parker O-ring Handbook for different sizes of seals [28]. As the value for the total friction force found using this method is in the units pounds, it should be multiplied with 4.448 to convert it to Newton.

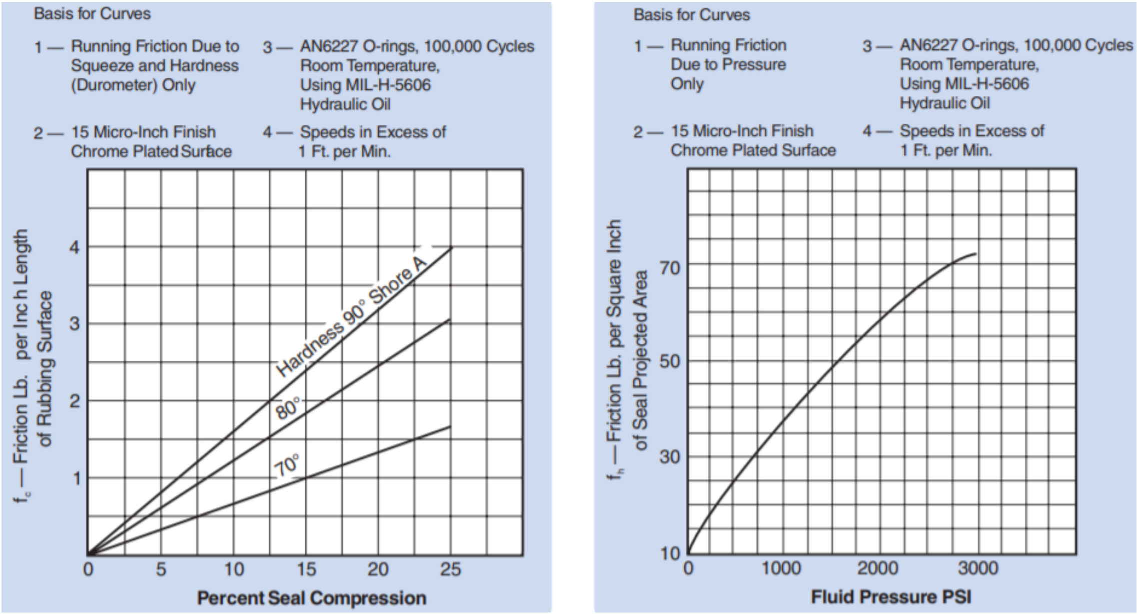

Figure 2.14: Friction f_c per length of rubbing surface correlated to seal compression (left) and friction f_h per magnitude of projected area versus fluid pressure (right) [28]

2.9 Hydraulic medium

The hydraulic medium which is used has great influence on the performance of the pump. In this work the emphasis will be on water as hydraulic medium. Water has less favorable properties to act as an hydraulic fluid than hydraulic oils. In seawater the salinity of seawater gives it a greater erosive potential, and it contains suspended solids, organic substances and dissolved gasses such as chlorine and oxygen which cause corrosion to occur [3].

Merritt [30] notes that water is a bad hydraulic fluid because of its restrictive liquid range, low viscosity and lubricity and corrosive properties. Due to new developments it has become possible to produce new water hydraulic components from anticorrosive materials which don't require lubrication. Also very small tolerances are achieved which reduce the leakages which are caused by the low viscosity of water ([31], [32]). Water also has a thermal conductivity that is 4-5 times larger than that of mineral oils, which mean that water hydraulic systems tend to need a lesser cooling capacity. Furthermore water contains much less air in solution, which leads to a lesser compressibility. Thus water has a larger bulk modulus than hydraulic oils, leading to greater rigidity which leads to faster operations and better control [33].

An important property of an hydraulic medium is the viscosity. It has already been used in several equations in this work and an accurate estimate of the viscosity is essential. Because the emphasis of this work is on water hydraulics, the viscosity of water has been researched more thoroughly.

The viscosity of a fluid is dependent of temperature and pressure. Substances will expand with raising temperatures and get compressed by raising pressures. The dependency of viscosity to temperature is depicted in figure 2.15 below. It is seen that the viscosity μ drops from 1.8 mPa s at 0 ^{o}C to around 0.55 mPa s at 50 ^{o}C. This is a significant drop over a quite small temperature range and emphasizes the importance of an accurate estimate of the viscosity.

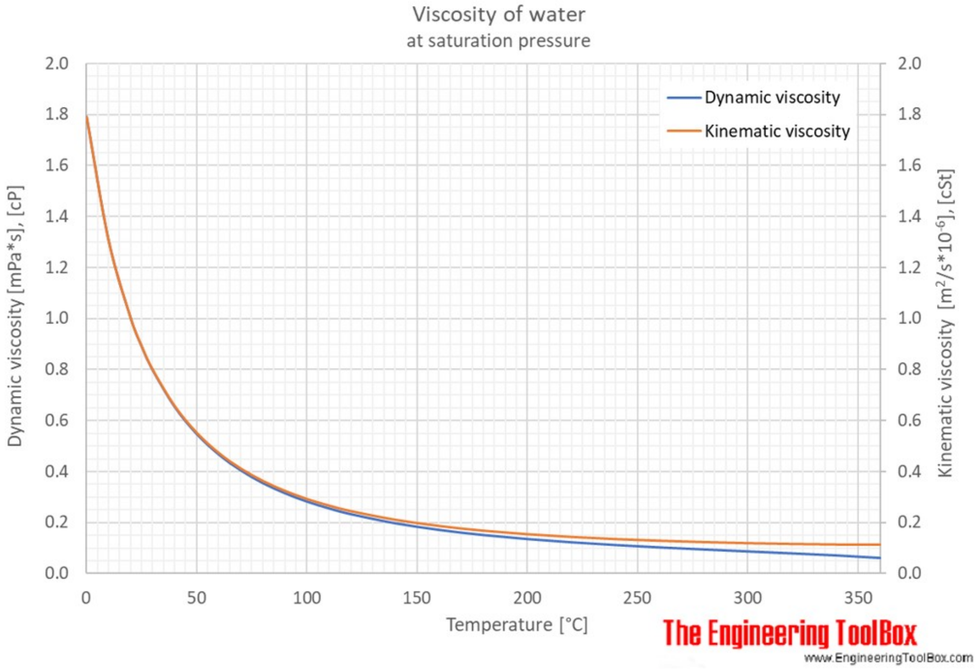

Figure 2.15: The dependency of viscosity and temperature of water [19]

Thus the viscosity of water needs to be determined as function of temperature and pressure.

For this (2.38), (2.39) and (2.40) are used [34]. Variables H_i and H_{ij} can be found in the appendix.

$$\bar{\mu} = \bar{\mu}_0(\bar{T}) \cdot \bar{\mu}_1(\bar{T}, \bar{\rho}) \tag{2.38}$$

$$\bar{\mu}_0(\bar{T}) = \frac{100\sqrt{\bar{T}}}{\sum_{i=0}^{3} \frac{H_i}{\bar{T}^i}} \tag{2.39}$$

$$\bar{\mu}_1(\bar{T}, \bar{\rho}) = \exp\left[\bar{\rho} \sum_{i=0}^{5} \left(\frac{1}{\bar{T}} - 1\right)^i \sum_{j=0}^{6} H_{ij}(\bar{\rho} - 1)^j\right] \tag{2.40}$$

Variables $\bar{\mu}$, $\bar{T}$ and $\bar{\rho}$ are the the viscosity, temperature and density of water normalized to some reference constants and are determined as in (2.41). The reference constants equal $\mu^* = 1 \cdot 10^6$, $T^* = 647.096$ [K] and $\rho^* = 322.0$ [kg/m^3] while μ [Pa s], T [K] and ρ [kg/m^3] are the variable viscosity, temperature and density.

$$\bar{\mu} = \frac{\mu}{\mu^*}, \quad \bar{T} = \frac{T}{T^*}, \quad \bar{\rho} = \frac{\rho}{\rho^*} \tag{2.41}$$

Density ρ is a necessary input in (2.40) and is found using (2.42) in which ρ_0 is the density at 0 ^{o}C and atmospheric pressure and p_0 equals atmospheric pressure [35]. The temperature is inserted in [^{o}C]. The density value found equals $\rho_0 = 999.8$ [kg/m^3].

$$\rho = \rho_0/(1 + \beta_T T)/(1 - (p - p_0)/K) \tag{2.42}$$

Two inputs necessary for the density calculation are the thermal expansion coefficient β_T [K^{-1}] and the bulk modulus K [Pa]. Data for the thermal expansion coefficient is found [36] and a fit is made to find its value for different operational conditions. The fit used is a cubic polynomial as in (2.43). The temperature is inserted in [^{o}C].

$$\beta_T(T) = p_1\left(\frac{T}{2}\right)^3 + p_2\left(\frac{T}{2}\right)^2 + p_3\left(\frac{T}{2}\right) + p_4 \tag{2.43}$$

With the data values for the polynomials are found and shown in table 2.7. The fit is depicted in figure 2.16.

p_1	p_2	p_3	p_4
1.765 E-09	-2.274 E-07	1.755 E-05	-6.688 E-05

Table 2.7: Values used for the fit in equation 2.43 for the thermal expansion coefficient β

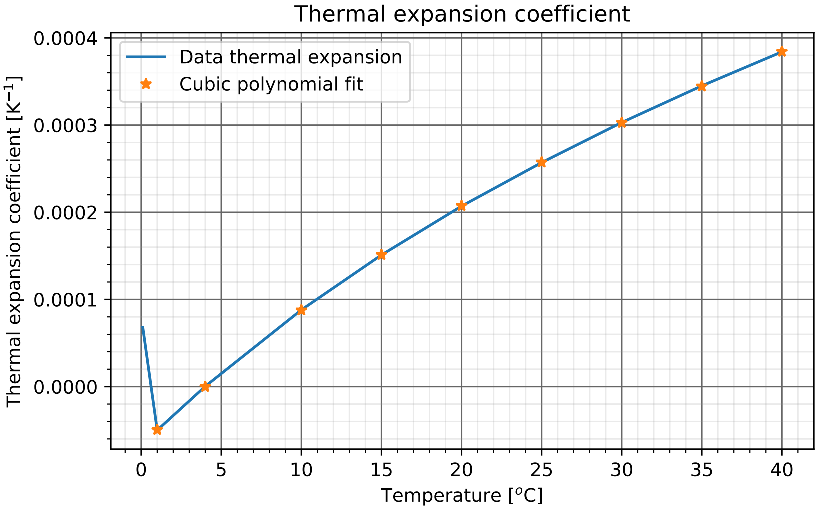

Figure 2.16: Thermal expansion coefficient fit

Another necessary input for the density is the bulk modulus K [Pa]. The Maple software contains a application to determine the bulk modulus with temperature and pressure as input [37]. This is run for temperatures between 0-40 [^{o}C] and 1-80 [bar] to obtain a dataset. With this dataset a fit is created with temperature and pressure as variables. The dataset is depicted in figure 2.17 and 2.18.

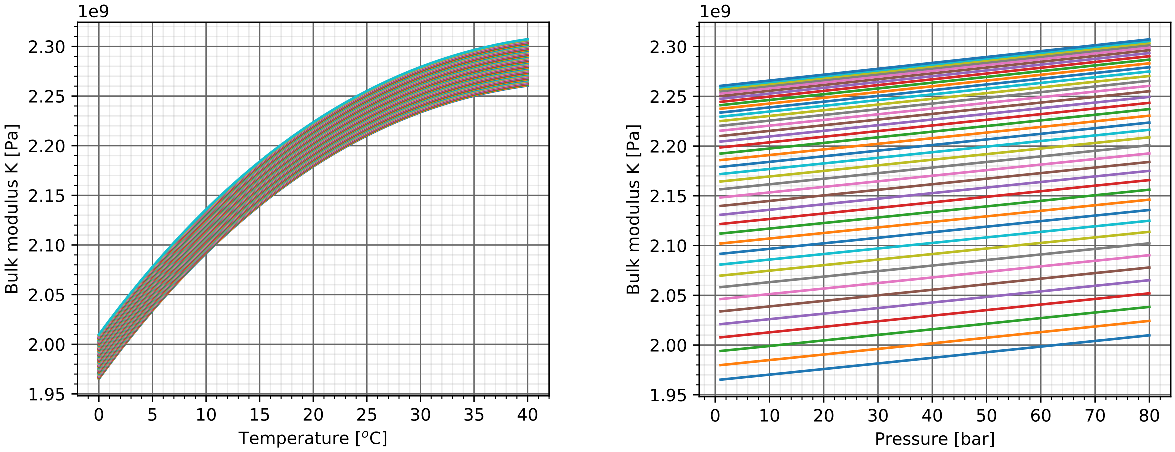

Figure 2.17: Temperature dependence bulk modulus K

Figure 2.18: Pressure dependence bulk modulus K

The variance with temperature is fitted as a cubic polynomial, the pressure dependence is fitted as a linear correlation. The temperature is inserted in [^{o}C]. Equation (2.44) is composed as function of temperature and pressure. The values for the constants are depicted in table 2.8.

$$K(T,p) = p_1 T^3 + p_2 T^2 + p_3 T + p_4 + a \cdot p \tag{2.44}$$

p_1	p_2	p_3	p_4	**a**
940.96	-221708.90	14744285.51	1965410298.91	555544.86

Table 2.8: Values used for the fit in equation 2.44 for the bulk modulus K

Chapter 3

Analytical Component-Wise Modelling of a Camring Driven Radial Piston Pump

How can the volumetric and mechanical efficiency of a radial piston pump be estimated in the design phase without experimental fitting data? A prototype camring driven radial piston pump is investigated component wise, and losses for each component are determined given an operating range. Also the potential of this model is tested by fitting certain component parameters to test data to see to what accuracy the performance can be predicted when optimal parameters are used. Furthermore an empiric modelling method found in literature is used to compare the accuracy of the model to. It is found that the model predicts leakage flow more accurately than the empiric model. The input torque is predicted to an accuracy of within 20% by the model for output pressures higher than 30 bar, but the empiric method performs better for the lower pressures.

Nomenclature

n_{cr}	Rotational speed camring [rpm]
n_w	Number of waves present in camring [-]
p_f	Fluid feed pressure [Pa]
p_d	Fluid discharge pressure [Pa]
p_l	Viscous friction torque [Nm]
μ	Fluid viscosity [Pa s]
T	Fluid temperature [K]
ρ	Fluid density [kg/m^3]
β_T	Fluid thermal expansion [K^{-1}]
K	Fluid bulk modulus [Pa]
F_n	Normal force [N]
M_l	Load friction torque [Nm]
M_v	Viscous friction torque [Nm]
M_f	end-flange friction torque [Nm]
M	Torque [Nm]
P	Power [W]
ω	Rotation angular frequency [rad/s]
C_r	rolling resistance coefficient [-]
F	Force [N]
d	Diameter [m]
v_r	Rolling velocity [m/s]
T_p	Period one piston strike [s]
y^p	Piston location [m]
U^p	Piston velocity [m/s]
l_{strike}	Piston strike length [m]
α	Camring-piston angle [^{o}]
p_c	Chamber pressure [Pa]
v_x	Flow velocity in x-direction [m/s]
c	Gap between piston and cylinder [m]
G	Pressure gradient over piston [Pa/m]
q_x	Flow per unit width in x-direction [m^2/s]
Q_s	Leakage flow [m^3/s]
Q_i	Ideal volumetric flow [m^3/s]
D_p	Ideal volumetric displacement [m^3]
A^p	Piston head area [m^2]
Q_d	Discharge flow [m^3/s]
Δp	Pressure drop [Pa]
S_g	Specific gravity [-]
Q^{cv}	Flow through check valve [m^3/s]
K_v	Valve flow coefficient [-]
A_w^p	Wetted piston area [m^2]
k_s	Spring constant [N/m]
u_0	Initial spring compression [m]
η_v	Volumetric efficiency [-]
T_d	Ideal pump output torque [Nm]
T_s	Torque loss [Nm]
η_m	Mechanical efficiency [-]
C	Fitting parameters empiric method [-]

3.1 Introduction

The basis for the current method to model the performance of piston pumps has been established in 1946 by W.E. Wilson ([38], [39]). Since then this modelling method based on fitting to experimental data has been extended by other authors ([40], [41], [42], [43]). Test data of a piston pump is acquired and certain functions containing empiric fitting parameters for volumetric and mechanical efficiency or flow and torque are fitted to the data [7]. This way an empirical model as function of pressure and rotational speed of the pump is acquired. Although this gives a good approximation of the actual performance of the pump, it becomes more difficult to correlate the losses to their actual cause. The fitting parameters say nothing about component wise losses. A model which estimates the efficiency of a pump while also showing the contribution of each component to the losses is a valuable design tool.

In this work a model is proposed which estimates the total and component wise efficiency using a semi-analytical approach. Equations to estimate the losses of each component are found which incorporate geometry, load conditions and kinematic and dynamic relative to operation input parameters. Also hydraulic and temperature effects are accounted for to a certain extend. Test data of an experimental camring driven radial piston pump are used to determine the accuracy of this modelling approach. The results are discussed and the limitations explained, and based on these limitations future work recommendations are made.

3.2 Camring driven radial piston pump

For determining the accuracy of this approach an experimental camring driven radial piston pump is used. To offer a better understanding of the proposed model first the basic principles of the workings of this pump archetype are discussed.

As the camring rotates, the rotation of the camring forces the translational piston movement, compressing the hydraulic fluid. The movement is transferred through rollers which are attached to the piston rods. Piston springs and chamber pressure forces the piston back up when the camring is not pushing it down. It is evident that the shape of the camring causes unwanted side forces, lateral to the piston axis. These have to be mitigated in a way to avoid jamming or high friction forces. To carry the camring it is supported by the pump axis through two internal bearings, one front bearing, one back bearing.

Furthermore, to avoid the hydraulic fluid from flowing back into the inflow line and from the outflow line back into the cylinder, check valves are present on both inflow and outflow lines. Fluid that leaks through the gap between piston and cylinder is removed through a leakage line.

3.3 Component-wise modelling approach

In order to obtain an analytical approximation of the efficiency of a radial piston pump, components are modelled semi-analytically. The components within the pump are described and examined individually for given input conditions. The model is designed such that inter component interaction is accounted for. The flowchart depicted in figure 3.1 presents an overview of the general model. The input parameters include the dimensions of components, the piston-cylinder configuration and bearing input parameters, among others. The model consequently sweeps through the different operating conditions for efficiency mapping of different pressure and rotational speed combinations.

3.3.1 Initial input parameters

All component calculations are performed relative to the initial input parameters. The main components in the experimental radial piston

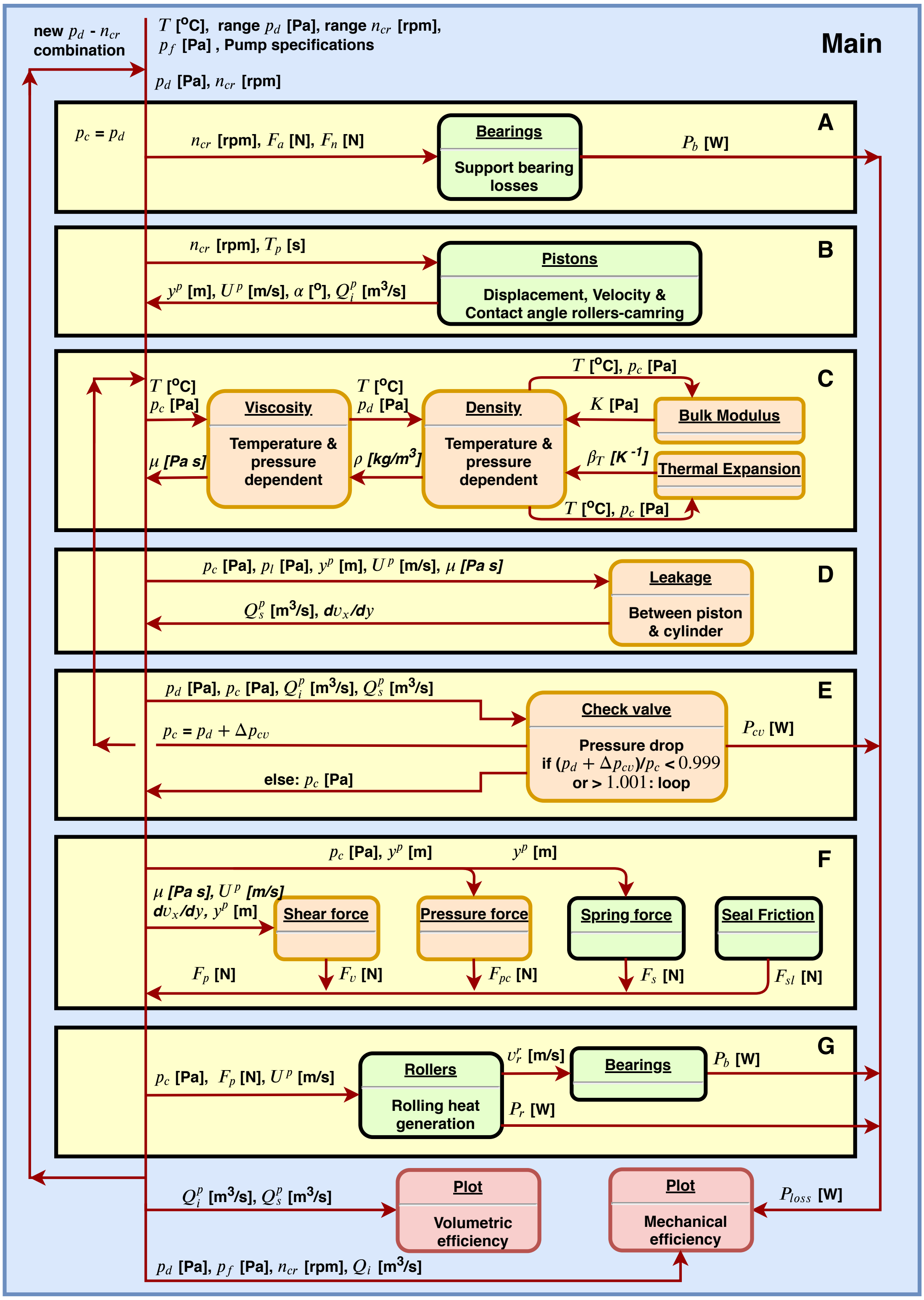

Figure 3.1: Schematic visualization of the inner working of the semi-analytical component wise model. Green boxes indicate physical components, orange boxes indicate hydraulic phenomena.

pump are the camring, rollers, bearings, pistons, check valves and the hydraulic medium.

The motion of each component in the pump is determined by the input rotation speed of the camring n_{cr} [rpm] and the number of wave shaped patterns present in the camring, which determines the number of times a piston strikes up and down per camring revolution and is denoted with n_w. The rotation speed of the camring is also referred to as the pump rotation speed.

The hydraulic medium is inserted in the system with a certain feeding pressure, p_f [Pa], leaves the system with the discharge pressure p_d [Pa] and is assumed to have a constant temperature. These are initial model input parameters.

The viscosity μ of the hydraulic medium is necessary to determine leakage flow, viscous shear and pressure drops due to flow resistance. Because the test pump uses water as hydraulic fluid its viscosity is defined more thoroughly. The determination of the viscosity is depicted in part **C** of figure 3.1. The viscosity of a fluid is dependent of temperature and pressure. The viscosity μ of water drops from 1.8 mPa s at 0 ^{o}C to around 0.55 mPa s at 50 ^{o}C [19]. This is a significant change and thus the viscosity of water is determined as function of temperature and pressure, both input parameters of the model. For this (3.1), (3.2) and (3.3) are used following the New International Formulation for the Viscosity of H_2O. Variables H_i and H_{ij} are fitted parameters and can be found in [34].

$$\bar{\mu} = \bar{\mu}_0(\bar{T}) \cdot \bar{\mu}_1(\bar{T}, \bar{\rho}) \tag{3.1}$$

$$\bar{\mu}_0(\bar{T}) = \frac{100\sqrt{\bar{T}}}{\sum_{i=0}^{3} \frac{H_i}{\bar{T}^i}} \tag{3.2}$$

$$\bar{\mu}_1(\bar{T}, \bar{\rho}) = \exp\left[\bar{\rho} \sum_{i=0}^{5} \left(\frac{1}{\bar{T}} - 1\right)^i \sum_{j=0}^{6} H_{ij}(\bar{\rho} - 1)^j\right] \tag{3.3}$$

Variables $\bar{\mu}$, $\bar{T}$ and $\bar{\rho}$ are the viscosity, temperature and density of water normalized to reference constants and are defined as in (3.4). The reference constants equal $\mu^* = 1 \cdot 10^6$ [Pa s], $T^* = 647.096$ [K] and $\rho^* = 322.0$ [kg/m^3] while μ [Pa s], T [K] and ρ [kg/m^3] are the variable viscosity, temperature and density [34].

$$\bar{\mu} = \frac{\mu}{\mu^*}, \quad \bar{T} = \frac{T}{T^*}, \quad \bar{\rho} = \frac{\rho}{\rho^*} \tag{3.4}$$

The density ρ is an input to (3.3) and is determined as

$$\rho(T, p) = \frac{\rho_0/(1 + \beta_T(T - 273.15))}{(1 - (p - p_0)/K)} \tag{3.5}$$

with the density at 0 ^{o}C $\rho_0 = 999.8$ kg/m^3 and p_0 equals atmospheric pressure [35]. For thermal expansion coefficient $\beta_T(T)$ [K^{-1}] and bulk modulus $K(T, p)$ [Pa] data sets have been used to create a fit to obtain the values efficiently ([36], [37]).

Based on these initial input parameters the power and leakage losses in all internal components are be calculated. Following the method of modelling for each component is described.

3.3.2 Losses in bearings

The power losses in the larger pump bearings which support the camring on the pump axis are determined first as just the pump rotational speed n_{cr} and an estimate of the radial loading F_n^b [N] are necessary, along with the bearing parameters. These bearing losses are calculated in section **A** in figure 3.1. The bearings which are present in the rollers present in the pump are determined with the same method and are calculated in section **G** in figure 3.1.

To determine power losses due to bearings, the method described by Harris is used [15] which is a derivation based on work of Palmgren Miner [16]. For this approximations of the load friction torque M_l [Nm], the viscous friction torque M_v [Nm] and the end-flange friction torque M_f [Nm] are defined using the bearing specific parameters, given by manufacturers.

With the torque losses known, the power loss per bearing is determined with the correlation between power, torque and rotational speed as following

$$P_b = M^b \omega^b \tag{3.6}$$

with M^b [Nm] being the sum of the torque losses and ω^b [rad/s] the rotational speed of the bearing. Torque loss in bearings can also be expressed by a rolling resistance coefficient C_r^b [-]. This means that bearing losses can be expressed identical to rolling losses, with a radial force F_n^b [N] acting upon it and a rolling resistance coefficient C_r^b indicating the fraction of F_n^b which is transferred in rolling resistance F_f^b [N]. By using the method described above to find the torque loss in the bearing, (3.7) can be used to find rolling resistance coefficient C_r^b, with d^b [m] being the bore diameter [14].

$$M^b = C_r^b F_n^b \frac{d^b}{2} \tag{3.7}$$

Consequently (3.8) can be used to determine the power loss per bearing ([8], [9])

$$P_b = F_f^b v_r^b = F_n^b C_r^b v_r^b \tag{3.8}$$

with v_r^b [m/s] as the bearing rolling velocity.

3.3.3 Piston movement

For most calculations just one piston motion is used to make the model as efficient as possible. The period of one piston motion is defined as:

$$T_p = \frac{60}{n_{cr}} \cdot n_{\mathrm{w}} \tag{3.9}$$

A vector $\mathbf{t} = [0, T_p)$ in 100 timesteps dt describes the piston movement over one piston strike.

The vertical position of the piston in the cylinder is dependent on the strike length of the piston, the rotational speed of the pump and the amount of strikes a piston makes per pump revolution. Figure 3.2 shows the different positions and motions of the piston. The position y^p [m] of the piston can be described as

$$y^p(t) = A \cdot \sin(\omega^p t + n\pi) + b \tag{3.10}$$

with the amplitude being half the strike length defined as $A = \frac{l_{\text{strike}}}{2}$ [m]. The angular frequency is found with the period, $\omega^p = \frac{2\pi}{T_p}$ [rad/s]. The phase shift equals $n\pi = -0.5\pi$ to get $y = 0$ at $t = 0$. Finally, b [m] is the initial value which equals to amplitude A. The function for piston velocity $U^p(t)$ is determined by taking the time derivative of (3.10), $\frac{dy^p}{dt}$, as seen in (3.11).

$$U^p(t) = A \cdot \omega^p \cdot \cos(\omega^p t + n\pi) \tag{3.11}$$

The angle between piston and camring α, which is depicted in figure 3.2, also alternates per piston strike and is defined as

$$\alpha = \alpha_{max} \cdot \cos(\omega^p t + n\pi) \tag{3.12}$$

with amplitude $\alpha_{\max}$ [^{o}] as maximum angle, which is an input parameter of the model.

The sinusoidal solution was found in this case to give an excellent description and provides ease of use.

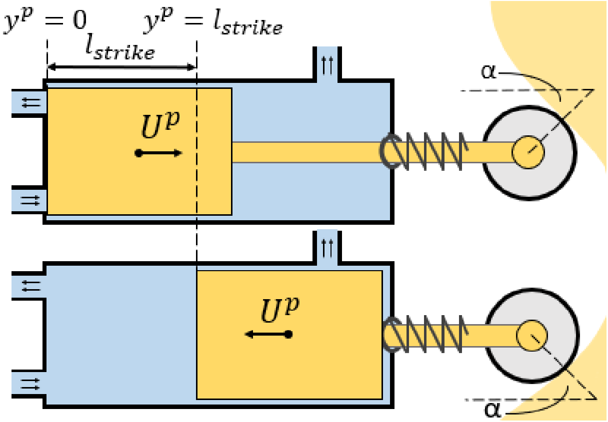

Figure 3.2: A piston depicted in its lowest and highest points in a cylinder together with its motion

3.3.4 Leakage and output flow

Next the leakage that occurs between the piston cylinder gap is determined. The leakage flow calculations are performed in section **D** of figure 3.1. The reason why leakage is the first loss defined in the model is because it is used to determine the chamber pressure p_c [Pa] required to obtain a certain discharge pressure p_d [Pa]. The chamber pressure will be higher than the output pressure of the pump due to pressure drop caused by flow resistance.

The flow is considered as laminar flow between two parallel plates ([20],[21]). For higher pressures this flow might turn turbulent [20], so a check will be performed using the Reynolds number of the flow.

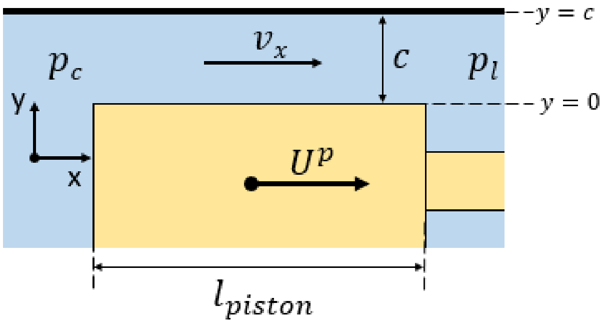

Figure 3.3: The gap between the piston and cylinder

The leakage flow between the piston cylinder gap is described as steady, two dimensional viscous flow between two perpendicular plates which are located a distance c apart driven by a moving plate and a pressure gradient G [Pa/m] [24]. The gap is depicted in figure 3.3. The piston is considered to be the moving plate. This gives the two boundary conditions $v_x(0) = U^p$ and $v_x(c) = 0$. The flow velocity v_x [m/s] at distance y from the lower plate is described as following

$$v_x(y) = \frac{G}{2\mu} y(c-y) + U^p(\frac{c-y}{c}) \tag{3.13}$$

with pressure gradient $G = \frac{\mathrm{d}p}{\mathrm{d}x}$, gap width c [m] and piston velocity U^p [m/s]. To obtain the total flow over the gap per unit width in the z-direction, (3.13) is integrated over the gap width c which gives (3.14).

$$q_x = \int_0^c v_x \, dy = \frac{Gc^3}{12\mu} + \frac{1}{2} U^p c \tag{3.14}$$

To obtain the total leakage flow per piston Q_s^p [m^3/s], this flow q_x [m^2/s] is multiplied with the average circumference of the piston and cylinder. The gap width is found as $c = \frac{d^c - d^p}{2}$ with d^c and d^p being the cylinder and piston diameters, respectively.

With the piston location y^p and velocity U^p and the fluid viscosity μ known, (3.13) can be used to predict the leakage flow. Pressure gradient G alternates with the movement of the piston, since the distance from the head of the piston to the leakage line tube alternates. The pressure gradient G is the largest when the piston is at $y^p = l_{\text{strike}}$, just as it begins expelling fluid from the cylinder, as seen in figure 3.2. Combining (3.13) with piston and cylinder dimensions leakage flow per piston Q_s^p [m^3/s] can be estimated.

With the dimensions of the piston the ideal flow per piston, without leakage Q_i^p [m^3/s] can be determined. This follows from the ideal displacement D_p^p [m^3], which is the ideal volume displaced during one piston strike, input rpm of the pump n_{cr} and number of piston strikes per pump revolution, as in (3.15).

$$Q_i^p = D_p^p \frac{n_{cr}}{60} n_w = A^p l_{\text{strike}} \frac{n_{cr}}{60} n_w \tag{3.15}$$

Now the pump discharge flow per piston Q_d^p [m^3/s] is determined as in (3.16).

$$Q_d^p = Q_i^p - Q_s^p \tag{3.16}$$

With the number of piston-cylinder configurations present in the system known the total discharge, ideal and leakage flows, Q_d, Q_i and Q_s, can be determined.

3.3.5 Pressure drop due to check valves

The output flow per piston Q_d^p is dependent on the desired output pressure p_d [Pa] since the pressure gradient G is obtained using this desired output pressure, which is a model input parameter. The pressure drop Δp due to flow resistance after the cylinder is estimated using the discharge flow per piston Q_d^p, after which this pressure drop is added to the desired output pressure p_d to obtain a new chamber pressure p_c [Pa]. This is done in section **E** in figure 3.1. This new pressure p_c is used to determine a new value for viscosity μ, as seen in section **C** in figure 3.1. Consequently a new leakage loss per piston Q_s^p is calculated together with a new discharge flow per piston Q_d^p, in section **D** in figure 3.1, which leads to a different pressure drop. This iteration between sections **C**, **D** and **E** in figure 3.1 is done until the difference in pressure drop between two iterations is negligibly small, leading to the leakage caused by the actual chamber pressure p_c. Most flow resistance is offered by check valves in the pump which ensures that fluid cannot flow back into the chamber. The following equation correlating the pressure drop with the flow rate though a valve is defined

$$\Delta p_{cv} = S_g \frac{(Q^{cv})^2}{K_v^2} \tag{3.17}$$

where S_g [-] is the specific gravity of the fluid, Q^{cv} [m^3/s] is the flow rate through one valve and K_v [-] is the valve flow coefficient which is a valve specific constant [18]. Note that because fluid is only expelled from the chamber half of the time, the flow experienced by the check valve equals $Q^{cv} = 2 \cdot Q_d^p$ m^3/s. Further pressure drop by flow resistance in the pump is neglected and thus check valve pressure drop Δp_{cv} equals total pressure drop Δp. The total power loss due to pressure drop is defined as in (3.18).

$$P_{cv} = Q_d \cdot \Delta p_{cv} \tag{3.18}$$

3.3.6 Forces resisting piston motion

The total force resisting piston motion F_p [N] is determined in section **F** of figure 3.1. The four components which are identified to contribute to F_p are discussed below.

Another use of (3.13) is to check how flow velocity v_x, as seen in figure 3.3, changes with respect to position y from the piston. This is used to determine the friction resulting from the shearing of viscous fluid on the piston [25]. The shear stress of a Newtonian fluid in a parallel flow can be deducted from the gradient of velocity in the direction perpendicular to the flow direction [26]. This results in (3.19) for friction caused by shear stress

$$F_v = \tau A_w^p = A_w^p \mu \frac{dv_x}{dy} \tag{3.19}$$

with A_w^p [m^2] as the wetted piston area.

Seals used to close off gaps on pistons and piston rods cause a frictional resistance to piston movement. The friction caused by a seal can be separated into two components; the seal friction due to seal compression F_C and the seal friction due to hydraulic pressure on the seal F_H [29]. These are dependent on compression per length of rubbing surface f_c, seal rubbing length L_{sl}, the friction due to fluid pressure per magnitude of projected area f_h and the projected area of the seal A_{sl}. Values for these variables can be found in Parker O-Ring Handbook for different sizes, materials and conditions [28]. Total seal friction is found with (3.20) with the multiplication of 4.448 necessary to convert the unit to Newton.

$$\begin{aligned} F_{sl} =& 4.448(F_C + F_H) \\ =& 4.448(f_c L_{sl} + f_h A_{sl}) \end{aligned} \tag{3.20}$$

Another force which needs to be overcome when moving the piston is caused by the piston spring with a certain spring constant k_s [N/m] and initial compression u_0 [m]. It is described as (3.21).

$$F_s = k_s(l_{\text{strike}} - y^p + u_0) \tag{3.21}$$

Together, the force caused by the chamber pressure F_{pc}, shear force F_v, seal friction force F_{sl} and the spring force F_s sum the total force required to move the piston, F_p. Chamber pressure p_c alternates between the pressure found as described above and the feed pressure p_f.

Figure 3.4 shows the forces that resist the movement of the piston within the cylinder. To move the piston inside the cylinder force F_p needs to be overcome by the camring. By doing so, unwanted side force F_{side} [N] is generated since the camring makes contact with the piston rod at angle α, as seen in figure 3.5. This side force possibly introduces extra friction or some system has to mitigate it.

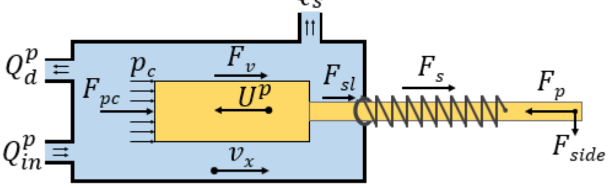

Figure 3.4: Overview of the piston-cylinder interface and the forces resisting movement

3.3.7 Losses due to rolling resistance

In this work, validation is performed using a radial piston pump which utilizes rollers on the end of the piston rod to translate the rotation of a camring to the translational motion of the piston. In the model the losses due to rolling in the rollers and bearings are determined in section **G** as seen in figure 3.1. The work done by the roller moving over the camring is described by (3.22).

$$P_r = F_f^r v_r^r = F_n^r C_r^r v_r^r \tag{3.22}$$

Roller velocity v_r^r is dependent on the piston velocity U^p and the piston-camring angle α and is derived from the outcome of (3.11) and (3.12) as in (3.23).

$$v_r^r = \frac{U^p}{\sin(\alpha)} \tag{3.23}$$

The normal force acting on the roller F_n^r is found with (3.24).

$$F_n^r = \frac{F_p}{\cos(\alpha)} \tag{3.24}$$

The roller interaction with the camring is depicted in figure 3.5.

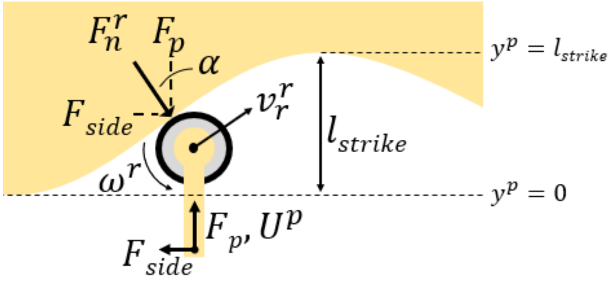

Figure 3.5: The interaction between the camring and a piston roller displayed schematically

3.3.8 Efficiency calculations

The total efficiency is divided in two main efficiencies; the volumetric and the mechanical efficiency. These are determined in the plot sections in figure 3.1. The volumetric efficiency can be determined from the ideal flow per piston Q_i^p and leakage flow per piston Q_s^p, which are determined by the methods listed above. Equation (3.25) is used to obtain the volumetric efficiency.

$$\eta_v = \frac{Q_i^p - Q_s^p}{Q_i^p} \tag{3.25}$$

The mechanical efficiency can be expressed by the ideal output torque of the pump T_d [Nm] together with the torque losses T_s [Nm] and is defined as in 3.26 [44].

$$\eta_m = \frac{T_d}{T_d + T_s} \tag{3.26}$$

Output torque T_d is found with the ideal volumetric displacement per pump revolution D_p [m^3] which is determined with the ideal flow as in (3.27).

$$D_p = Q_i \frac{60}{n_{cr}} \tag{3.27}$$

The output torque T_d is consequently found as in (3.28) with Δp_p as the pressure difference between inflow and discharge lines.

$$T_d = \frac{D_p}{2\pi} \Delta p_p \tag{3.28}$$

The torque loss T_s is found with the total calculated power loss P_{loss} [W] together with the pump angular velocity ω^{cr} and is defined as in (3.29).

$$T_s = \frac{P_{\text{loss}}}{\omega^{cr}} = \frac{60}{2\pi \cdot n_{cr}} P_{\text{loss}} \tag{3.29}$$

3.3.9 Finding parameters through data fitting

The model can be used to find parameters which are not known. One parameter important for leakage is the piston diameter. All piston diameters of the test pump have been measured and the average is used as model input parameter. The piston diameter however can alter due to thermal expansion and water absorption. To check whether the measured average piston diameter d^p makes sense, (3.14) is rewritten, while neglecting piston velocity U^p, to equal the leakage for one piston as in (3.30).

$$Q_s^p = \left(\frac{G(d^c - d^p)^3}{8 \cdot 12\mu}\right) \cdot \frac{\pi(d^c + d^p)}{2} \tag{3.30}$$

In the test data, the leakage flow is known, together with the fluid temperature and pressure. Thus (3.30) can be used to perform a least square fit to find a value for d^p which gives the smallest sum of the squared error. The same type of rewriting the model is done for the total input torque T_{in}, consisting of T_d and T_s, in a way that parameters can be fitted to the data. Rolling resistance coefficient C_r^r is fitted to the data this way to find the optimal solution.

3.3.10 Empiric modelling for comparison

An state of the art empiric modelling method is used to compare the results of the model to [7]. The empiric equation for the volumetric efficiency η_v can be taken to equal the following

$$\eta_v = 1 - C_l \frac{\Delta p_p}{\mu \omega_{cr}} - C_t \sqrt{\frac{\Delta p_p}{\mu \omega_{cr}}} \tag{3.31}$$

where C_l accounts for the compressibility of the hydraulic fluid and low Reynolds number leakage and C_t is a factor which is determined for high Reynold number leakage. The empiric mechanical efficiency equation can be taken to equal the following

$$\eta_m = 1 - C_{st} - C_c \frac{\mu \omega_{cr}}{\Delta p_p} - C_h \sqrt{\frac{\mu \omega_{cr}}{\Delta p_p}} \tag{3.32}$$

where C_{st} stands for starting torque losses, C_c accounts for the torque losses caused by Coulomb friction which are correlated to the loads in the pump and C_h is a factor which is used to approximate the hydrodynamic torque losses which are the result of fluid shear.

Equations (3.31) and (3.32) are used combined with (3.25), (3.26) and (3.28) to find the leakage flow and input torque with this empiric method.

3.4 Validation of the model results

To assess the accuracy of the model test data is necessary of a pump of which detailed specifications are known. With all of the dimensions and components known the pump specifications can be inserted into the model to get an estimation of the efficiencies of that specific pump. The pump of which test data is acquired is a radial piston pump driven by a rotating camring. This pump is designed for operations up to 80 bar and 30 rpm.

The test data contains data points at which, at a certain output pressure and rotational speed, measurements have been performed, including discharge flow Q_d, water temperature T, feed pressure p_f and input torque T_{in}. A total of 57 data points for different operational conditions are available. Internal leakage is assumed to be negligibly small, and thus leakage flow equals $Q_s = Qi - Q_d$.

The leakage flow and input torque are determined by using the model, by using the fitted model and by using the empiric fitting model. Each method is compared to the actual values obtained from the test data. In all figures a negative value for a datapoint means that the test data at that point is larger than what the method depicted in that figure predicted.

3.4.1 Comparison of the leakage flow

As the volumetric efficiency of this type of pump is built up only out of the ideal output flow Q_i and the leakage flow Q_s, comparing the leakage flows of all three methods to the test datapoints is the most direct comparison possible.

The difference in percentage between the leakage flow predicted by the model, with the measured value for the piston diameter d^p, and as determined with the test data, is depicted in figure 3.6. The mean difference between all datapoints is 2.65%.

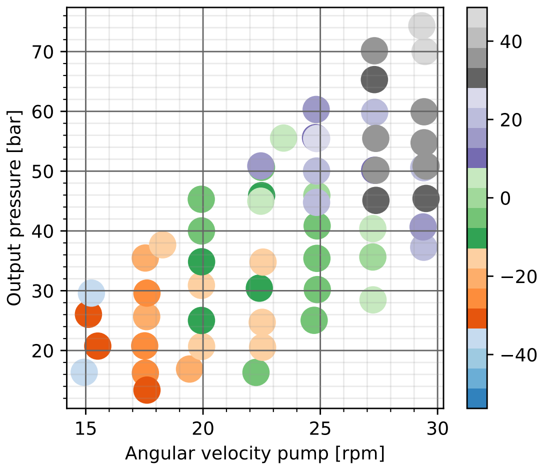

Figure 3.6: The leakage flow measured at the datapoints compared to the leakage flow predicted by the model, difference in percentages

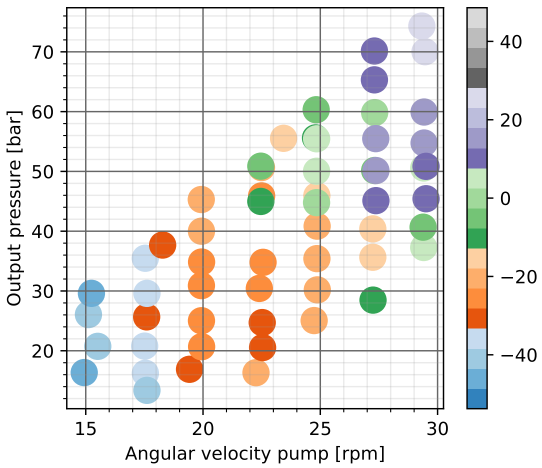

Figure 3.7: The leakage flow measured at the datapoints compared to the leakage flow predicted by the model with a fitted value for the piston diameter, difference in percentages

In figure 3.7 the leakage flow estimated by using the model with the fit for the piston diameter is compared to the test data. By fitting the leakage data to the model a new value for d^p is found. The measured value is $d^p = 60.0517$ mm. The fitted value equals $d^p = 60.05725$ mm. The mean difference found using this method is -13.60%. The reason why this fitted method differs more is because the least square fit is used, which finds the smallest value for the sum of the squared error, which in this case does not give the smallest average percentage difference.

Figure 3.8 shows the comparison between the leakage flow obtained using the empiric fitting modelling method and the test data. The average difference of the comparison is -47.75%.

On average, the method using the model with the measured value for the piston diameter gives the best result. It however has big outliers in both the left bottom corner of the operational envelope and the top right corner. The variant using the fitted value for d^p shows about the same pattern. Underestimations are made in the bottom left corner, overestimations are made in the top right. The empiric fitting method, depicted in figure 3.8, shows large underestimations of the true leakage flow over the entire operational envelope.

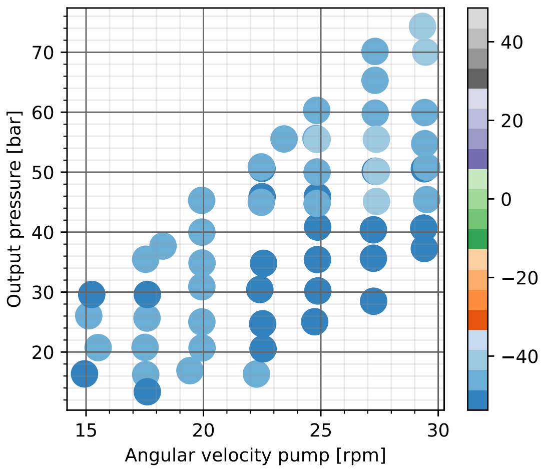

Figure 3.8: The leakage flow measured at the datapoints compared to the leakage flow predicted by the empiric fitting model, difference in percentages

3.4.2 Comparison of the input torque

The mechanical efficiency is determined with the input torque and the output torque. The output torque is an input into the models and thus is set the same as what is measured at each datapoint. Thus to compare the models to the test data, the input torques are compared, as this contains the output torque and the torque losses in the system.

Figure 3.9 shows the comparison between the input torques as calculated with the model and the torques from the test data. The average difference between the model and the data is -18.56%.

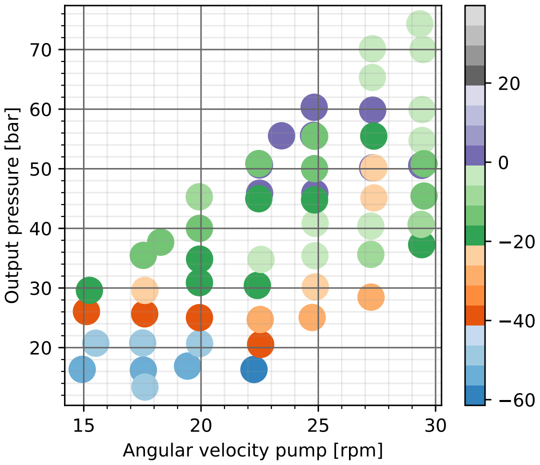

Figure 3.9: Total input torque measured at the datapoints compared to the torque predicted by the model, difference in percentages

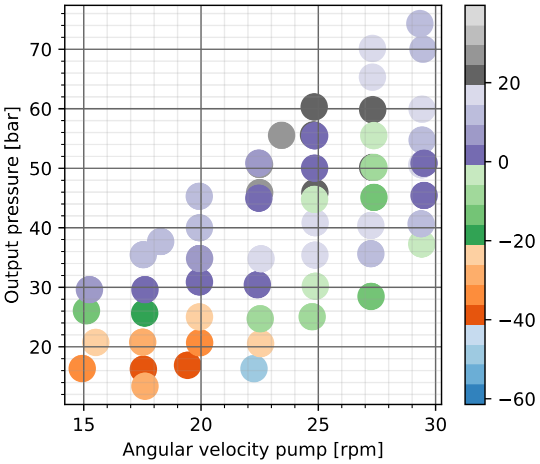

Figure 3.10: Total input torque measured at the datapoints compared to the torque predicted by the model with a fitted value for the rolling resistance coefficient C_r^r, difference in percentages

The results of the comparison performed with the values obtained from the model, using a rolling resistance coefficient obtained by fitting, are depicted in figure 3.10. In the model a rolling resistance coefficient of $C_r^r = 0.001$ is used, whereas the fit gives $C_r^r = 0.0302259$. This new value for the rolling resistance coefficient gives an mean difference between predictions and data of 1.00%.

In figure 3.11 the comparison is made between the test data torques and the torques obtained using the empiric fitting model. The average difference over all datapoints is 0.12%.

On average, the empiric fitting model gives the best result. The comparison in figure 3.11 shows some undershoot in the bottom left corner and overshoot mainly in the right side of the figure, but the overshoot observed in figure 3.9 is much larger. It is seen though that, above an output pressure of 30 bar, the estimated torque in this figure is within a 20% absolute difference. It is mainly the lower pressures for which the predictions are poor. The fitted model depicted in figure 3.10 lowers to underestimations made at lower pressures, but in turn decreases the accuracy of predictions are higher pressures.

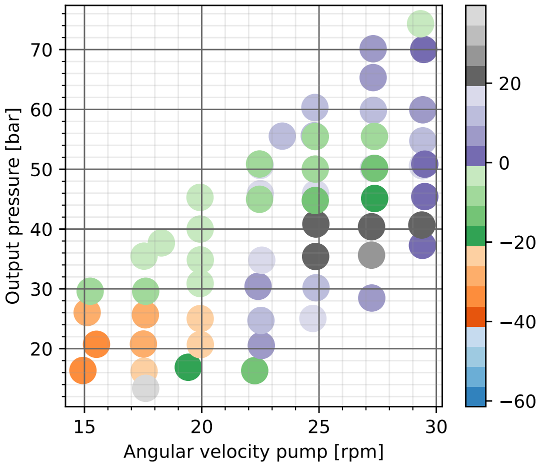

Figure 3.11: Total input torque measured at the datapoints compared to the torque predicted by the empiric fitting model, difference in percentages

3.5 Discussion of the results and further recommendations

Without fitting the volumetric efficiency is estimated with an average difference of 2.65%.

It is seen in figure 3.6 that the model results show a bigger error for higher pressures. A possible explanation for this can be the assumption of laminar flow that is made in the model. It is checked whether the flow remains laminar, which is necessary for the Couette Poiseuille flow equation, (3.13), to be valid. For the measured piston diameter, $Re = 2300$ is crossed above an output pressure of 67 bar. The validity of the model above this pressure is uncertain. It is seen though that with more accurate engineering, which results in a smaller average gap width, Reynolds numbers drop significantly. Thus more precise engineering will make the model valid for larger operating ranges.

For the validation of the model one pump has been used which has a limited operational range. To test the validity of the model further it should be ran for different pumps with different operating ranges so that the generality of the model can be assessed. When the model is ran for a larger operating range of the test pump figure 3.12 is obtained. Although the pump is not designed to withstand these loads and thus the rollers will fail plastically, the figure depicts the capabilities of the model and the need for further validation.

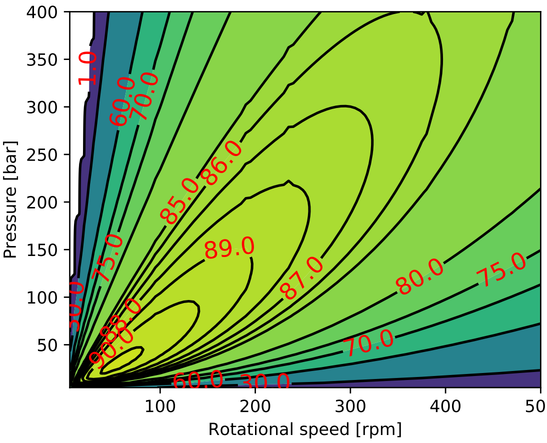

Figure 3.12: Total efficiency determined by the model for a much larger operational range

When increasing the rotational speed of a pump it is expected that the mechanical efficiency drops, while the volumetric efficiency increases [7]. To check whether the model behaves as expected in a larger operational range with higher rotational velocities, the volumetric, mechanical and total efficiency of the test pump are determined at 50 bar for a large rotational speed range. The results are depicted in figure 3.13. It is seen that the expected pattern is obtained, but the accuracy should be validated with different test pumps with higher rotational speeds.

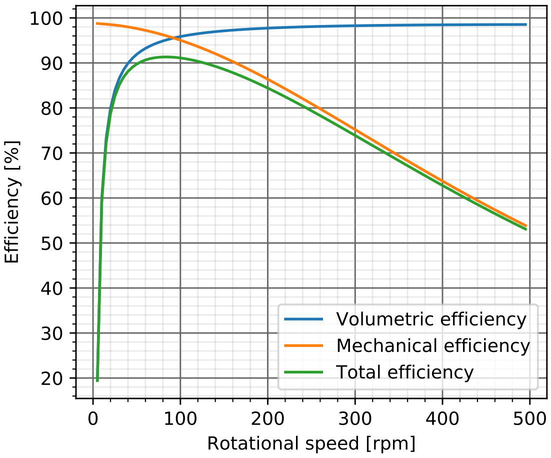

Figure 3.13: The efficiencies determined by the model versus rotational speed at 50 bar output pressure

The losses in the rollers of the test pump due to rolling resistance are based on the assumption that the rollers have the same rolling resistance coefficient as steel train wheels on rails, $C_r^r = 0.001$ [10]. The accuracy of this is unknown. For a more precise model, when working with a pump which contains rollers, more work should be done to obtain a more accurate rolling resistance coefficient, for example by FEM analysis or by building a test bench.

Components which could not be analyzed without an empirical parameter are the valves. Pressure drops are calculated with a valve specific flow coefficient K_v, which is derived empirically. For off the shelf valves this coefficient is supplied by the manufacturer. When a valve is designed in house, a test set-up is necessary to determine this coefficient, as was the case for the test pump.

Furthermore the losses in bearings are based on a constant viscosity of the lubricating grease. This viscosity, however, alters with temperature. In further work an estimation of the temperature in bearings according to operation conditions can be made, which can lead to a more accurate estimation of the grease viscosity. Also the amount of lubrication present could be investigated.

Furthermore the material of which the piston and cylinder are made can be of great influence on the performance of the pump. If the material has a relatively large thermal expansion coefficient, gaps between piston and cylinder could grow and shrink with changing temperature conditions. Also, the water absorption of a material should be taken into account since this may also change the designed gap width. These material properties are not taken into account but are highly recommended to apply in future work.

Based on the method described in this work recommendations can be made on pump design. Figure 3.14 shows the normalized power losses per component of the test pump. Based on this graph it can be concluded that the roller-bearing system would offer the greatest possibilities for mechanical efficiency improvements.

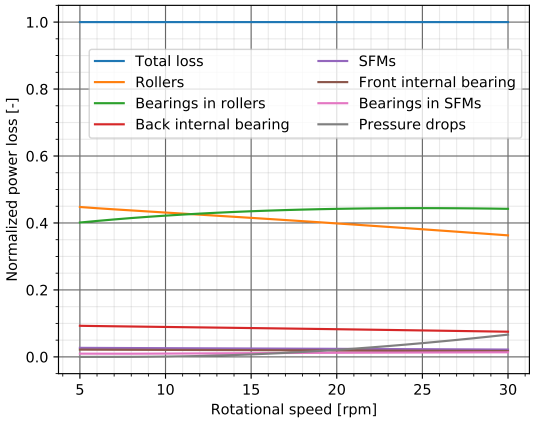

Figure 3.14: The estimated power losses of all components present in the test pump normalized to the total power loss

Chapter 4

Sensitivity of Model to Parameters

It is important to assess which components contribute the most to the losses within the pump system. Since they generate the largest losses they are the most interesting parts to study further. With more accurate modelling and consideration of assumptions new design choices could be considered to minimize these losses. The sensitivity study done in this chapter is based on the model for the test pump.

To this end figure 4.1 depicts all of the losses within one piston configuration together with the total loss of 1 piston configuration. This is done for the operational rotational speed range of the test pump at 80 bar output pressure. Figure 4.2 visualizes all of the losses within the pump, at the same operating conditions. The abbreviation SFM stands for side force mitigation system.

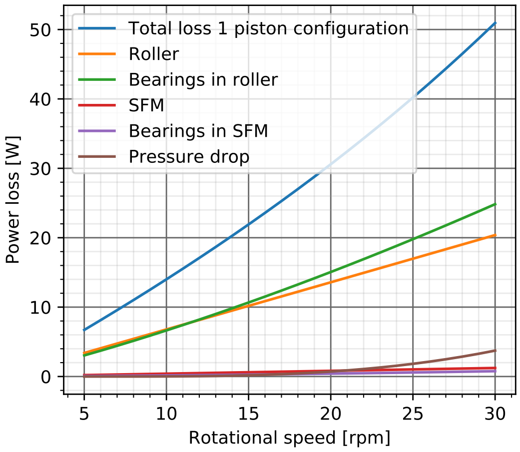

Figure 4.1: All of the power losses in 1 piston configuration according to the model plotted together versus rotational speed at 80 bar

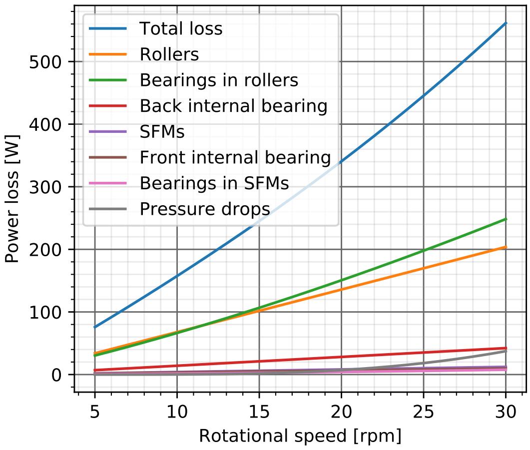

Figure 4.2: All of the power losses in the pump according to the model plotted together versus rotational speed at 80 bar

To indicate which percentage of the total losses each component contributes, the same graphs are made, normalized to the total loss. Figure 4.3 shows the losses within one piston configuration normalized to the total losses of one piston configuration. Figure 4.4 shows the total losses of each type of component within the entire pump, normalized to the total loss of the pump.

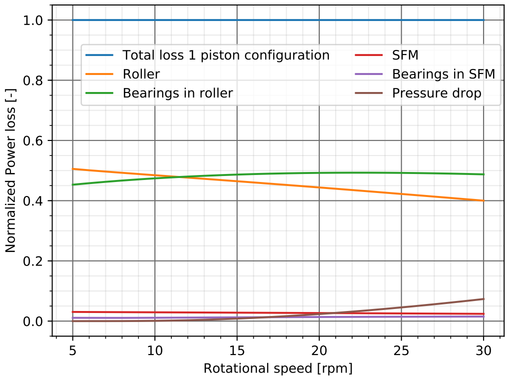

Figure 4.3: All of the normalized losses in 1 piston configuration according to the model plotted together versus rotational speed at 80 bar

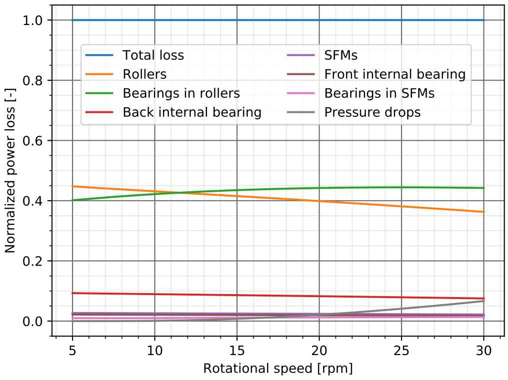

Figure 4.4: All of the normalized losses in the pump according to the model plotted together versus rotational speed at 80 bar

It is clear that the rollers and the integrated bearings cause most of the losses according to the model. This emphasizes the importance of good estimation of losses in these parts. To this end the assumptions made for calculations are discussed and their sensitivity to change assessed.

4.1 Sensitivity of rolling losses estimation to rolling resistance coefficient

The method used for predicting the losses due to rolling resistance, (3.22), shows that the losses are correlated linearly to the rolling resistance coefficient C_r^r. This means that a rollings resistance coefficient twice as large causes twice as much losses in the model, as is seen in figure 4.5.

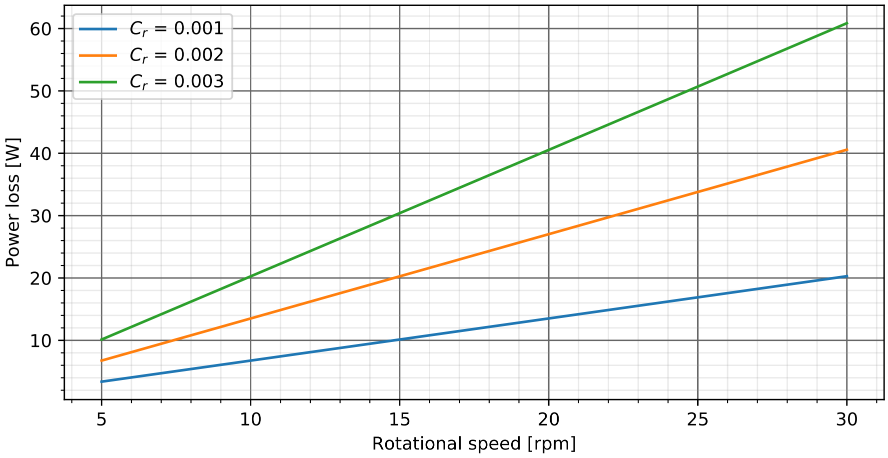

Figure 4.5: The power losses due to rolling resistance for one roller at 80 bar for different rolling resistance coefficients

In figure 4.6 it is visualized how the contribution of rolling resistance to the total losses per piston configuration changes with an increasing value of C_r^r. With $C_r^r = 0.001$, the approximate coefficient valid for steel wheels on rails, the contribution of the rolling resistance ranges from 50% at 5 rpm to 40% at 30 rpm. When $C_r^r = 0.003$ is taken, the contribution already ranges from 75% to 67%.

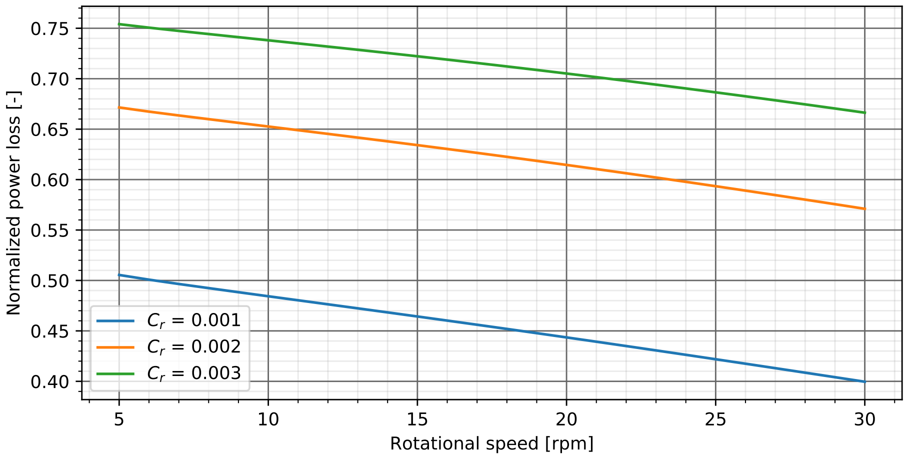

Figure 4.6: The power losses due to rolling resistance for one roller at 80 bar for different rolling resistance coefficients normalized to the total loss per piston configuration

Since a value of $C_r^r = 0.001$ is about as low as it gets and the percentage of contribution at this value is already up to 50% it is clear that the rollers are one of the more important components within this type of pump and should be investigated further to enable a more accurate model to be created.

4.2 Sensitivity of the bearing rolling resistance coefficient to operating conditions

To calculate the power losses in bearings the empiric method described in chapter 2 is used to estimate the torque loss in the bearings. With the torque loss known, corresponding rolling resistance coefficient C_r^b is determined with (2.14). This rolling resistance coefficient, however, is dependent on the operating conditions. To see how it changes with the operating conditions, one of the bearings present in the camring roller is investigated. Figure 4.7 depicts the rolling resistance of a bearing present in the camring roller during the entire operating range. An lubricant viscosity of $\nu_0 = 50$ [cSt] is used.

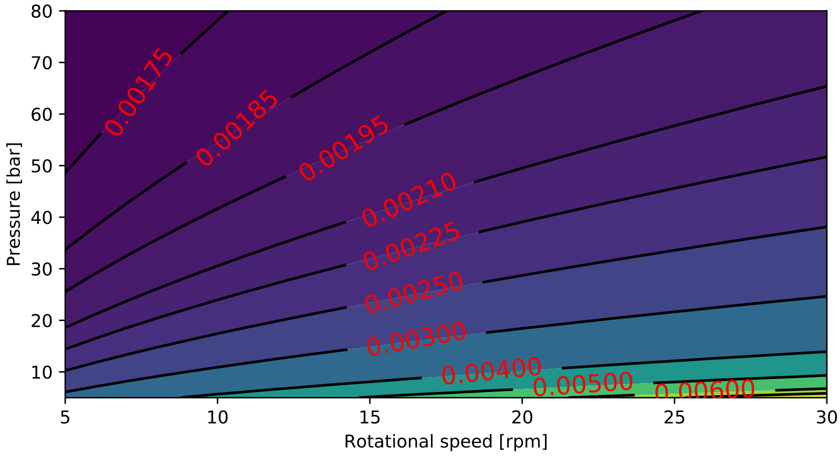

Figure 4.7: The rolling resistance coefficient of a bearing present in the camring roller for the entire operating range of the test pump

It is seen that the rolling resistance increases with increasing rotational velocity, but decreases with increasing pressure. When inspecting (2.16) and (2.20) it is seen that the load friction torque M_1 is effected by alternating load, while the viscous friction torque M_v is effected by rotational velocity and bearing lubricant. With (2.14) it is easily seen that for a higher rotational velocity which leads to a higher value for M_v, but not a higher value of normal force F_n^b, the rolling resistance coefficient C_r^b is increased.

As a higher pressure leads to a lower value for C_r^b, it can be concluded that load friction torque M_1 increases slower than radial force F_n^b with increasing pressure.

Figure 4.8 shows how, with a constant pressure, C_r^b alters with increasing rotational speed of the pump. This is done for pressures from 5 bar to 80 bar, with 80 bar giving the lowest values for the rolling resistance coefficient. Figure 4.9 visualize how C_r^b alters with constant rotational speed of the pump but increasing pressure. This is done for rotational speeds from 5 rpm to 30 rpm, with 30 rpm giving the highest values for the rolling resistance coefficient.

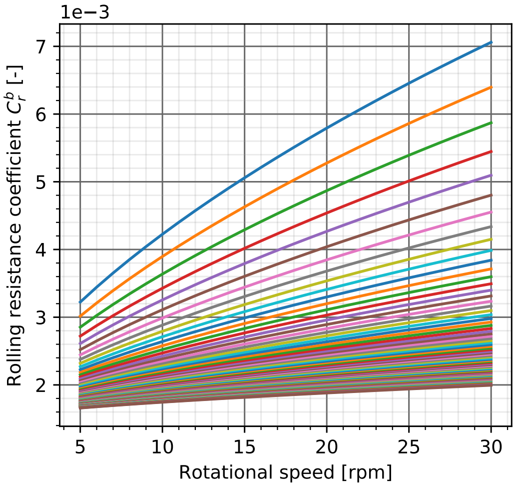

Figure 4.8: How the rolling resistance of a roller bearing present in the camring roller alters with rotational speed

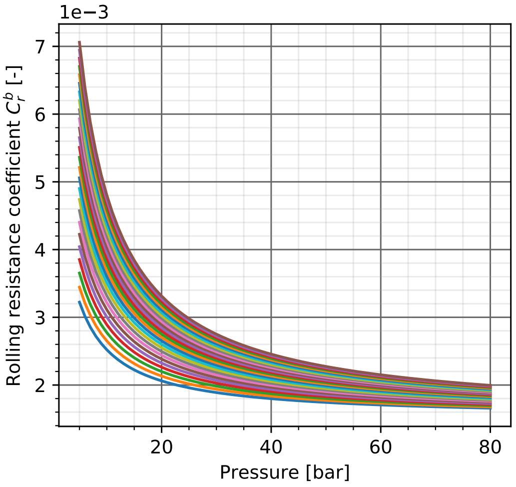

Figure 4.9: How the rolling resistance of a roller bearing present in the camring roller alters with pressure

The calculations in this section have been made with a constant lubricant viscosity of 50 [cSt]. During operation, however, the viscosity of the lubricant may alter. If the lubricant heats up during operation the viscosity will drop. How the model responds to a change in lubricant viscosity is therefore discussed in the next section.

4.3 Sensitivity of bearing losses due to bearing lubricant viscosity

The bearings together with rollers are the biggest contributors to losses in this type of pump according to the model, as can be seen in figures 4.3 and 4.4. Therefore it is assessed which assumptions are made in calculating the bearing losses and how these influence the outcome.

In the method utilized a lot of empirical parameters are used which are determined and delivered by the bearing manufacturer. This makes this method easy to use as only the variables have to be determined which are dependent on the system in which they are present.

Variables like radial force F_n^b [N] and rotational velocity are fairly easily obtained by modelling the moving components of the pump. One variable which is found to be harder to obtain is the viscosity of the bearing lubricant ν_0 [cSt].

Viscosity changes with changing operating conditions, especially due to temperature changes [45]. As a bearing is working for some time in a certain operating range a certain lubricant viscosity is reached. How the viscosity of the lubricant influences the losses caused by the bearings inside the rollers in the test pump is depicted in figure 4.10.

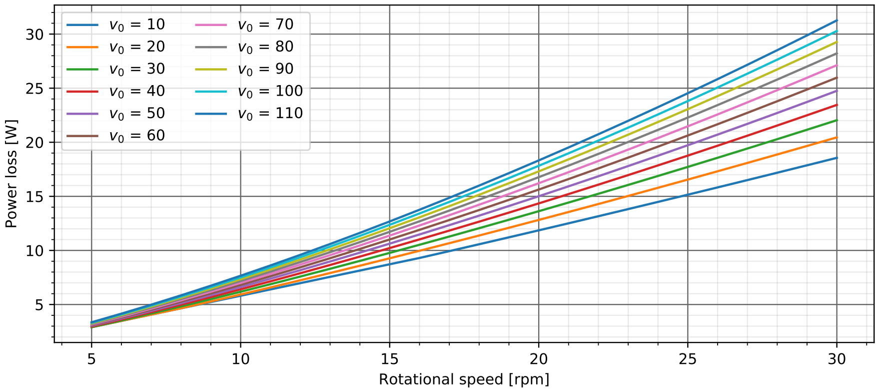

Figure 4.10: The power loss of the two bearings present inside the roller at 80 bar for different lubricant viscosity's

It can be seen that at 30 rpm the lowest viscosity of $\nu_0 = 10$ cSt causes a loss of around 31 W, while the highest viscosity of $\nu_0 = 110$ cSt causes a loss of only 18.5 W. As these are the losses per piston configuration this difference will have a large impact when looking at the efficiency of the entire pump. Figure 4.11 shows what percentage of the total losses per piston configuration the bearings cause for the different viscosity's. With the lowest viscosity $\nu_0 = 10$ cSt the bearings account for 54.5 % of the total losses per piston configuration. At the highest viscosity, $\nu_0 = 110$ cSt, the bearings cause 41.5% of the losses. This difference of 13% is significant and therefore emphasizes the importance of an accurate bearing lubricant viscosity ν_0.

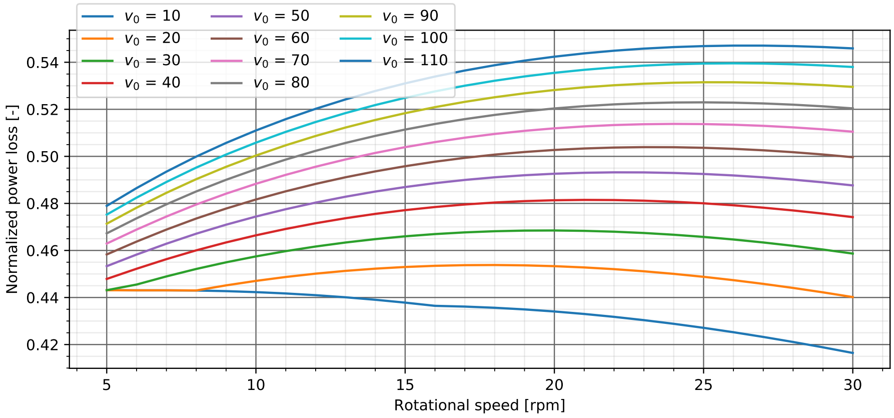

Figure 4.11: The power loss of the two bearings present inside the roller at 80 bar for different lubricant viscosity's normalized to the total loss per piston configuration

Another aspect which shows the effect of viscosity in the empiric method used to determine the torque losses is the rolling resistance coefficient of the bearing, C_r^b. Figure 4.12 shows the rolling resistance coefficient of a bearing present in a camring roller during all operating conditions, for a lubricant viscosity of $\nu_0 = 10$ [cSt]. Figure 4.13 shows this for a lubricant viscosity of $\nu_0 = 110$ [cSt]. It is seen that especially at lower pressures and higher rotational speeds of the test pump the difference in rolling resistance coefficient is significant.

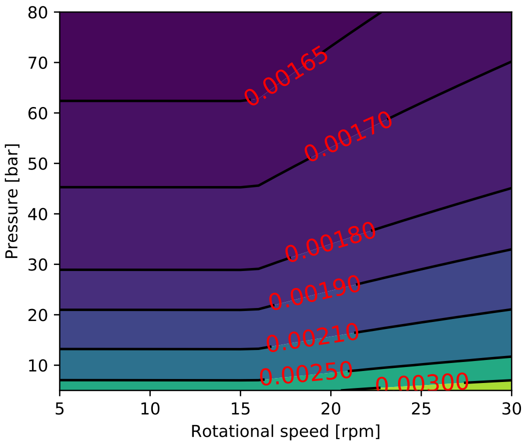

Figure 4.12: The rolling resistance of a bearing present in the camring roller for the entire operating range of the test pump with $\nu_0 = 10$ [cSt]

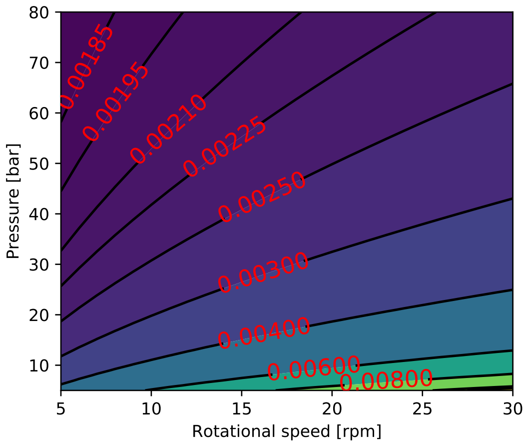

Figure 4.13: The rolling resistance of a bearing present in the camring roller for the entire operating range of the test pump with $\nu_0 = 110$ [cSt]

4.4 Temperature of the hydraulic fluid

As the viscosity of a fluid is highly dependent on the temperature it is investigated what impact a change in temperature has on the results obtained from the model. This way it can be estimated how important an accurate estimate of the operating temperature is.

4.4.1 Effect of temperature on leakage

How leakage varies with increasing temperature is investigated with the model for the test pump using the average measured gap size. As the viscosity of water decreases with increasing temperature according to (2.38), it can be seen from (3.13) that leakage flow increases with decreasing viscosity. This dependence is depicted in figure 4.14 below for different temperatures.

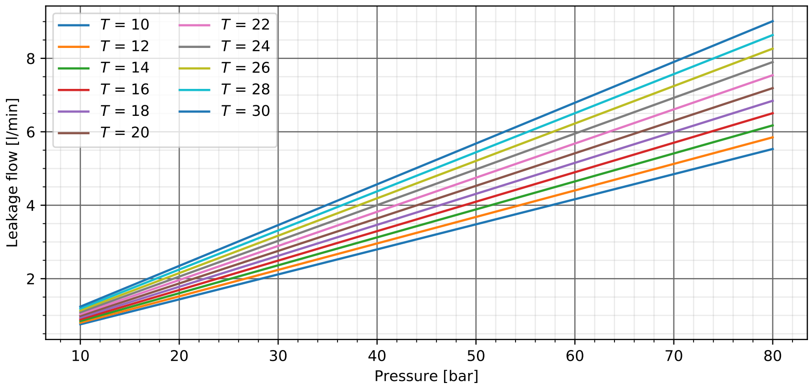

Figure 4.14: The leakage flow versus pressure for each piston for different fluid temperatures according to the model at 30 rpm

It is seen that at a temperature of 10 ^oC the leakage flow per piston configuration at 80 bar equals 5.5 L/min, while at a temperature of 30 ^oC the leakage flow increased to 9 L/min. To show what effect temperature has on the efficiency of the pump the volumetric efficiency of the pump for the different temperatures has been visualized in figure 4.15 below. Do note that possible expansion of the piston due to temperature increase has not been taken into account in the results.

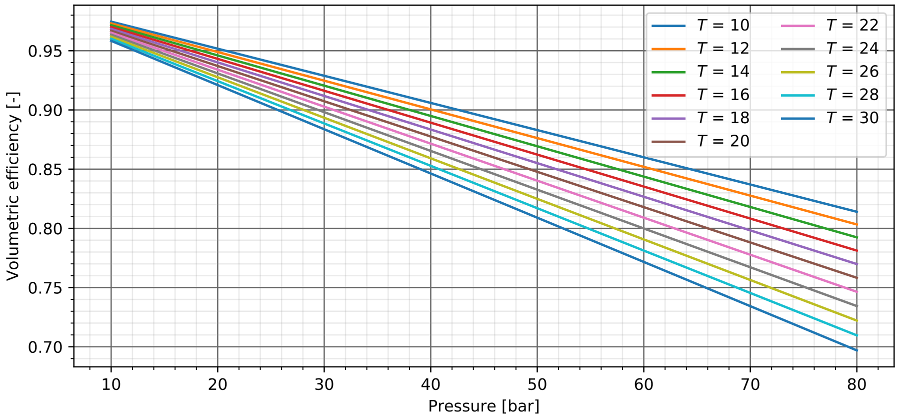

Figure 4.15: The volumetric efficiency versus pressure for different fluid temperatures according to the model at 30 rpm

The volumetric efficiency at a water temperature of 10 ^oC is found to be around 81.5%, while the efficiency at a water temperature of 30 ^oC is reduced to around 69.5%.

The already low viscosity of water is very variable with temperature, as is shown in figure 2.15 in section 2.9 Hydraulic medium. To cope with these low viscosity's it is important that pumps using water as hydraulic fluid are designed to have very small gaps between the piston and cylinder to minimize leakage. Important factors to consider here are how accurate the piston and cylinder of certain materials can be manufactured and possible expansion of the piston with increasing temperature. If the expansion of the piston at higher temperatures is not accounted for jamming might occur.

4.4.2 Effect of temperature on viscous shear

From (3.19) it can be concluded that the viscous friction force F_v is dependent on viscosity μ of the fluid film and therefore dependent on the temperature of the fluid. Furthermore it is dependent on the change of flow velocity with distance y just above the piston surface, $\frac{dv_x}{dy}$. As the leakage flow increases with increasing temperature, as discussed above, $\frac{dv_x}{dy}$ is also expected to change with increasing temperature.

To investigate the dependence of viscous shear force F_v on temperature first the dependencies of $\frac{dv_x}{dy}$ and μ on temperature are visualized for the operational pressure range of the test pump at 30 rpm. Figure 4.16 shows the dependency of $\frac{dv_x}{dy}$, figure 4.17 that of μ. It is seen that $\frac{dv_x}{dy}$ indeed becomes larger with increasing temperature, in contrary to the viscosity, which decreases with rising temperature.

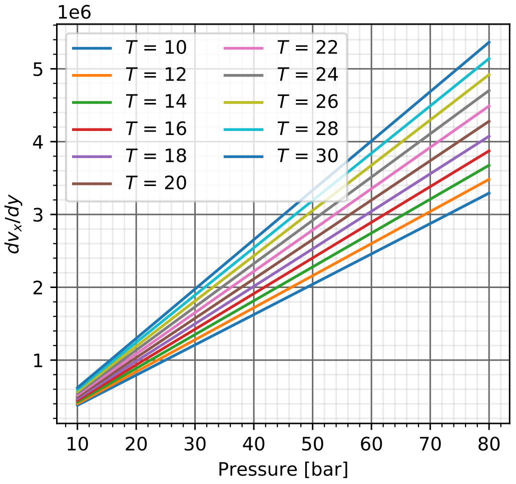

Figure 4.16: Change of flow velocity in leakage fluid film just above the piston surface $\frac{dv_x}{dy}$ for different fluid temperatures versus pressure

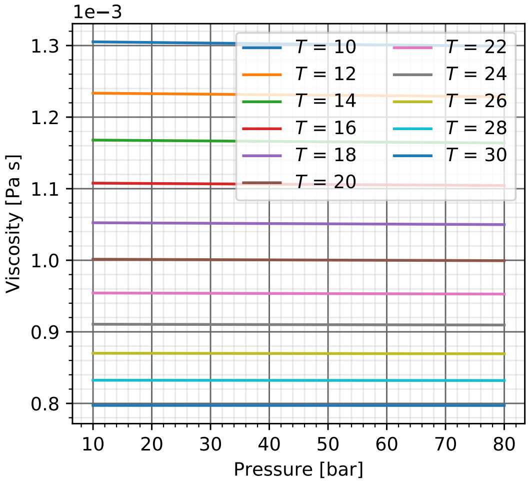

Figure 4.17: Viscosity μ of the leakage fluid film for different fluid temperatures versus pressure

With $\frac{dv_x}{dy}$ increasing but viscosity decreasing with rising temperatures, it is not clear how the viscous force F_v will respond to an increase in temperature. In order to find the response of F_v it is calculated for different temperatures with the values found for $\frac{dv_x}{dy}$ and μ and is depicted in figure 4.18 below. It is found that the increase of $\frac{dv_x}{dy}$ and the decrease in μ counter each other almost perfectly. Very similar values for F_v versus pressure are found for each temperature, as is seen in figure 4.18, thus F_v is not sensitive to changes in water temperature according to the model.

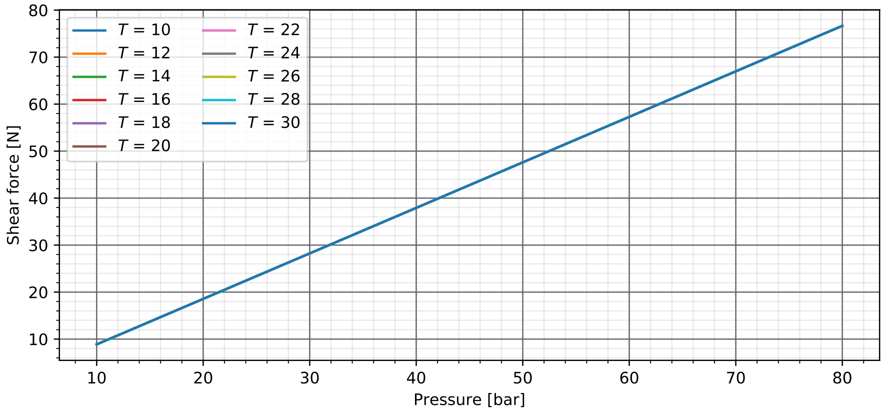

Figure 4.18: Viscous shear force F_v on the piston caused by the leakage fluid film for different fluid temperatures versus pressure

4.5 Alignment of the piston in the cylinder

Through wrongly design or through large side forces the piston can be forced against the cylinder. This scenario has to be taken into account to account for possible extra losses that occur in the pump. The alignment of the piston inside the cylinder determines whether the gap width between them is uniform or alters over the circumference. In figures 4.19 and 4.20 these two scenarios are depicted schematically. When the gap width is uniform it is assumed that the only friction force present is caused by the viscous shear of the fluid film. When misalignment takes place, however, also friction between the piston and cylinder surfaces occurs. In addition to this also friction between the piston rod and piston seal becomes more important. In this section the effects of misalignment on the mechanical and volumetric efficiencies are discussed.

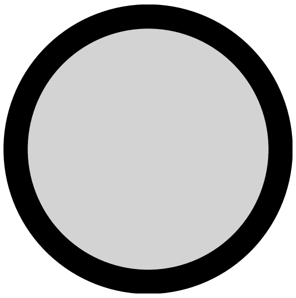

Figure 4.19: Schematic overview of the ideal uniform gap width

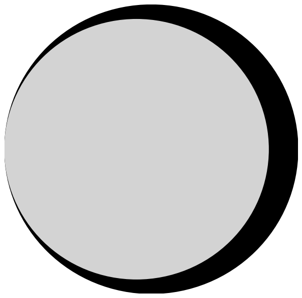

Figure 4.20: Schematic overview of the non uniform gap width possibly caused by misalignment

4.5.1 Effect of alignment on volumetric efficiency

The worst case scenario for piston-cylinder interaction is depicted in figures 2.10 and 2.11. To be able to calculate leakage flow when this worst case scenario occurs, an equation is developed to determine how the non-uniform gap size c alters. The necessary dimensions are depicted in figure 4.21 below. Out of these dimensions, the triangle depicted in figure 4.22 is derived to calculate the altering gap size c.

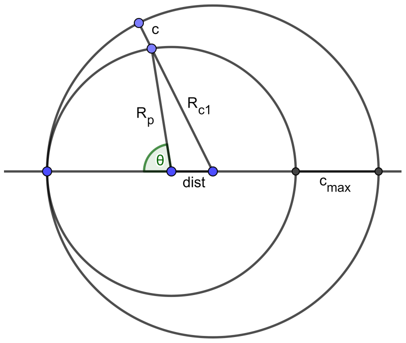

Figure 4.21: Schematic overview of the geometric values necessary to determine gap width c over the circumference

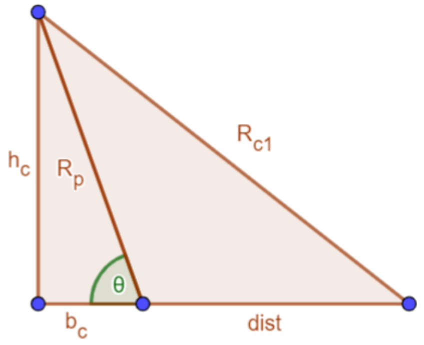

Figure 4.22: Triangle used to calculate the altering gap size c based on figure 4.21

The gap sizes are calculated by solving (4.1), (4.2), (4.3) and (4.4) for θ altering from 0 to 180 [^{o}]. Values R_p and dist are constant, as R_p [m] is the radius of the piston and dist [m] is the distance between the centers of the piston and cylinder. The gapsize c is determined from the radius of the cylinder R_c and the calculated value for R_{c1}.

$$h_c = \sin(\theta) R_p \tag{4.1}$$

$$b_c = \cos(\theta) R_p \tag{4.2}$$

$$R_{c1} = \sqrt{h_c^2 + (b_c + \text{dist})^2} \tag{4.3}$$

$$c = R_c - R_{c1} \tag{4.4}$$

The values found for the gap size c for the test pump are plotted against the increasing angle θ. This is done for the minimum, average and maximum measured gap sizes. The results are depicted in figure 4.23 below and can be incorporated in the model.

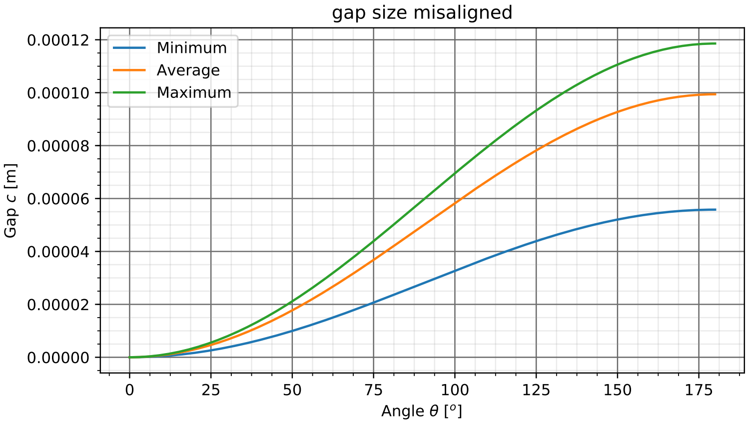

Figure 4.23: The gap sizes c altering with angle θ for the three different measured gap sizes

To depict the influence this misalignment possible has on the volumetric efficiency, the efficiencies for both scenarios are determined at 80 bar for a rotational speed range. The average gap width has been used. The results are visualized in figures 4.24 and 4.25 below. It is seen that the largest difference in efficiency is at 16 rpm, and equals approximately 58%. This emphasizes the need for a well working side force mitigation system which maintains an uniform gap width between the piston and cylinder.

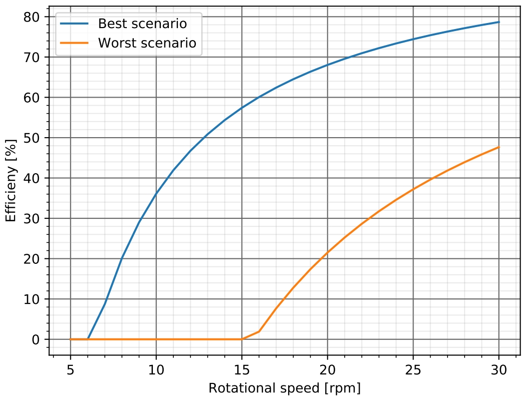

Figure 4.24: The volumetric efficiencies of the two alignment scenarios at 80 bar

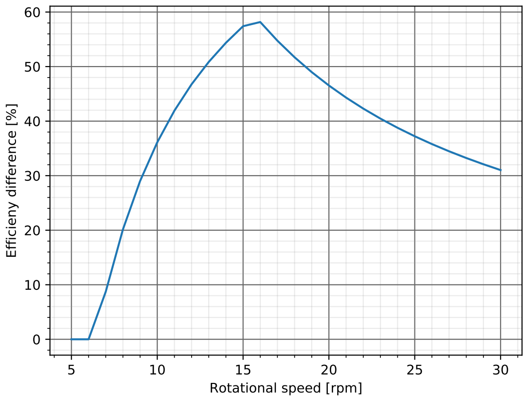

Figure 4.25: The difference in volumetric efficiency of the two alignment scenarios at 80 bar

4.5.2 Effect of alignment on mechanical efficiency

To determine the friction force this interaction creates Coulomb's law of friction described in section 2.7.2 is used.

The force diagram of the misaligned scenario is depicted in figure 4.26 below. The angle of misalignment θ is assumed to be so small that F_p does not have to be adjusted for the angle. The piston rod is assumed to be connected to the piston with a ball joint, which enables the piston to stay horizontally aligned with the cylinder even though the piston rod is not. Also, because the side forces are mitigated by the piston sliding over the cylinder surface for the misaligned scenario, it is assumed that the present side force mitigation system has no interaction with the system.

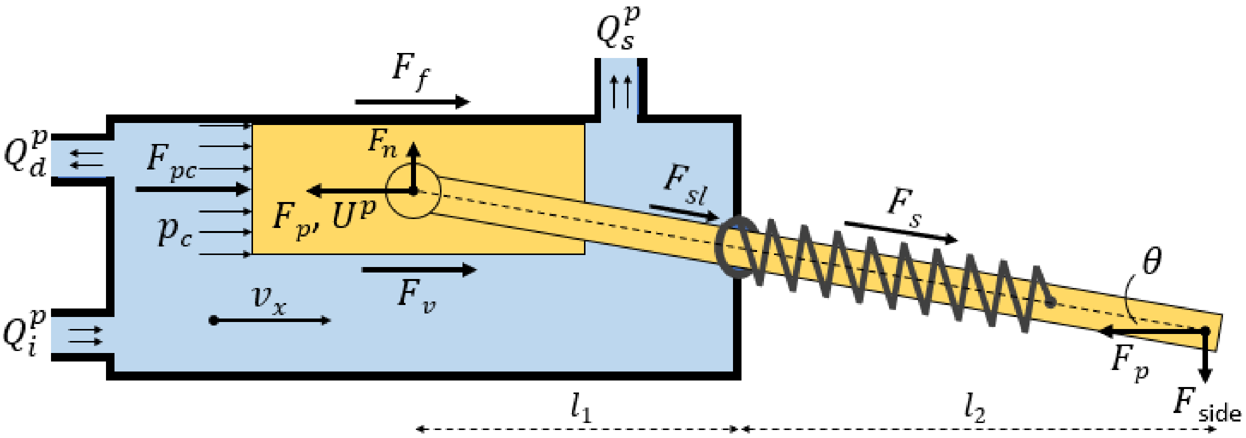

Figure 4.26: Overview of the piston-cylinder interface and the forces resisting movement while misaligned

Axial piston force F_p is determined as in (4.5).

$$F_p = F_{pc} + F_s + F_v + F_f + F_{sl} \tag{4.5}$$

Normal force F_n used in (2.34) is determined from the side force F_{side} and the arms l_1 and l_2.

$$F_n = \frac{l_2 F_{\text{side}}}{l_1} \tag{4.6}$$

It should be noted that these arms alter with the piston strike. It is assumed that the arms are equal in length when the displacement equals half a piston strike.

The seal friction F_{sl} is of more importance in the misaligned scenario. Because the piston rod is using the seal as a point of rotation, the force induced on the seal equals the sum of both forces enacted on the piston ends, i.e. $F_n^{sl} = F_n + F_{\text{side}}$. This potentially increases axial piston force F_p largely as rubber normally has a large coefficient of friction. This added friction force is again estimated using Coulomb's law of friction.

To determine the actual axial piston force profile F_p during one piston strike first the necessary force profile without the friction forces F_f and F_{sl} is determined. Through the angle profile between camring and roller than the side force profile F_{side} during one pistons strike is determined. With the side force the normal force F_n for friction is determined with (4.6). Next (2.34) is used to obtain first estimates of the friction force profiles F_f and F_{sl} during one piston strike. These force profiles are added to the required axial piston force F_p, after which a new estimation of the side force is made. This iteration is continued until the difference in F_p between two iterations is negligible.

The pistons of the test pump are made from natural PEEK. It is found that the friction coefficient μ_k between natural PEEK and stainless steel in water lubricated conditions at a sliding velocity of 0.05 m/s and 12 MPa pressure equals approximately 0.35 [46]. This coefficient is used for calculations. A friction coefficient for rubber similar to the test pump rubber seal material, nitrile rubber 70 shore, of $\mu_k = 1.02 - 2.33$ is found ([47], [48]). As these friction coefficients are for dry running, a value is assumed of $\mu_k = 1$.

The obtained results are depicted below. Figure 4.27 shows the losses due to the rollers present in one piston configuration. In the legend, by 'Normal' the best alignment scenario is meant, thus with a uniform gap width. Lines indicated with 'Misaligned roller' shows what the losses would be in the misaligned scenario if the friction of the piston rod seal would be neglected. Label 'Misaligned roller + seal' shows an estimation of the losses due to misalignment with the piston rod seal friction taken into account.

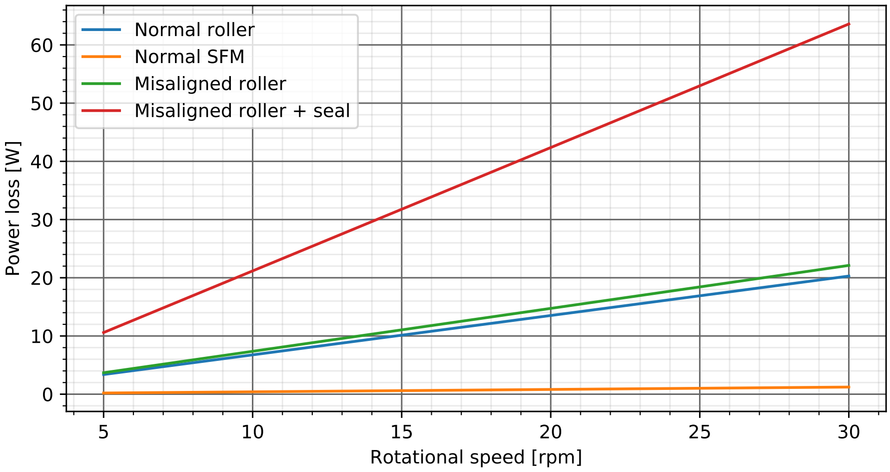

Figure 4.27: The losses in the rollers present in one piston configuration for the two alignment scenarios at 80 bar with $C_r^r = 0.001$

Figure 4.28 shows the losses of the bearings present in one piston configuration for the two different alignment scenarios. The same labels are used as explained above. Figure 4.29 shows the total losses of the bearings and rollers present in one piston configuration for the two different alignment scenarios.

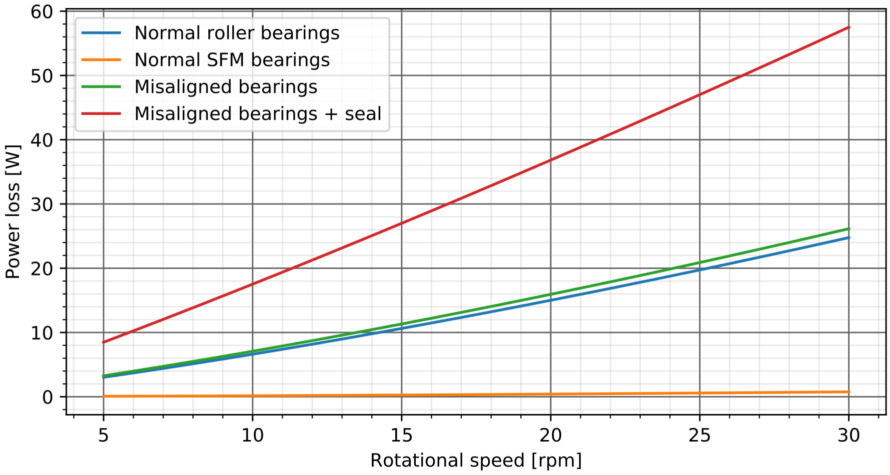

Figure 4.28: The losses in the bearings present in one piston configuration for the two alignment scenarios at 80 bar with $C_r^r = 0.001$

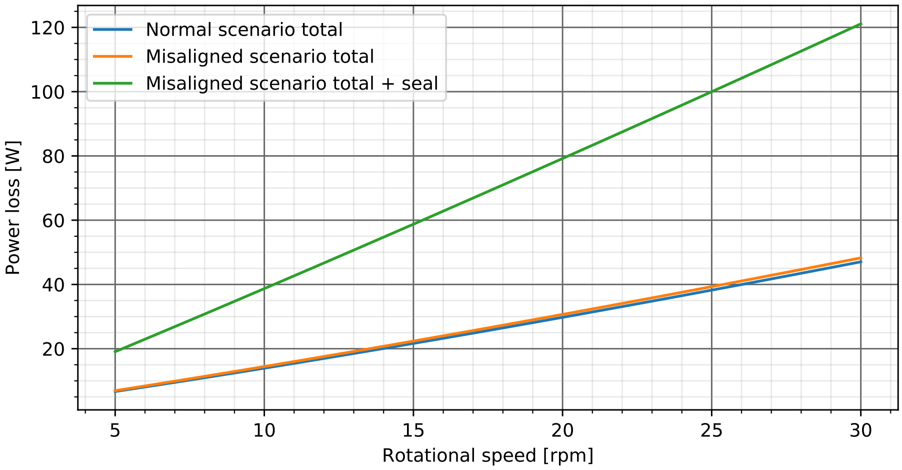

Figure 4.29: The total losses in the rollers and bearings present in one piston configuration for the two alignment scenarios at 80 bar with $C_r^r = 0.001$

It is clear that misalignment negatively influences the mechanical efficiency by causing a larger power loss per piston configuration. It is seen that especially the friction that is caused by the piston rod seal has a major impact on the total losses per configuration. This is because of the high friction coefficient and the large normal force that acts on it. Without these seal friction forces, the changes in total power loss are very small, as is seen clearly in figure 4.29.

To depict the influence this misalignment possibly has on the mechanical efficiency, the efficiencies for both scenarios are determined at 80 bar for a rotational speed range. The average gap width has been used. The results are visualized in figures 4.30 and 4.31 below.

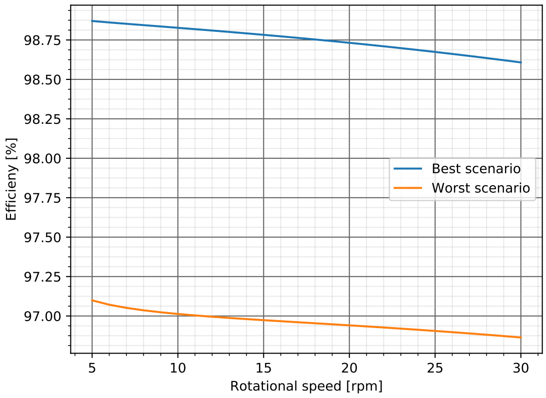

Figure 4.30: The mechanical efficiencies of the two alignment scenarios at 80 bar

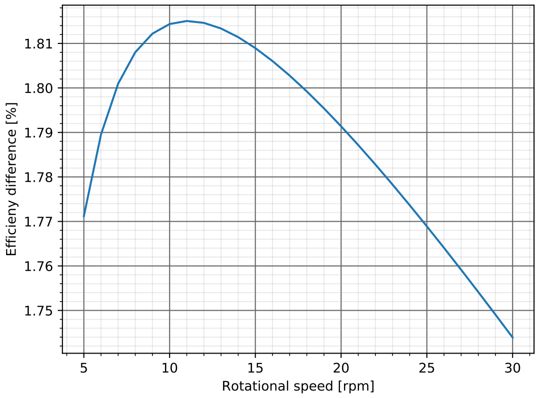

Figure 4.31: The difference in mechanical efficiency of the two alignment scenarios at 80 bar

It is seen that the largest difference in efficiency is approximately 1.81%. Although this is not a considerably large difference, the main problem of misalignment is expected to come from wear. Components which are not designed to handle these kinds of loads now have to mitigate the side forces, possibly breaking them down over time.

To check whether the piston will be able to handle the high side force which act on it during misalignment, a load check is incorporated in the model. Using the method described for rollers, (2.8), (2.9), (2.10), (2.11) and (2.12) are used to check what the maximum contact pressure will be. At 80 bar and 30 rpm, maximum pressure p_{max} is found to be approximately 6.5 MPa. As the compressive strength of PEEK is found to be 135 MPa, the side force should not directly destroy the piston [49].

4.5.3 Effect of alignment on total efficiency

As the volumetric efficiency is affected way more by the misalignment, 58% versus 1.81% difference in mechanical efficiency, the volumetric efficiency dominates the total efficiency. Figures 4.32 and 4.33 show the total efficiencies for both alignment scenarios and their difference. It is seen that the highest difference in efficiency occurs at 16 rpm and is around 58%, following the trend of the volumetric efficiency.

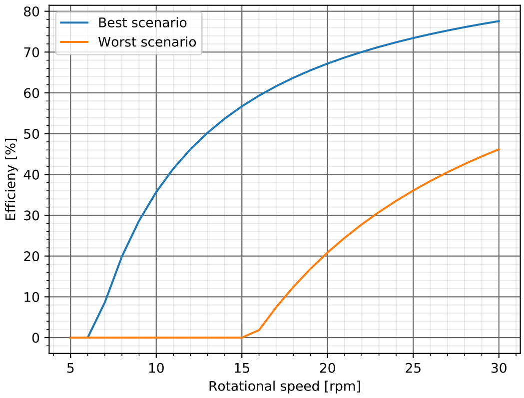

Figure 4.32: The total efficiencies of the two alignment scenarios at 80 bar

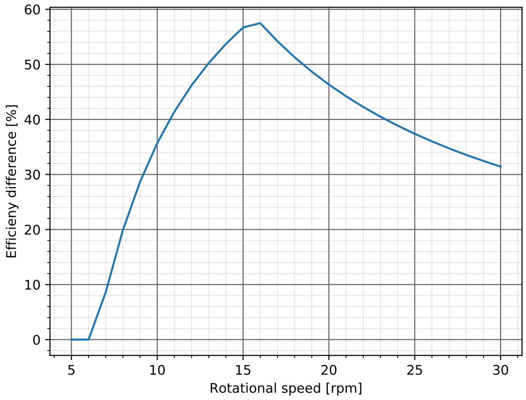

Figure 4.33: The difference in total efficiency of the two alignment scenarios at 80 bar

4.6 Contribution of the different forces resisting piston motion

To get a better understanding of how the total force required to move the piston, F_p, is composed, all of its components are calculated and visualized in this section. This way it is easier to get a better understanding of which components are most important in the analytical analysis of hydraulic pumps. Both the ideal and the misaligned scenario are investigated.

4.6.1 Forces resisting piston movement during ideal alignment

During ideal alignment nothing interesting is observed. As you would expect, the majority of F_p is caused by the force required to overcome the chamber pressure, F_{pc}. Figure 4.34 depicts the contribution of each contributing force at the moment the chamber pressure switches from boost pressure to high pressure. Figure 4.35 shows the forces normalized to total piston force F_p.

To get a better understanding of how the forces develop during one piston strike they are depicted in figure 4.36 at 80 bar and 30 rpm. Figure 4.37 shows the forces during one piston strike normalized to F_p.

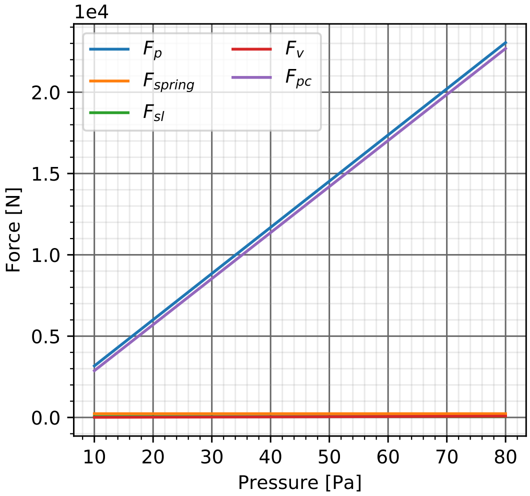

Figure 4.34: All of the forces resisting piston movement just when the chamber pressure switches from boost to high pressure at 30 rpm

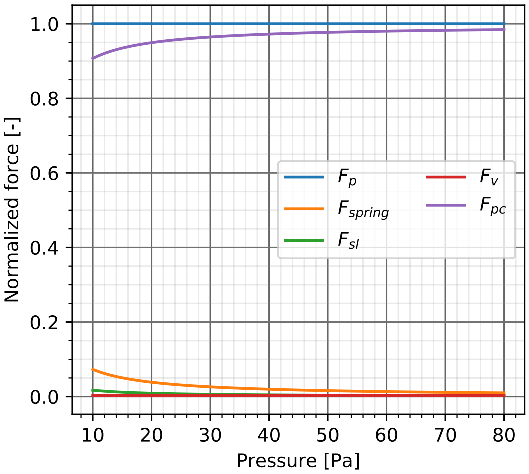

Figure 4.35: All of the normalized forces resisting piston movement just when the chamber pressure switches from boost to high pressure at 30 rpm

It is seen that the contribution of the forces other than F_{pc}, especially the spring force F_s, have a far greater contribution to F_p when the pressure in the chamber equals the boost pressure. When the chamber pressure switches to high pressure it is almost completely dominated by pressure force F_{pc}.

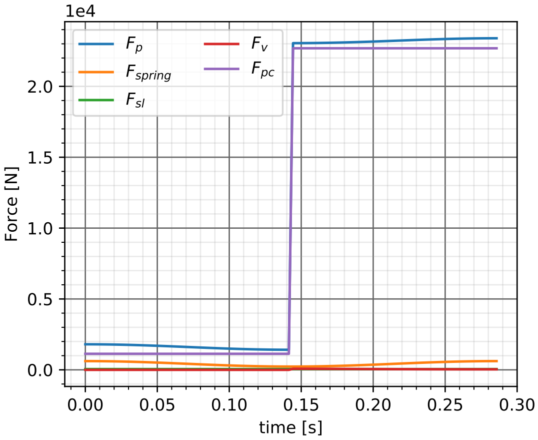

Figure 4.36: All of the forces resisting piston movement during one piston strike during normal alignment at 80 bar and 30 rpm

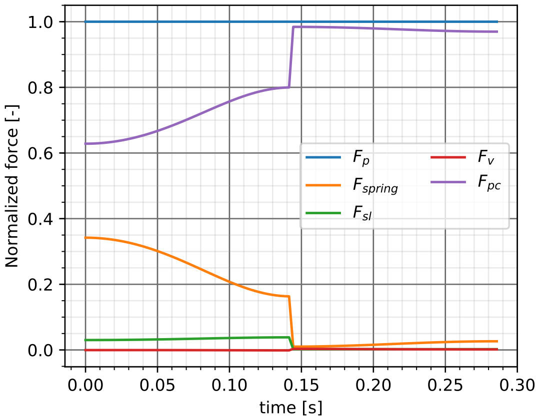

Figure 4.37: All of the forces resisting piston movement during one piston strike during normal alignment at 80 bar and 30 rpm normalized

4.6.2 Forces resisting piston movement during misalignment

The forces contributing to the total piston force F_p during misalignment show a more interesting trend. Figure 4.38 shows the forces contributing to F_p during one piston strike at 80 bar and 30 rpm. Figure 4.39 shows the obtained force profiles normalized to the total force F_p.

As the side forces grow with increasing angle between the roller and camring, the contributions of piston friction force F_f and seal friction force F_{sl} are at their maximum at a maximum camring-roller angle. Since their magnitude is directly dependent on F_p and the angle, the contributions of these friction forces are the same for boost chamber pressure and high chamber pressure. At high chamber pressure, other forces than friction and pressure contribute an insignificant part of the total force F_p.

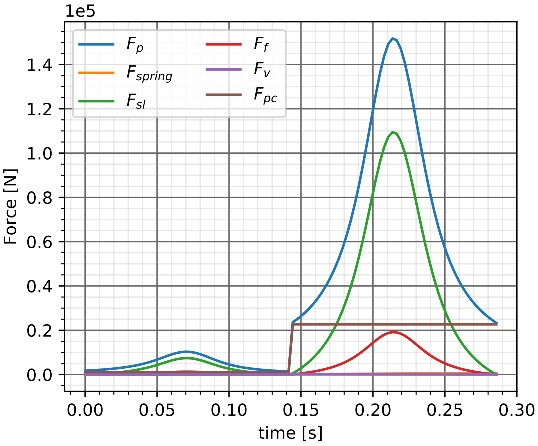

Figure 4.38: All of the forces resisting piston movement during one piston strike during misalignment at 80 bar and 30 rpm

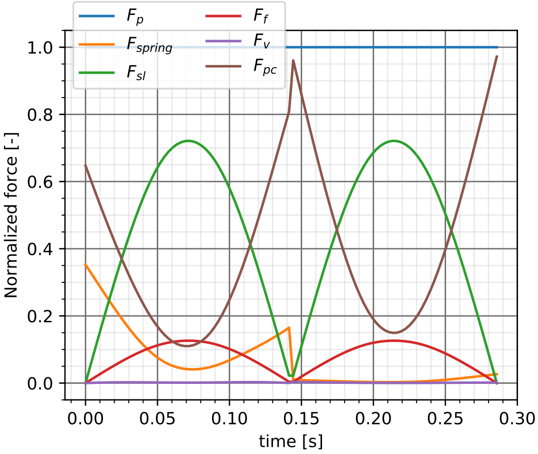

Figure 4.39: All of the forces resisting piston movement during one piston strike during misalignment at 80 bar and 30 rpm normalized

4.7 Laminar flow check of the leakage flow fluid film

To check whether the assumption of laminar flow is valid using the Poiseuille Couette flow described in section 2.6 Leakage, the equation for flow between two plates (2.29) is utilized at maximum operating conditions for the test pump, 80 bar and 30 rpm. It should be checked whether the Reynolds number stays below 2300.

According to (2.26) the maximum Reynolds number is found at the maximum flow velocity. To find the moment during a pistons strike at which maximum leakage flow occurs, the piston velocity and pressure gradient profiles are depicted in figures 4.40 and 4.41.

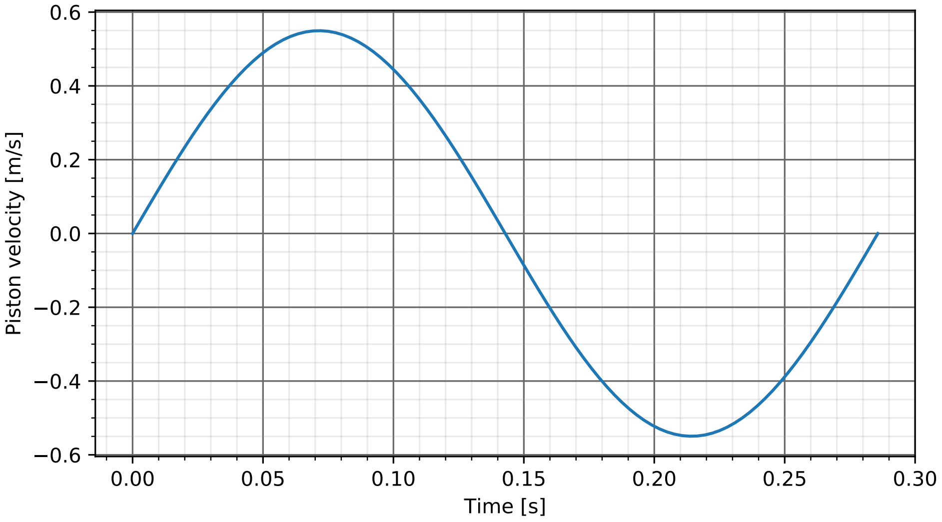

Figure 4.40: The piston velocity during one piston strike at max pump rpm

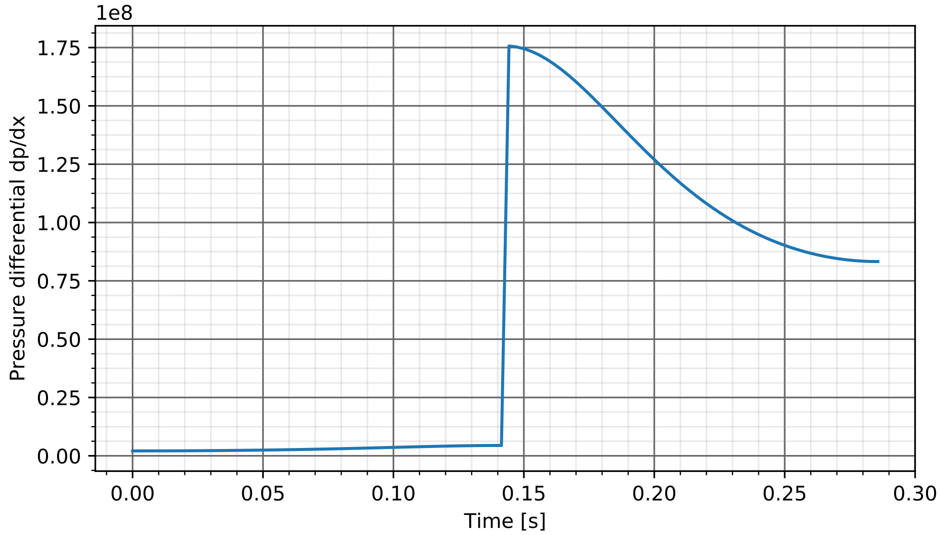

Figure 4.41: The pressure gradient $\frac{dp}{dx}$ over one piston strike at 80 bar and 30 rpm

Three points of interest are investigated to check the flow profile in the leakage flow film. Two points are the largest positive and negative piston velocities that are seen in figure 4.40. Large differences are seen in the flow profile because at the largest positive velocity the chamber pressure equals the boost pressure. At the largest negative velocity however, the chamber pressure equals the pressure of the output port and thus the pressure gradient is significantly larger, resulting in a larger flow. With (2.29) it is found that the highest leakage flow will occur when the pressure gradient is the largest, which results from the smallest flow length shown in figure 4.42.

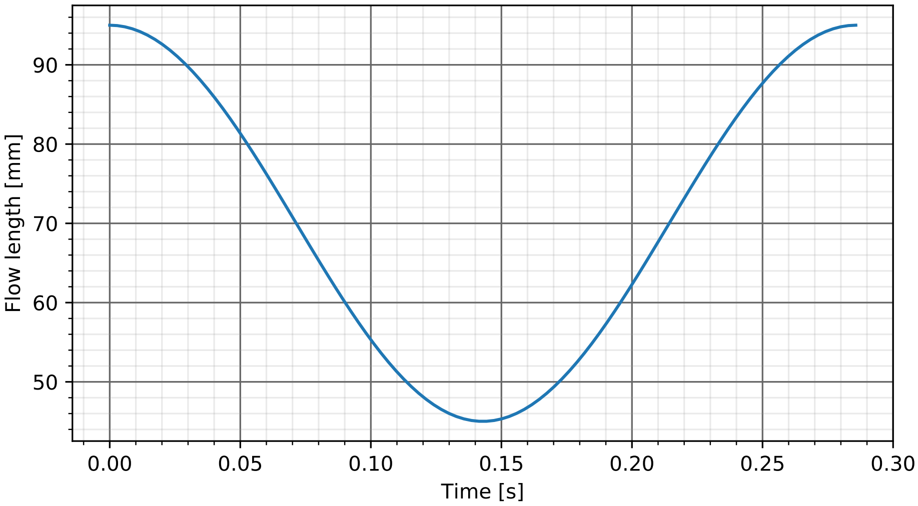

Figure 4.42: The flow length L [mm] alternating during one piston strike

For all three points of interest the flow profile of the fluid film between piston and cylinder is visualized in figure 4.43. It is seen that the highest mean flow velocity is reached with the maximum pressure gradient.

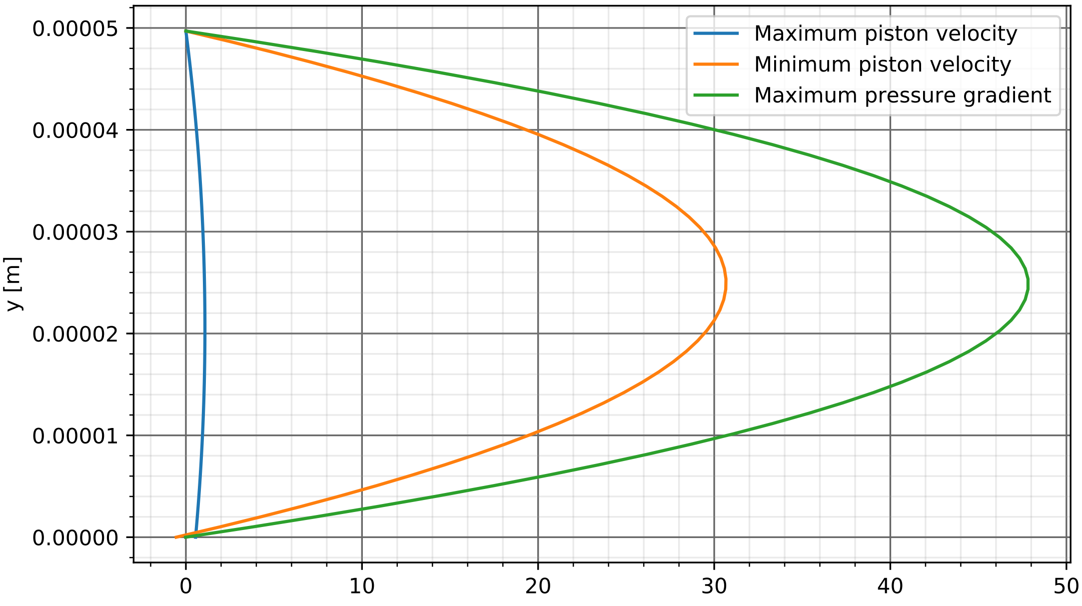

Figure 4.43: The flow profiles in the fluid film between piston and cylinder at three different moments in one piston strike

With the flow profile corresponding to the maximum leakage flow known, (2.26) is used to determine the Reynolds number.

Sources differ in opinion about what should be taken as hydraulic diameter. Some claim it equals $D_H = 2c$ ([50], [51]), while other claim that $D_H = c$ should be used [52]. For both cases the obtained Reynolds numbers are depicted in table 4.1 below.

p=80 [bar], rpm = 30	$v_{x,\text{mean}}$ [m/s]	Reynolds number for:	$D_H = 2c$ [m]	$D_H = c$ [m]
Average gap width	31.24		2746.44	1373.22
Smallest gap width	9.84		485.87	242.93

Table 4.1: Reynolds numbers in the leakage fluid film according to Couette Poisseule flow

It can be seen that for the average measured gap width of the test pump, the found Reynolds value is greater than 2300 if a hydraulic diameter of $D_H = 2c$ is used. When $D_H = c$ is used, Reynolds stays well below 2300. This means that the assumption of laminar flow might not be accurate for every piston-cylinder combination present in the test pump.

The problem, however, is taken away if the pistons are machined more accurately. For the smallest measured gap width, the largest Reynolds number for $D_H = 2c$ found equals to 485.87, which is well within the laminar range.

In table 4.2 the Reynolds number is shown for the largest pressure for which the average gap leakage flow remains laminar, i.e. $Re \leq 2300$. This is found to be at 67 bar.

p=67 [bar], rpm = 30	$v_{x,\text{mean}}$	Reynolds number for:	$D_H = 2c$
Average gap width	26.09		2291.26

Table 4.2: Largest pressure at which flow with average gap width remains laminar

Chapter 5

Effect of Replacing Rollers with Hydrostatic Bearings on Pump Performance

One use of this component-wise model is that components can be replaced to investigate the effect this is expected to have on the pump performance. In chapter 4 it is shown that the rollers and bearings present in the rollers will cause the largest losses in this pump system. Therefore it is very interesting to investigate in components which replace these rollers and bearings to analyze the effect this will have on pump performance. In this chapter it is researched how a hydrostatic bearing should be designed so that the implementation of it will cause an improvement of performance.

5.1 Basic principles of hydrostatic bearings

Hydrostatic bearings are based on inserting a fluid under high pressure between the surface of the bearing and the surface it is separated from. In contrast to hydrodynamic bearings the fluid film in hydrostatic bearings is maintained even though the two surfaces are not in motion relative to each other [13].

Hydrostatic bearings offer a high load capacity and stiffness while offering very low resistance to movement. The fluid film between two surfaces only resists motion through viscous shear as the two surfaces are not supposed to be in contact. To make sure the two surfaces remain separated it is essential that the bearing stiffness is sufficient.

The type of hydrostatic bearing used in this work contains a shallow pocket, in which the fluid is inserted from the source. This means that in this central pocket the pressure distribution is different than in the edges of the bearing. A hydrostatic bearing of this kind is depicted in figure 5.1 below. The pressure of the fluid film over the shallow pocket is assumed to be constant, recess pressure p_r. Over the edges the pressure drops from recess pressure to the pressure which is present outside the bearing system, in this case atmospheric pressure p_a.

To simplify the load capacity calculations of the bearing, the effective area A_e is introduced. The effective area A_e multiplied with p_r should equal to the total load capacity F_c of the bearing, which includes the load capacity of the edges. Figure 5.1 shows a hydrostatic bearing with fluid film thickness h and the pressure distribution in this film, together with the simplification of how effective area A_e is used to calculate the load capacity.

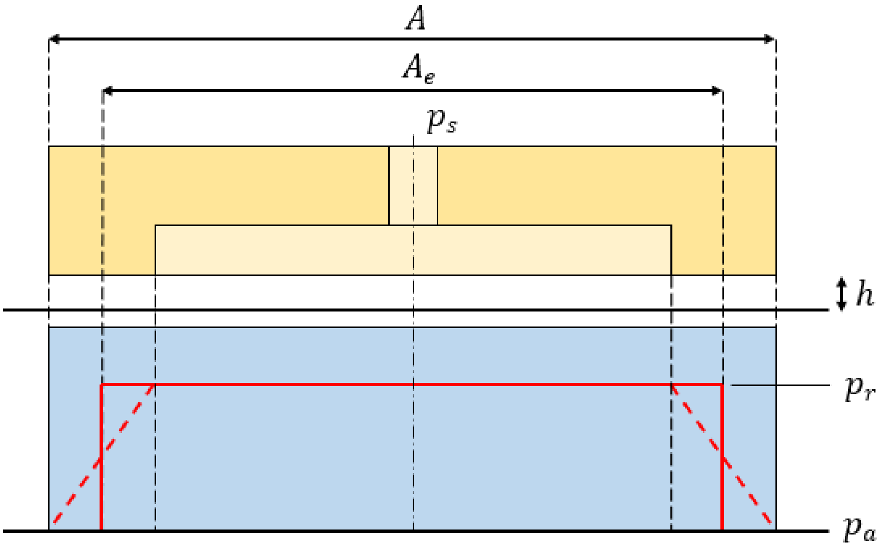

Figure 5.1: A hydrostatic bearing visualized schematically with the principle of effective area A_e and recess pressure p_r

5.2 Design and implementation of a hydrostatic bearing

When designing a hydrostatic bearing it is of importance that the restrictor is chosen accordingly to the operation. The restrictor allows flow to pass from the source to the bearing. By doing so the restrictor lowers the source pressure p_s to the recess pressure p_r, which is the pressure in the fluid film under the bearing. Two different types of restrictors are the capillary and the orifice restrictor, which are depicted schematically with their geometries in figure 5.2 below.

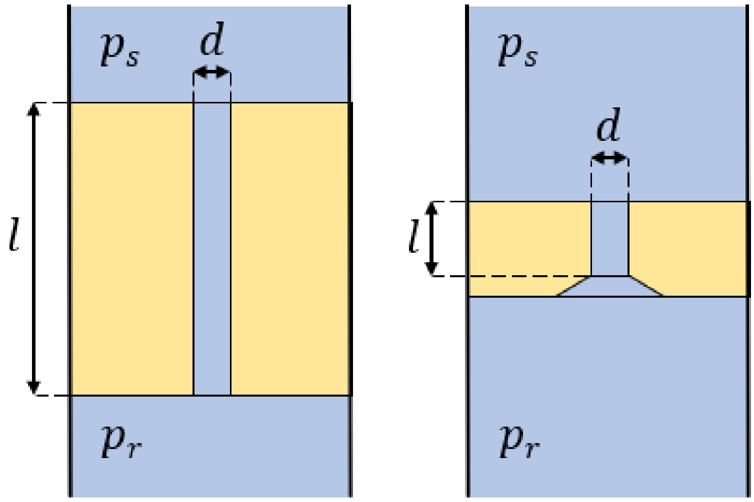

Figure 5.2: The two restrictors depicted schematically with their geometries; left shows the capillary restrictor, right shows the orifice restrictor

Which restrictor should be used depends on the correlation stated in (5.1) below [13]. Reynolds number Re is determined, which depends on fluid density ρ, viscosity μ, flow velocity V and the restrictor diameter d. Furthermore length diameter ratio l/d of the restrictor is to be taken into account.

$$Re = \frac{\rho V d}{\mu} \begin{cases} Re < 1000,\ l/d > 20, & \text{capillary restrictor} \\ Re > 20,\ l/d < 5, & \text{orifice restrictor} \end{cases} \tag{5.1}$$

Before the Reynolds number can be determined, an estimation of the flow Q^{hb} through the bearing during operation must be made. As this flow is dependent on the restrictor used, a bearing is designed with bot restrictors to see whether they are valid for (5.1). The equations stated below are valid for both restrictors unless stated otherwise.

An important variable in the calculations is the the pressure factor β. It is the factor with which the source pressure p_s is lowered to recess pressure p_r and is found with (5.2).

$$\beta = \frac{p_r - p_a}{p_s - p_a} \tag{5.2}$$

To find The load capacity of the bearing the effective bearing area A_e should be known, together with β and p_s. This load capacity should equal the forces induced on the piston rod by the camring. To find a value for effective area A_e, it is calculated using (5.3) for the forces and pressures during one piston strike for a pressure factor of $\beta = 0.5$. This is because the stiffness S of a hydrostatic bearing is greatest around this value for β for a capillary restrictor [13]. For the orifice restrictor, maximum stiffness is obtained at $\beta \approx 0.59$.

$$F_c = A_e \beta (p_s - p_a) \tag{5.3}$$

Figure 5.3 below shows the forces that are induced on the hydrostatic bearing during one piston strike at 80 bar output pressure, which equals the normal forces found for the rollers, F_n^r. These values are used in (5.3) together with β, p_s and p_a to find an appropriate value for A_e.

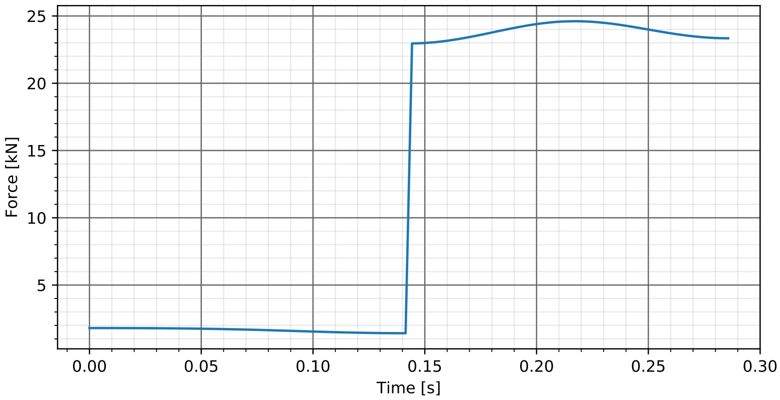

Figure 5.3: The forces induced on the hydrostatic bearing during one piston strike at 80 bar

It is chosen to design a square bearing for this application. The shape of the bearing determines the equations used to determine flow through the bearing. To determine the effective area of a square hydrostatic bearing, lengths L_0 and L_1 are necessary, which are depicted in figure 5.4 below.

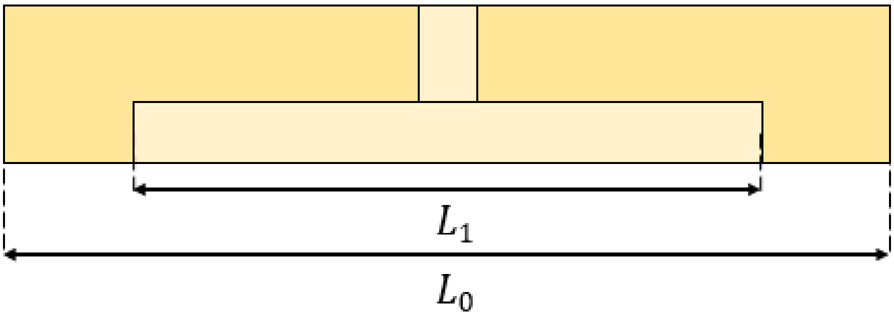

Figure 5.4: Necessary geometry of a square hydrostatic bearing to determine the effective area A_e

The effective area A_e of the bearing is obtained through (5.4).

$$A_e \approx \frac{L_0^2 + L_1^2}{2} \tag{5.4}$$

For this design it is assumed that L_1 equals $0.6L_0$. Using this assumption, (5.4) is used to determine L_0, as in (5.5).

$$L_0 = \sqrt{\frac{2A_e}{1.36}} \tag{5.5}$$

The film factor C_F is determined by the film geometry, and thus the bearing geometry and is found with (5.6).

$$C_F = \frac{1}{3}\frac{1 + L_1/L_0}{1 - L_1/L_0} \tag{5.6}$$

Consequently the flow through the bearing is determined using the values determined above, plus the value for the film thickness h [m]. How the film thickness is determined depends on the restrictor used. Bearing flow Q^{hb} [m^3/s] is found with (5.7).

$$Q^{hb} = \frac{h^3}{\mu}\beta(p_s - p_a)C_F \tag{5.7}$$

When designing a hydrostatic bearing it is important to make sure that the stiffness is sufficient to withstand the load. Therefore, to easily compare stiffness to load capacity, dimensionless stiffness $S^{'}$ and load capacity $F_c^{'}$ are introduced. Dimensionless stiffness is determined as in (5.8). Stiffness S is determined differently for the two restrictors and is discussed in their individual sections. Area A is the total bearing area and is determined as $A = L_0^2$.

$$S^{'} = \frac{Sh}{A(p_s - p_a)} \tag{5.8}$$

The dimensionless load capacity $F_c^{'}$ is determined with (5.9).

$$F_c^{'} = \frac{F_c}{A(p_s - p_a)} \tag{5.9}$$

Following the restrictor type specific equations are given and the restrictor dependent effective area A_e will be determined.

5.2.1 Hydrostatic bearing with capillary restrictor

Following (5.3), using the values for the force induced on the bearing depicted in 5.3 at 80 bar, 30 rpm, the effective area A_e is determined during one piston strike to comply to the β value which offers the greatest stiffness, $\beta = 0.5$. In figure 5.5 the values for A_e found are visualized. Based on this an effective area of $A_e = 0.01$ m^2 is chosen, to obtain acceptable values for β during one piston strike. A common value for β for use with capillary restrictors is between $1/3 - 2/3$ [13]. How β alters during one piston strike with this A_e is depicted in figure 5.6.

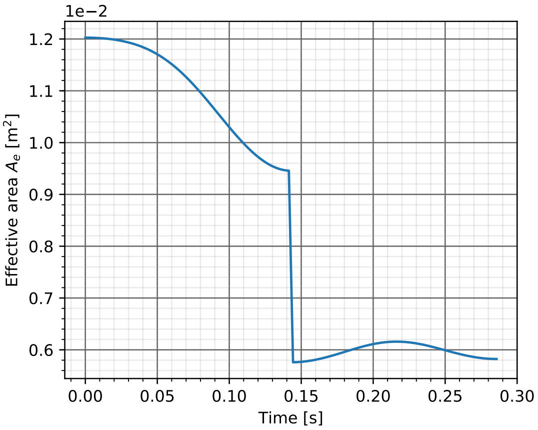

Figure 5.5: How the effective area A_e alters during one piston strike to comply to $\beta = 0.59$

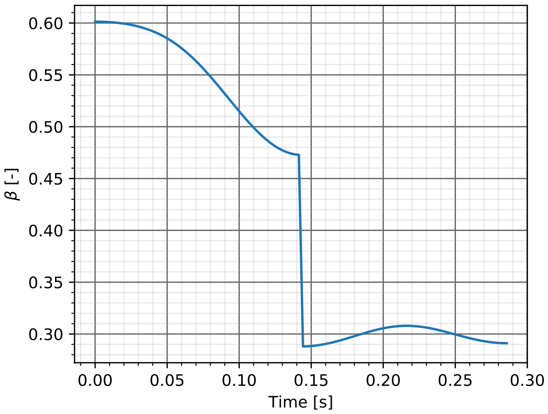

Figure 5.6: How β alters during one piston strike with an effective area of $A_e = 0.01$ m^2

The film thickness h is expressed using the geometry factor g, which is determined differently for the two types of restrictors. For the capillary restrictor, this geometry factor is dependent on the length l [m] and diameter d [m] of the restrictor, and the film factor C_F. Equation (5.10) is found.

$$g = \frac{128l}{d^4} C_F \tag{5.10}$$

The film thickness can consequently be determined with this geometry factor g and the pressure factor β as in (5.11).

$$h = \left(\frac{1-\beta}{\beta g}\right)^{\frac{1}{3}} \tag{5.11}$$

With the film thickness h known the total bearing flow Q^{hb} can be found using (5.7). Now all necessary values to determine the bearing stiffness are known and is found with (5.12).

$$S = A_e(p_s - p_a)\frac{3}{h}\beta^2\frac{(1-\beta)}{\beta} \tag{5.12}$$

The dimensionless stiffness $S^{'}$ can now be determined with (5.8) and the dimensionless load capacity can be determined using (5.9). The value of the ratio $S^{'}/F_c^{'}$ is supposed to alter between 2 and 1 for a β value between $1/3 - 2/3$.

5.2.2 Hydrostatic bearing with orifice restrictor

Following (5.3), using the values for the force induced on the bearing depicted in 5.3 at 80 bar, 30 rpm, the effective area A_e is determined during one piston strike to comply to the β value which offers the greatest stiffnes, $\beta = 0.59$. The values for A_e shown in figure 5.7 are obtained. From the range of values for A_e seen, $A_e = 0.009$ m^2 is chosen, as this seems to give the best values for β over one piston strike. A common value for β for use with orifice restrictors is between $1/3 - 2/3$ [13]. The values for β depicted in figure 5.8 are obtained using this value for A_e.

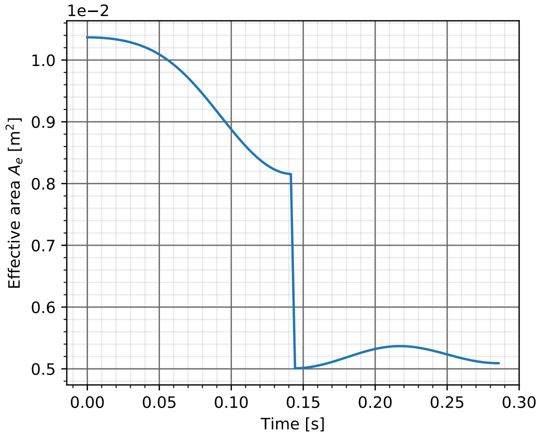

Figure 5.7: How the effective area A_e alters during one piston strike to comply to $\beta = 0.59$

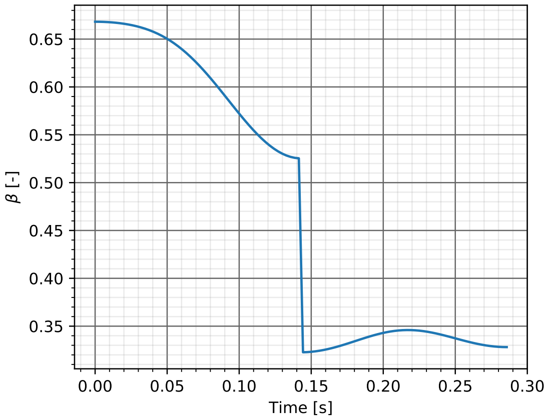

Figure 5.8: How β alters during one piston strike with an effective area of $A_e = 0.009$ m^2

To determine the geometry factor g for the orifice restrictor, the geometry, length l and width d, are represented by the constriction coefficient C_D. It is found that for higher Reynolds numbers, $Re > 200$, and a length width factor of $l/d < 1.4$, the constriction coefficient approximates $C_D = 0.7$ [13]. The geometry factor is found with (5.13).

$$g = \frac{C_F}{\mu C_D A_W}\sqrt{\frac{\rho(p_s - p_a)}{2}} \tag{5.13}$$

The film thickness is consequently found similar to how it is found for the capillary restrictor, except that a square root is introduced in the equation. Equation (5.14) is obtained.

$$h = \left(\frac{\sqrt{1-\beta}}{\beta g}\right)^{\frac{1}{3}} \tag{5.14}$$

With (5.7) the total flow over the bearing can now be calculated. The stiffness of the hydrostatic bearing utilizing the orifice restrictor can now be found with (5.15).

$$S = 6\frac{F_c}{h}\frac{1-\beta}{2-\beta} \tag{5.15}$$

With the stiffness determined (5.8) is used to determine the dimensionless stiffness S' and (5.9) is used to determine the dimensionless load capacity F_c'. The ratio S'/F_c' is supposed to alter between 2.2 and 1.5 for a β value between $1/3 - 2/3$.

5.3 Least square fit to find mimimum hydrostatic bearing parameters for performance improvement

To find the design parameters for the hydrostatic bearings so that their implementation will actually cause an improvement of the performance, a least square fit is used. This fit has both a mechanical and volumetric part, which are both discussed. These are combined to form the total efficiency, which should approximate the total efficiency of the system using rollers.

To find the parameters for the design of both restrictor types, average values for input variables during one piston strike are used. This is because the fit would become too complex if certain input variables would consist of 100 vector elements to describe 1 piston strike. Thus, for each operational condition, the average values for normal force on the roller or hydrostatic bearing F_n^r, roller velocity v_r^r and chamber pressure p_c are found.

5.3.1 Volumetric functions necessary for fitting the hydrostatic bearing functions

The volumetric efficiency map of the test pump for all operational conditions has been determined with the model. The leakage flow per piston at each condition is determined by rewriting 3.25 to (5.16).

$$Q_s^p = Q_i^p - \eta_v Q_i^p \tag{5.16}$$

With (5.7) the water extracted from the cylinder which is necessary to lift the hydrostatic bearing with height h above the camring surface is determined. The total leakage flow per piston which determines the volumetric efficiency in this system can thus be found as in (5.17).

$$Q_{s,\text{hydro}}^p = Q_s^p + Q^{hb} \tag{5.17}$$

The volumetric efficiency can then be determined with (5.18).

$$\eta_v = \frac{Q_i^p - Q_{s,\text{hydro}}^p}{Q_i^p} \tag{5.18}$$

These functions are necessary for the parameter fit to be performed and can be solved when the values for the parameters are found.

5.3.2 Mechanical functions necessary for fitting the hydrostatic bearing functions

First, the mechanical efficiency map for all operating conditions of the test pump with the roller system is found using the model. Also the total power losses caused by the rollers and appurtenant bearings for each operating condition are found, P_r^{tot}. The ideal output torque T_p is found for each condition with (3.28). Torque loss T_s can consequently be determined by rewriting (3.26) to (5.19).

$$T_s = \frac{T_p}{\eta_m} - T_p \tag{5.19}$$

The total power loss $P_{\text{loss}}^{\text{rollers}}$ in the pump with rollers for each condition can then be found by rewriting (3.29) to (5.20) with n_{cr} [rpm] being the rotational speed of the pump.

$$P_{\text{loss,rollers}} = T_s \omega_p = T_s \frac{2\pi \cdot n_p}{60} \tag{5.20}$$

The mechanical power losses inside the pump without the rollers is then found as the additional power loss P_{add} [W], and is determined with 5.21.

$$P_{\text{add}} = P_{\text{loss,rollers}} - P_r^{\text{tot}} \tag{5.21}$$

To determine the power loss due to the hydrostatic bearing the fluid film flow Q^{hb} is described by Poiseuille Couette flow. Because the bearing is symmetric, and the fluid is fed to the bearing in the center of the bearing, the friction forces induced on the bearing by this Poiseuille flow are assumed to cancel each other out. Therefore the only force that resists the movement of the bearing is the friction caused by the movement of the bearing itself. The flow pattern induced by the movement of the bearing is described by Couette flow as in (5.22).

$$v_x(y) = v_h(\frac{d-y}{d}) \tag{5.22}$$

The point of interest is at the bearing surface, thus close to $y = 0$. With v_h as the velocity with which the bearing moves over the camring, which equals rolling velocity v_r^r, $\frac{dv_x}{dy}$ can be found close to the bearing surface. Consequently the friction force can than be determined using (2.33), with A_b being the bearing area. The power loss per piston configuration due to this friction force is than found with the correlation defined in (5.23).

$$P_v = A_b \mu \frac{dv_x}{dy} v_h \tag{5.23}$$

The total mechanical power loss in the pump with hydrostatic bearings $P_{\text{loss,hydro}}$ can then be determined by adding the total power loss due to viscous shear P_v^{tot} to the additional power loss P_{add}, which was determined earlier, as in (5.24).

$$P_{\text{loss,hydro}} = P_{\text{add}} + P_v^{\text{tot}} \tag{5.24}$$

With this total mechanical power loss with hydrostatic bearings known for each operational condition the new mechanical efficiency map can be constructed. The new torque loss T_s is found with (5.25).

$$T_s = \frac{P_{\text{loss,hydro}}}{\omega^{cr}} = \frac{60}{2\pi \cdot n_{cr}} P_{\text{loss,hydro}} \tag{5.25}$$

Consequently the new mechanical efficiencies can be calculated with (3.26). These functions are necessary for the execution of the least square fit to find the right values for the design parameters. When these values are found, the functions in this section can be solved.

5.3.3 Fitting hydrostatic bearing functions

To know for what design parameters the implementation of hydrostatic bearings improves the performance of the test pump a least square curve fit is used. For this the total efficiency map for each operational condition while rollers are used is obtained with the model. The hydrostatic bearing should be designed so that the new volumetric and mechanical efficiencies combine to approximate the total efficiency of the old system as precise as possible, as in (5.26).

$$\eta_t = \eta_v \eta_m \tag{5.26}$$

For each restrictor type the to be fitted parameters are found. For both restrictor types the effective area A_e is found beforehand, since they are chosen to get a optimal value for β for both restrictor types.

For the capillary restrictor it is found that, with A_e fixed, the fluid film height h depends on the restrictor diameter d and length l, as can be seen in (5.10) and (5.11). To find the values for d and l, the capillary restrictor functions together with the functions necessary to describe the new mechanical and volumetric efficiencies are fitted to approximate the total efficiencies found for the pump using rollers.

The same is done for the orifice restrictor, with as only difference that fluid film height h is only dependent on restrictor diameter d for this type of restrictor.

5.4 Results of the parameter fit

In this section the result of the parameter fit is discussed for both restrictor types. Fluid film heights, total flows, stiffnesses, Reynolds numbers an efficiencies are determined and visualized. All of the figures which depict one piston strike represent one piston strike at 80 bar output pressure and 30 rpm pump rotational speed.

5.4.1 Capillary restrictor

For the capillary restrictor both the restrictor diameter d and length l are fitted to obtain the total efficiencies of the pump utilizing hydrostatic bearings for all operational conditions as close as possible to the total efficiencies of the pump utilizing rollers. The values $d = 0.147$ mm and $l = 4.425$ mm are found. Now, with (5.10) and (5.11), fluid film height h during one piston strike is calculated and depicted in figure 5.9. Consequently (5.7) is used to determine the total fluid flow Q^{hb} of the bearing during one piston strike, which is shown in figure 5.10 below.

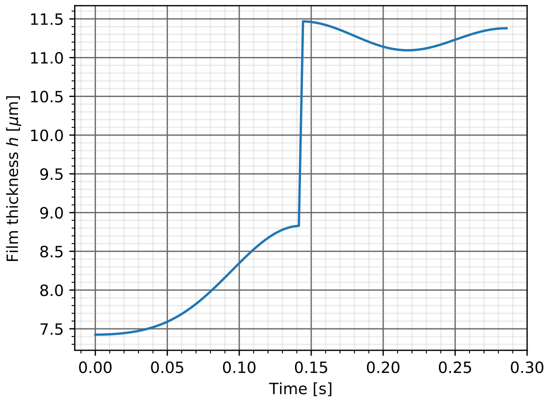

Figure 5.9: How the film thickness h alters during one piston strike at 80 bar output pressure and 30 rpm rotational speed

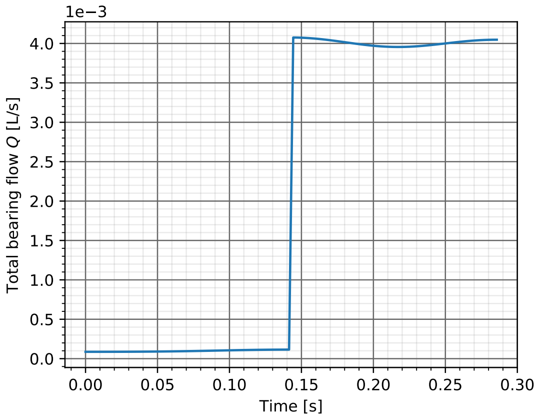

Figure 5.10: How the total bearing flow Q^{hb} alters during one piston strike at 80 bar output pressure and 30 rpm rotational speed

With h known, the stiffness S of the bearing can be calculated. But more importantly is how the stiffness compares to the load capacity F_c. Therefore dimensionless stiffness $S^{'}$ and dimensionless load capacity $F_c^{'}$ are determined with (5.8) and (5.9). The factor $S^{'}/F_c^{'}$ is depicted in figure 5.11. With Q^{hb} and d known, the Reynolds number of the flow through the restrictor can be determined. This is depicted in figure 5.12.

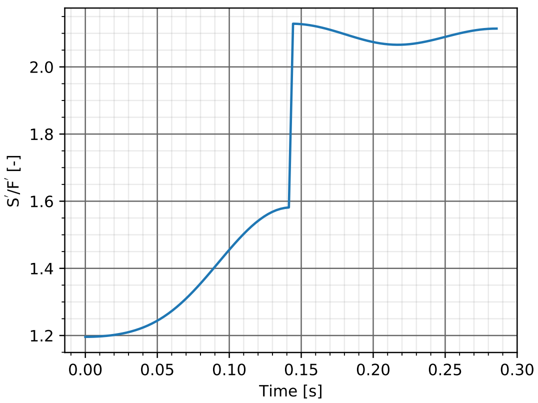

Figure 5.11: How the $S^{'}/F^{'}$ ratio alters during one piston strike at 80 bar output pressure and 30 rpm rotational speed

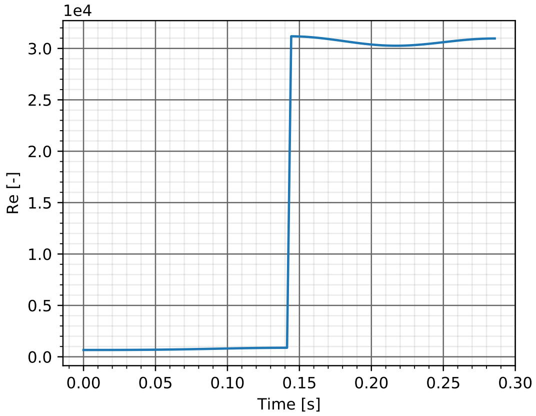

Figure 5.12: How the Reynolds number alters during one piston strike at 80 bar output pressure and 30 rpm rotational speed

In (5.1) the constraints for using a capillary restrictor are given. The constraint of $Re < 1000$ is obviously crossed, meaning that this type of restrictor is no feasible. Nevertheless, the viscous shear forces F_v corresponding to the film heights h and velocities v_h for one piston strike are given in figure 5.13. The mechanical power losses corresponding to these shear forces, P_v, during one piston strike are depicted in figure 5.14.

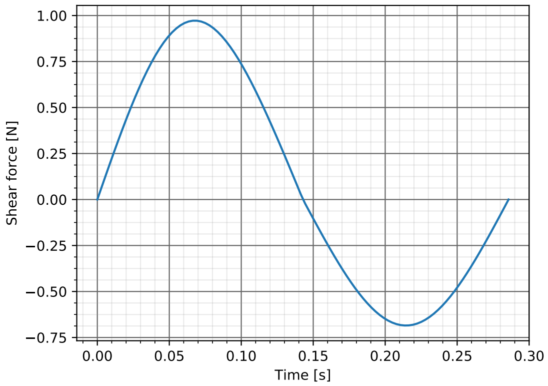

Figure 5.13: How shear force alters during one piston strike at 80 bar output pressure and 30 rpm rotational speed

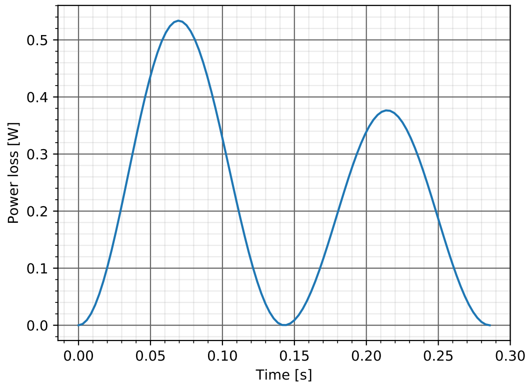

Figure 5.14: How the power loss alters during one piston strike at 80 bar output pressure and 30 rpm rotational speed

The volumetric efficiency map for all operational conditions achieved with bearing flow Q is depicted in figure 5.15. The mechanical efficiency map is depicted in figure 5.16. The total efficiency map obtained by combining the volumetric and mechanical efficiency is depicted in figure 5.17.

The total efficiency map for the pump with rollers is given in figure 5.34 which can be found in the orifice section. It is seen that the efficiency maps correspond well, but are not identical. An exact duplication cannot be achieved because the functions for the roller setup and hydrostatic setup behave differently under different conditions.

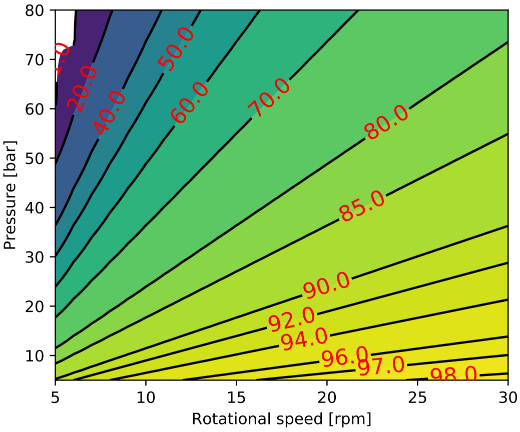

Figure 5.15: The volumetric efficiencies of the test pump utilizing hydrostatic bearings with a capillary restrictor at all operating conditions

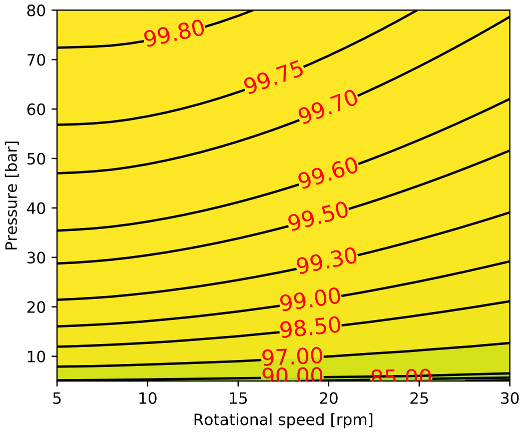

Figure 5.16: The mechanical efficiencies of the test pump utilizing hydrostatic bearings with an capillary restrictor at all operating conditions

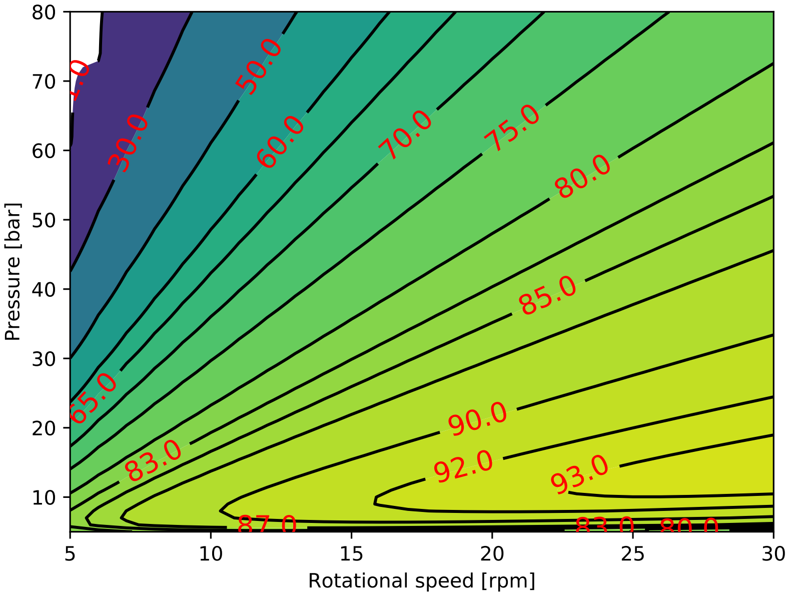

Figure 5.17: The total efficiencies of the test pump utilizing hydrostatic bearings with an capillary restrictor at all operating conditions

5.4.2 Orifice restrictor

For the orifice restrictor only the restrictor diameter d is fitted to obtain total efficiencies of the pump utilizing hydrostatic bearings as close as possible to the total efficiencies of the pump utlizing rollers. The value $d = 0.239$ mm is found. Next, with (5.13) and (5.14), fluid film height h during one piston strike is calculated and depicted in figure 5.18 below. Then (5.7) is used to determine the total fluid flow Q^{hb} of the bearing during one piston strike. This is depicted in figure 5.19 below.

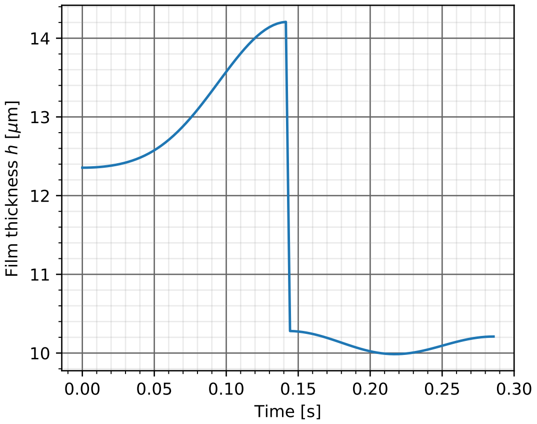

Figure 5.18: How the film thickness h alters during one piston strike at 80 bar output pressure and 30 rpm rotational speed

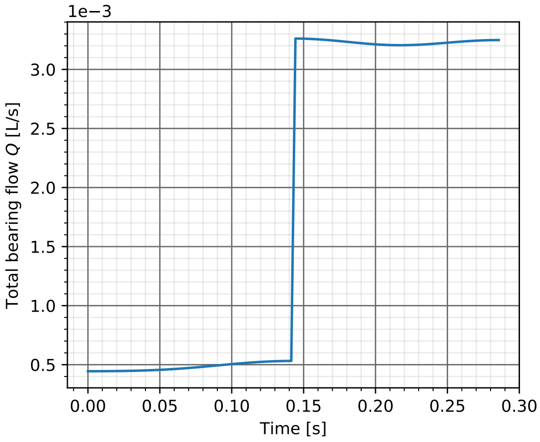

Figure 5.19: How the total bearing flow Q^{hb} alters during one piston strike at 80 bar output pressure and 30 rpm rotational speed

Stiffness S of the bearing can be calculated now that h is known. Again, dimensionless stiffness $S^{'}$ and dimensionless load capacity $F_c^{'}$ are determined with (5.8) and (5.9). The factor $S^{'}/F_c^{'}$ is depicted in figure 5.20 below. Furthermore, with Q^{hb} and d known, the Reynolds number of the flow through the restrictor is determined. This is depicted in figure 5.21.

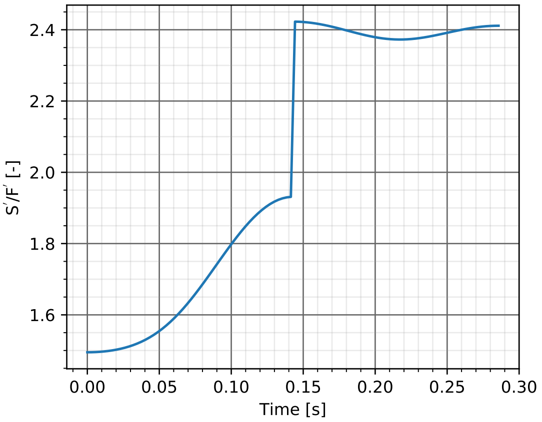

Figure 5.20: How the $S^{'}/F_c^{'}$ ratio alters during one piston strike at 80 bar output pressure and 30 rpm rotational speed

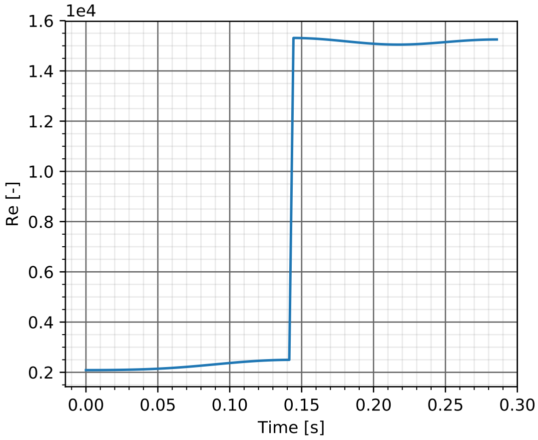

Figure 5.21: How the Reynolds number alters during one piston strike at 80 bar output pressure and 30 rpm rotational speed

Next the viscous shear force F_v and its corresponding power loss P_v are determined for the found values of h. The shear force is depicted in figure 5.22, the mechanical power loss is visualized in figure 5.23.

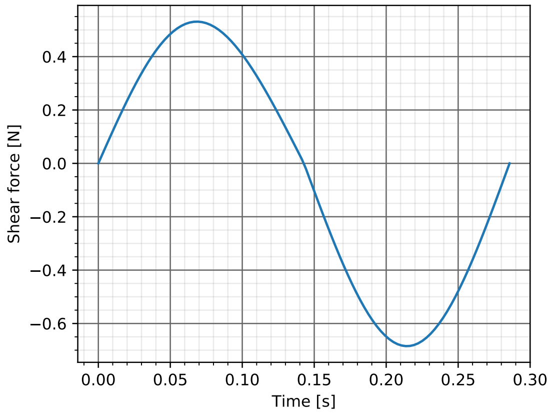

Figure 5.22: How shear force alters during one piston strike at 80 bar output pressure and 30 rpm rotational speed

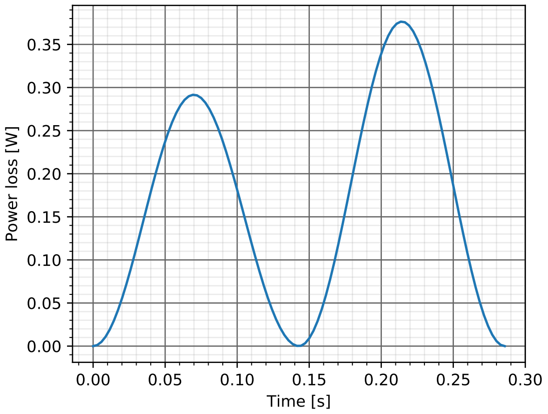

Figure 5.23: How the power loss alters during one piston strike at 80 bar output pressure and 30 rpm rotational speed

The bearing feed flow Q^{hb} to maintain a film height h between the bearing and camring surface lowers the volumetric efficiency of the system. To obtain the same total efficiency for the operational envelope of the test pump, however, this film height h and thus Q^{hb} has to be kept low. The average fluid film height is 12.18 μm which leads to an average bearing flow of 0.0016 L/s, while the average leakage flow for all conditions equals 0.057 L/s. This leads to a small difference in volumetric efficiency. The volumetric efficiencies for all operational conditions are depicted for both systems. The volumetric efficiencies of the system utilizing hydrostatic bearings are visualized in figure 5.24, those of the system utilizing rollers are shown in figure 5.25.

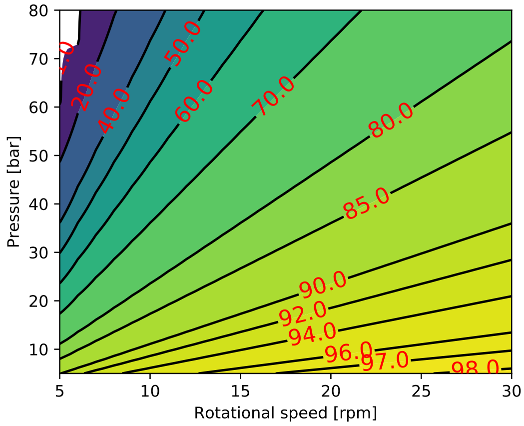

Figure 5.24: The volumetric efficiencies of the test pump utilizing hydrostatic bearings with an orifice restrictor at all operating conditions

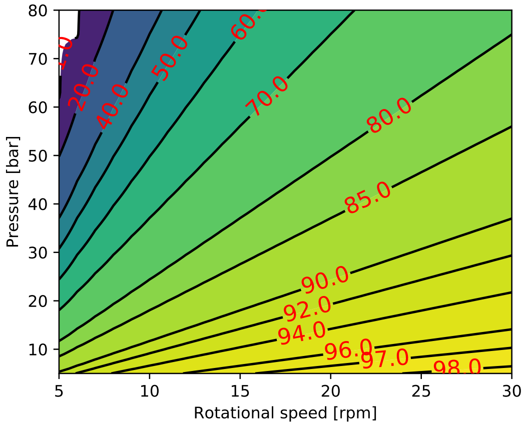

Figure 5.25: The volumetric efficiencies of the test pump utilizing rollers at all operating conditions

The total leakage losses of the hydrostatic bearing, thus the losses due to leakage between piston and cylinder with the bearing feed flow, is what determined the volumetric efficiencies depicted in figure 5.24. These total leakage flows per piston for each operational condition are given in figure 5.26 below. The total leakage flows per piston of the system utilizing rollers, which determine the volumetric efficiencies depicted in figure 5.25, are shown in figure 5.27.

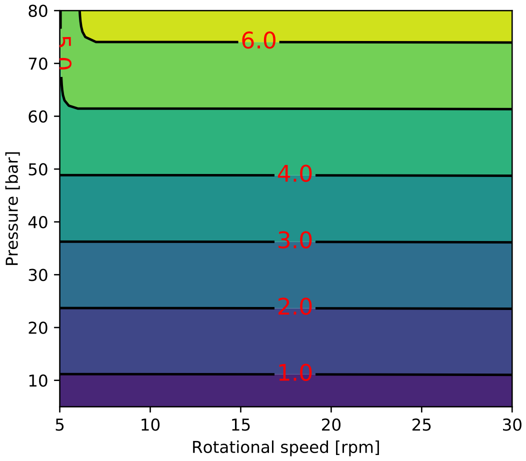

Figure 5.26: The total leakage flows [L/min] per piston configuration for a system utilizing hydrostatic bearings for all operational conditions

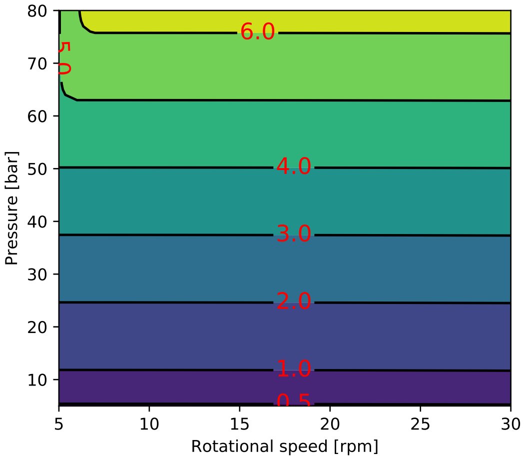

Figure 5.27: The total leakage flows [L/min] per piston configuration for a system utilizing rollers for all operational conditions

It is seen that the leakage losses for both systems are very similar, and changes primarily with rising output pressure. The losses for the system utilizing hydrostatic bearings are slightly higher for each pressure.

The curve which is seen in the top left corners of figures 5.26 and 5.27, at high pressure and low rotational speed, can be explained by investigating the ideal discharge flows of one piston for each operational condition, which are depicted in figure 5.28 below. The leakage flow can obviously not be higher than the ideal discharge flow, as there would be no water left in the cylinder.

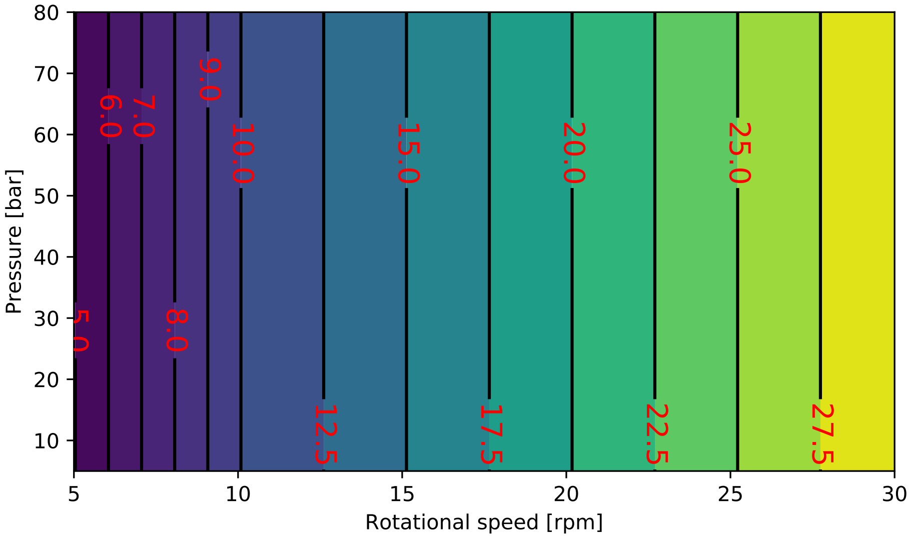

Figure 5.28: The ideal discharge flows [L/min] per piston configuration for all operational conditions

The mechanical power losses in the hydrostatic bearings are expected to be significantly lower than those in rollers. However, at the operational conditions of the test pump, the mechanical efficiencies of the system using rollers are already estimated to be very high, as is depicted in figure 5.30. The mechanical efficiencies of the system utilizing hydrostatic bearings are visualized in figure 5.29.

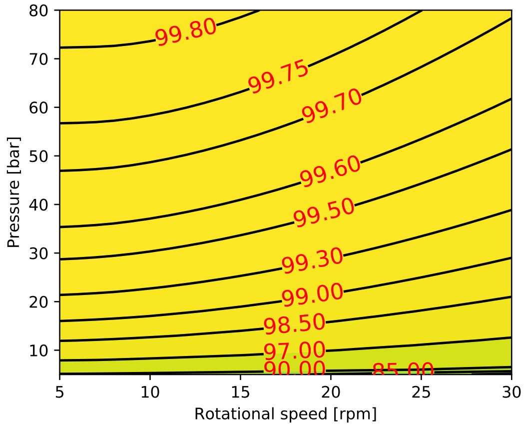

Figure 5.29: The mechanical efficiencies of the test pump utilizing hydrostatic bearings with an orifice restrictor at all operating conditions

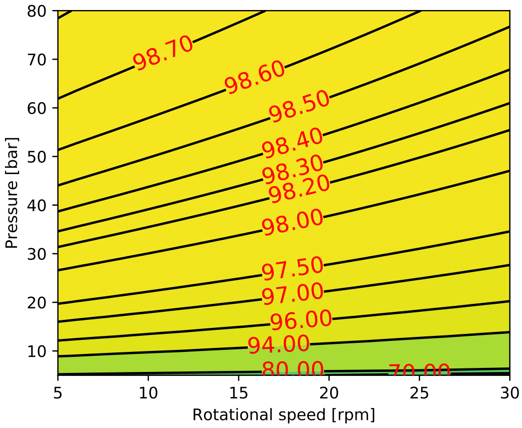

Figure 5.30: The mechanical efficiencies of the test pump utilizing rollers at all operating conditions

The improvement in mechanical efficiency does not appear to be very high when the two figures are compared. As an efficiency shows the losses relative to the total power output, though, these figures don't very well indicate the reduction in power loss obtained. Therefore the power loss per piston configuration of both solutions are calculated for all operational conditions. The power losses are depicted in figures 5.31 and 5.32 for a hydrostatic bearing and a roller, respectively.

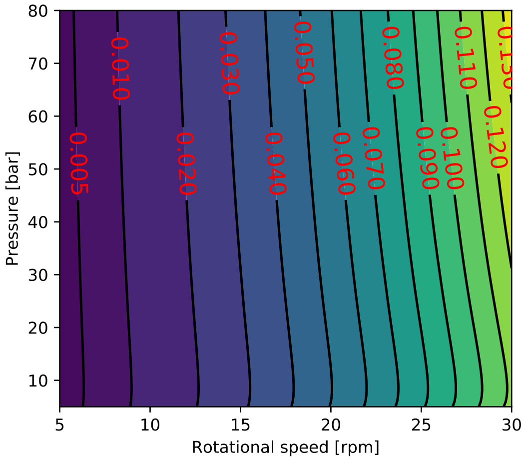

Figure 5.31: The mechanical power losses [W] due to viscous shear in one hydrostatic bearing moving over the camring for the entire operational envelope

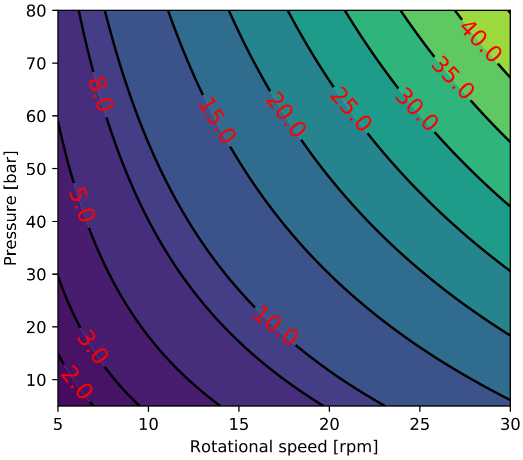

Figure 5.32: The mechanical power losses [W] due to rolling resistance in one roller moving over the camring for the entire operational envelope

The volumetric and mechanical efficiency combine to form the total efficiency. With the least square fit the closest approximation of a system with hydrostatic bearings to a system with rollers is achieved. Just as with the capillary restrictor, an exact duplication cannot be achieved because the hydrostatic bearings and rollers behave differently under different conditions. The total efficiencies of the system using hydrostatic bearings with orifice restrictors are depicted in figure 5.33 below, next to the total efficiencies of the system using rollers, figure 5.34.

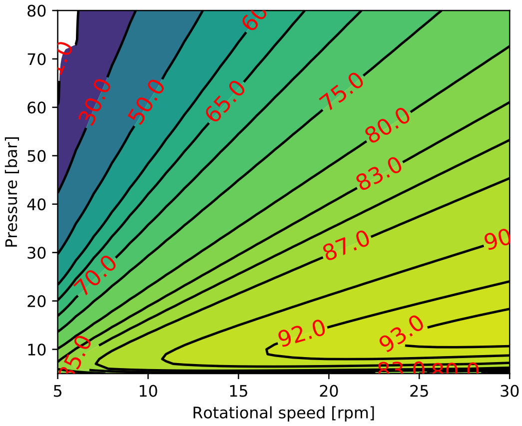

Figure 5.33: The total efficiencies of the test pump utilizing hydrostatic bearings with an orifice restrictor at all operating conditions

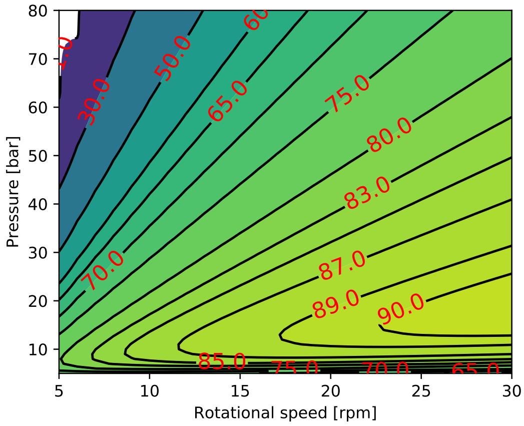

Figure 5.34: The total efficiencies of the test pump utilizing rollers at all operating conditions

The total efficiencies of the system using rollers is reproduced well by implementing a hydrostatic bearing with orifice restrictor. It could be of added value if the output control system of the pump was known. Based on these total efficiency maps, it would make sense to first build up rotational speed to its maximum at around 10 bar, before building up pressure, since this will yield the highest efficiency. In this work the path through the operating conditions taken to build up power output when higher operating conditions are reached is not taken into account. If it was, the fit performed in this chapter could be done only for the operating conditions that will actually be reached, which improves the fit since operating conditions which never occur would be neglected.

The diameter of both the capillary restrictor and the orifice restrictor which are obtained with the least square fit are very small, as to constrain the fluid film height h which limits the bearing feed flow Q^{hb}. Restrictor diameters below 0.4 to 0.5 mm, however, are at risk of blockage [13]. This problem has not been taken into account while designing the hydrostatic bearings discussed in this chapter, as the focus was to find the maximum fluid film height for which implementation of hydrostatic bearings would improve the total efficiency.

Chapter 6

Conclusion and Recommendations

6.1 Conclusion

The purpose of this thesis was to define the components critical to pump performance and to investigate the possibility to create a model predicting pump performance by using analytical equations of each defined component. This model was then tested to test data of an experimental camring driven radial piston pump. Then the potential of such a model was evaluated, with the implementation of hydrostatic bearings instead of rollers as proof of the benefits applying this model in pump design has.

To this end research questions were presented in the introduction, which are repeated below together with the taken approach and findings obtained through this work.

- What are the components critical to performance within hydraulic pumps?

The components and factors found to be critical to the performance of this type of pump are discussed as is the method used for calculating their effect. These include bearings, rollers, seals, springs, valves and leakage flow which is dependent on gap size, piston movement and viscosity and thus on hydraulic fluid. Furthermore the alignment of the piston inside the cylinder is taken into account which effects leakage, fluid shear and friction of the piston cylinder interface.

- To what accuracy can a component-wise, analytical model for pump performance be created?

The interactions of these components and factors are merged to form the proposed component-wise model for the experimental camring driven radial piston pump. The basic working of this type of pump is explained briefly and the interactions in the model are discussed aided by a flowchart. The model is also altered to allow parameter fitting to the test data to investigate the accuracy of the model with optimal parameters. Furthermore a state of the art empiric modelling method is introduced to compare the model results to.

The model is consequently compared to the obtained test data for validation. The model predicts leakage flow to an average difference of 2.7%, but outliers up to 48.7% for high pressures and -35.1% for low pressures are observed. With the parameter fit performed for piston diameter d^p the model predicts the leakage to an average difference of -13.6%. The empiric model predicts the average leakage flow to an accuracy of -47.8%.

The model predicts the input torque to an average difference of -18.6%. This difference is mainly caused by the inaccuracy of the predictions below 30 bar operating condition, where outliers up to -61.4% are observed. With the parameter fit performed for rolling resistance coefficient C_r^r an average difference of 1.0% is obtained. The empiric model predicts the average input torque to an accuracy of 0.12%.

- How sensitive to certain parameters used in the equations is the model?

Of all the reviewed components the power loss has been depicted together in one figure, figure 4.2. This gives an simple comparison of their contributions to the total power loss. The rollers and bearings present in the rollers appear to cause the highest losses in the test pump and thus are interesting for efficiency improvement. Some parameters and factors in the model are not known and are estimated based on assumptions and literature. These include the rolling resistance coefficient, bearing lubricant viscosity, temperature, alignment of the piston in the cylinder and the assumption of laminar flow. The sensitivity of the model to those are discussed.

- What are the possibilities of implementing this model into pump design?

Finally the model is used to assess the effect of implementing a hydrostatic bearing in the experimental camring driven radial piston pump. Rollers have been found in chapter 4 to cause the largest power losses in the pump operational envelope and thus it is interesting to look at alternatives for possibly efficiency improvement. The design of the hydrostatic bearing is discussed and implemented in the model.

By using a least square fit the restrictor design parameters of the system using hydrostatic bearings are found so that the total efficienies on the entire operational envelope approximate that of the system using rollers. It is found that a hydrostatic bearing using an orifice restrictor should be used because of the high Reynolds number flows obtained in the restrictor at the pump operating conditions, i.e. $Re > 1000$.

To approximate the same total efficiency for each condition the average bearing flow is found to be 0.0016 L/s, which corresponds to an average fluid film height of 12.18 μm. The orifice restrictor diameter which allows this flow is found to equal 0.239 mm. There is a risk of blockage with restrictor diameters smaller than 0.4-0.5 mm, possibly complicating the implementation of hydrostatic bearings in this pump design.

6.2 Recommendations

Based on this work some recommendations are made for future work. These concern both recommendations about the theory leading to the model and the results obtained from the model.

For the Identification of Performance Critical Components and Factors in Piston Pumps, the following is recommended:

- For this work simple, off the shelf analytical equations have been used to determine losses for each component. In depth analysis of each component can be performed to obtain better representations.

- Flow resistance through the manifolds of pumps should be taken into account and should be added to the model.

- Thermal expansion and water absorption of the materials of which the pistons and cylinders are made should be taken into account, since this effects the size of the gap between piston and cylinder and thus leakage flow.

- Rolling resistance should be evaluated more in depth as the coefficient used in this work is based on the assumption that it behaves as a steel train wheel on rails. A general method of predicting rolling resistance coefficients would benefit the generality of the model.
- Bearing lubricant viscosity and amount of lubrication present should be further incorporated into the model, as now a constant value for lubricant viscosity is used, regardless of the operating conditions.

For the Analytical Component-Wise Modelling of a Camring Driven Radial Piston Pump the following is recommended:

- Effects of dynamic input into the pump could be investigated, as the model now only predicts performance at steady state conditions.
- The prediction of mechanical efficiency at lower pressures should be investigated as here large errors are observed. Whether this error lies in the data or in the model is unknown.
- The model should be validated further for different pumps with different operational envelopes.

For the Sensitivity of Losses to Assumptions the following is recommended:

- The effect of misalignment should be validated and altered accordingly.
- Ideal pump parameters could be investigated. Which parameters lead to the most efficient design.

For the Effect of Replacing Rollers with Hydrostatic Bearings on Pump Performance the following is recommended:

- The effect of different bearing shapes should be investigated.
- As the bearing moves over the camring the contact area may vary. This spherical contact area should be investigated.
- The parameter fit performed to design the hydrostatic bearing should be done for the actual operating conditions which the pump will be subject to, to increase the quality of the fit.
- The values found for restrictor diameter d are below 0.4 mm and thus are at risk of blockage. A solution to this should be found in order to be able to implement hydrostatic bearings efficiently in this pump.

Appendix A

Checkvalve Flow Resistance Test

A.1 Checkvalve test setup

To find the pressure drop over the check valves which are used in the pump, a test set up is built. The check valve is depicted in figure A.1, the test casing is shown in figure A.2.

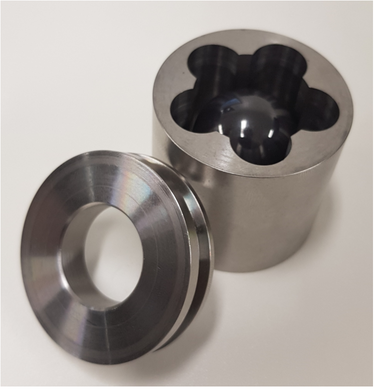

Figure A.1: Check valve

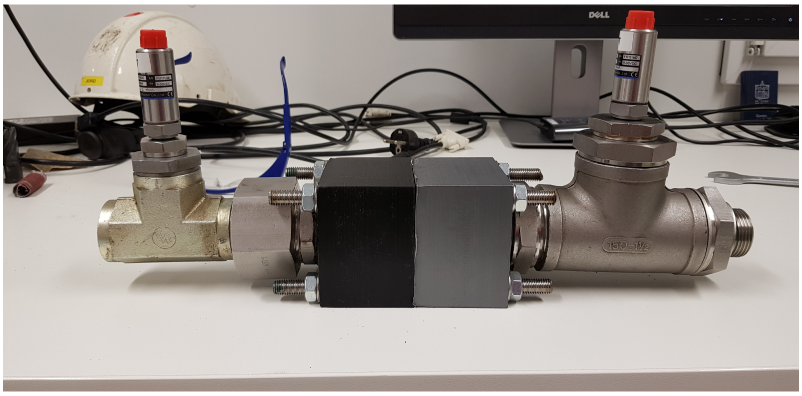

Figure A.2: Check valve test casing

The check valve is inserted in a flow circuit as depicted in figure A.3. Water is extracted from a tank by a boost pump, after which the flow is measured by flow senseor FS 01. Then the water is filtered before it reaches the first pressure sensor, PS 01. Flow goes through the check valve to the second pressure sensor, PS 02. Figure A.2 shows the checkvalve together with the two pressure sensors. To make sure pressure is built up near the checkvalve, a spear valve is added before the water goes to a drain.

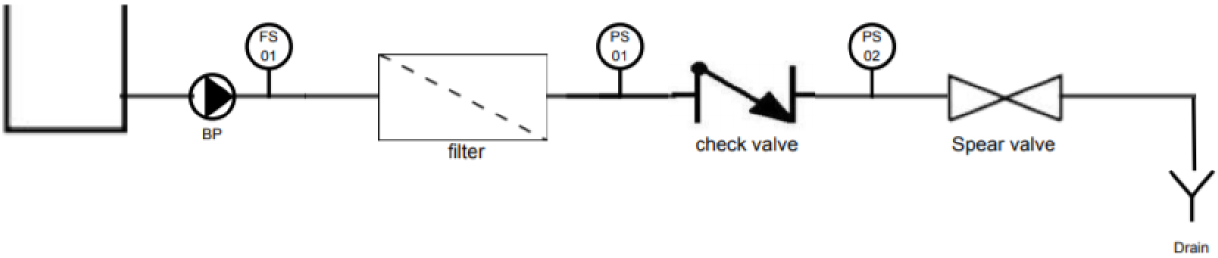

Figure A.3: Caption

The pressure drop over the check valve is measured for multiple flows to find the valve flow coefficient K_v. The data processing is discussed below.

A.1.1 Checkvalve data processing and results

To get an accurate approximation of the pressure drop with (2.25), the data should be analyzed before it is used. Figure A.4 shows the raw flow data, figure A.5 shows the raw in and output pressures measured at the checkvalve and figure A.6 contains the raw pressure drop data versus the corresponding measured flow.

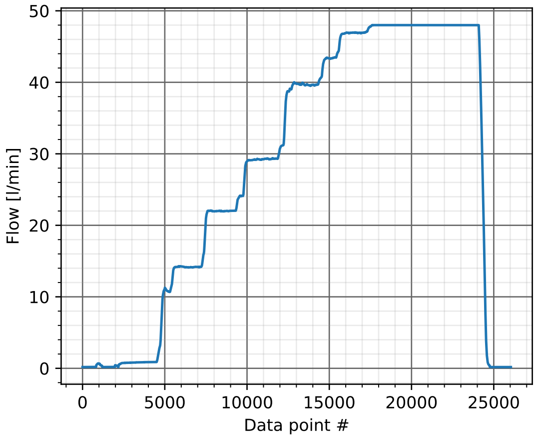

Figure A.4: Unfiltered flow data

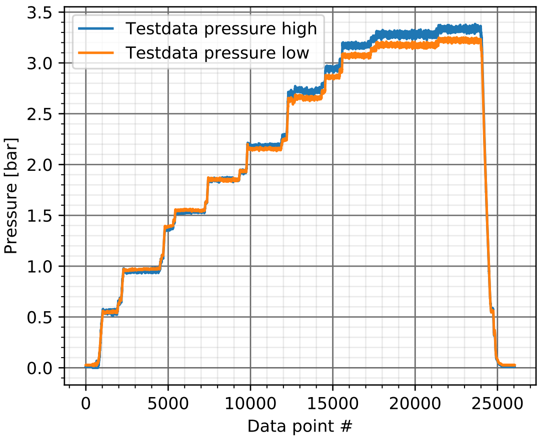

Figure A.5: Unfiltered in and output pressure

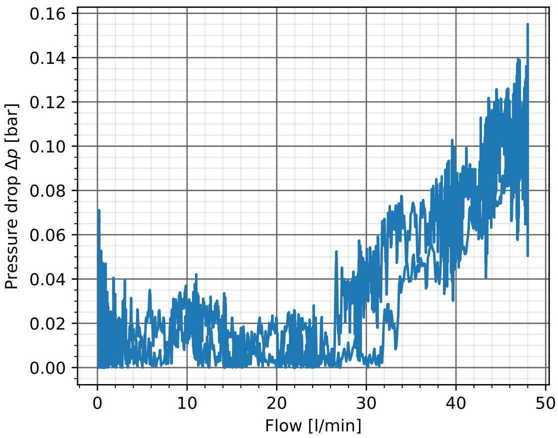

Figure A.6: Unfiltered pressure drop data versus the flow

The measurements began before flow was initiated, so this initial data points should be deleted, along with the corresponding pressure data points. Also, the flow meter used in the test set-up had a maximum measurement flow of 48 [l/min]. Thus all measurements of the flow at 48 [l/min], and the corresponding pressure data points, are deleted as well. Following the transient data is removed, i.e. the data between two points where measurements are performed for a longer time at steady conditions. The data that is left is depicted in figures A.7, A.8 and A.9 for the flow, in and output pressures and pressure drops versus flow, respectively.

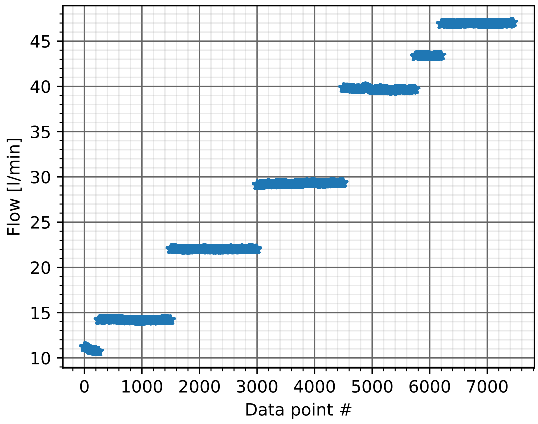

Figure A.7: Flow data with transient data filtered out

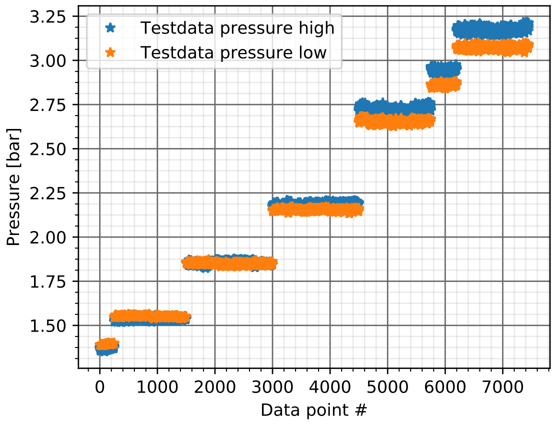

Figure A.8: in and output pressure data with transient data filtered out

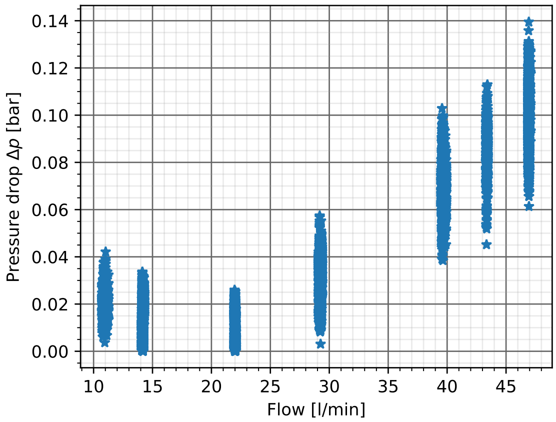

Figure A.9: Pressure drop data with transient data filtered out

The measurements depicted in figures A.7, A.8 and A.9 show measurements at steady conditions for a longer period of time. For each of those conditions, all of the measurements are averaged. In total measurements have been done at 7 different conditions, so 7 datapoints remain. The acquired datapoints for flow are depicted in figure A.10, the in and output pressures are shown in figure A.11 and the pressure drops in figure A.12. Using this data with (2.25) gives 7 different values for the valve coefficient K_v. These are depicted in figure A.13. The average value found is $K_v = 146.68$.

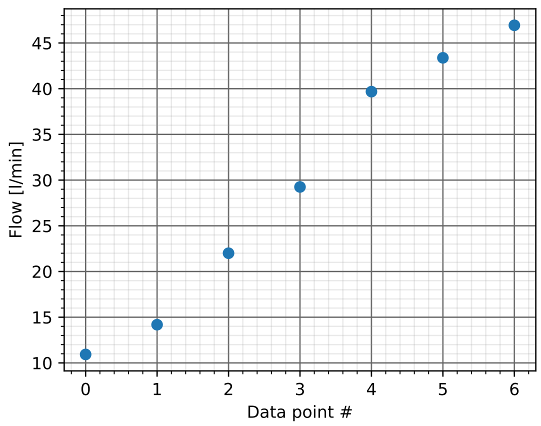

Figure A.10: Average values for flow at the test datapoints

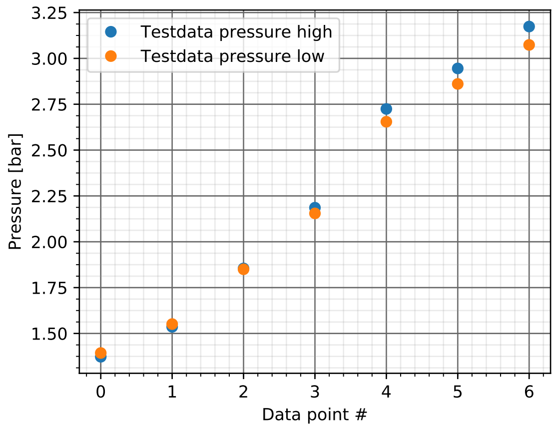

Figure A.11: Average values for in and output pressure at the test datapoints

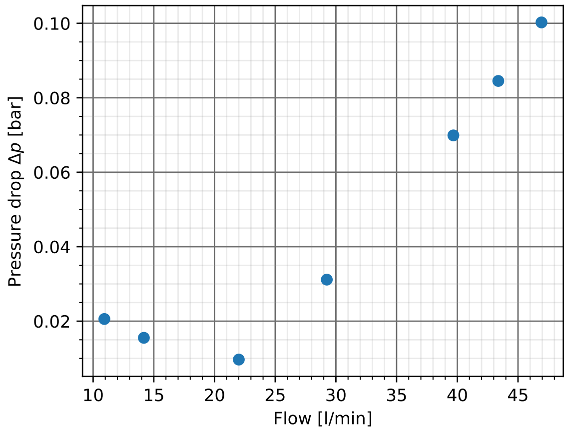

Figure A.12: Average values for pressure drop at the test datapoints

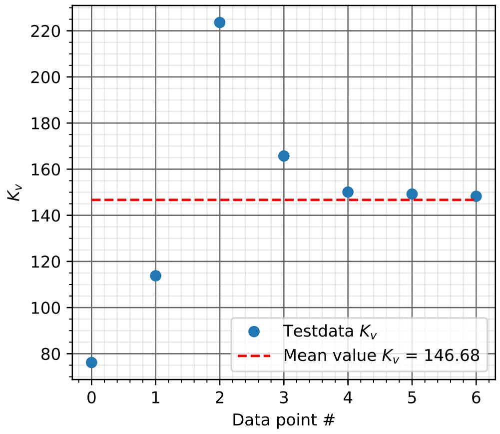

Figure A.13: Values for valve coefficient K_v determined at datapoints

The average value found for K_v is used to calculate the pressure drops as quadratic function of flow velocity. To check whether the outcome makes sense, a quadratic fit is performed on the pressure drop data points as following

$$\Delta p = a\,(Q^{cv})^2 \tag{A.1}$$

with a as fitting parameter and Q^{cv} [l/min] as volume flow. The results are depicted in figure A.14 below.

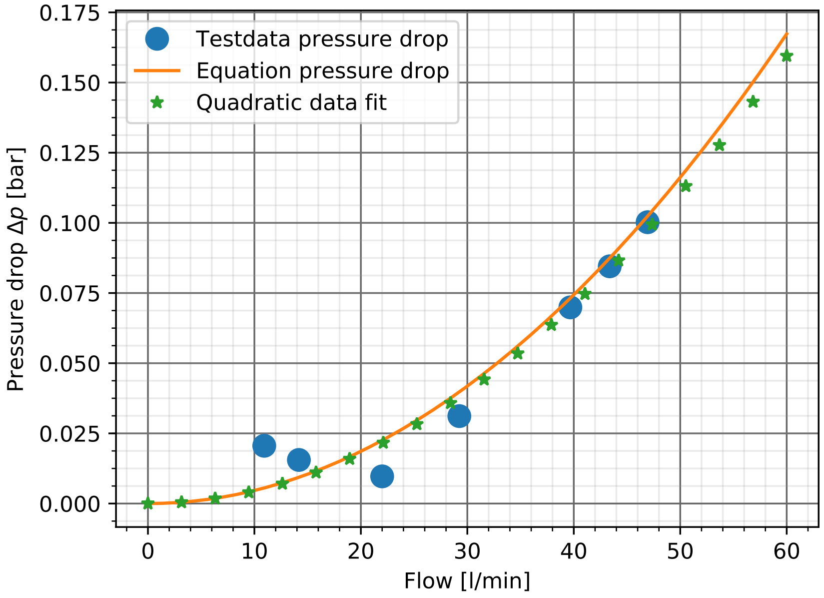

Figure A.14: Approaching the pressure drops with the found value for K_v and a quadratic fit as check

Appendix B

Testing of the DOT Pump

B.1 Test setup

The test bench of the DOT pump can be seen in figure B.1. Figure B.2 shows the computer image of the test bench as designed. Left of the DOT pump a Hägglunds motor is attached to the test bench to drive the pump. Furthermore a boost pump is included to feed water to the system. To obtain data of testing multiple sensors are incorporated in the system. Figure B.3 shows the piping and instrument diagram (P&ID) of the test bench.

Figure B.1: The DOT pump attached to its test bench

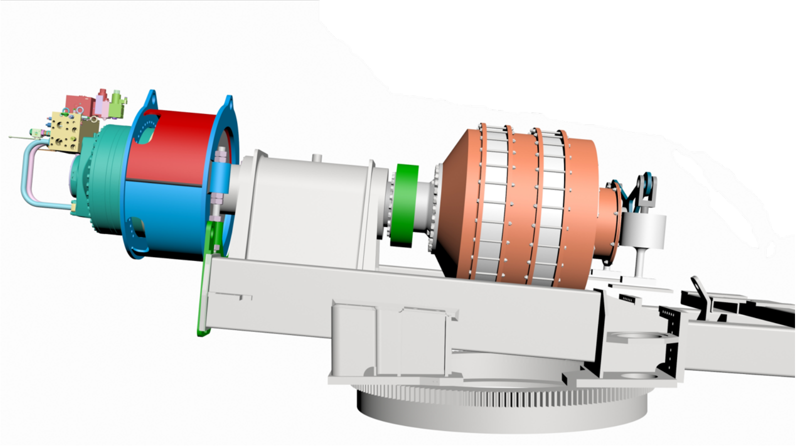

Figure B.2: A computer image of the DOT pump attached to its test bench

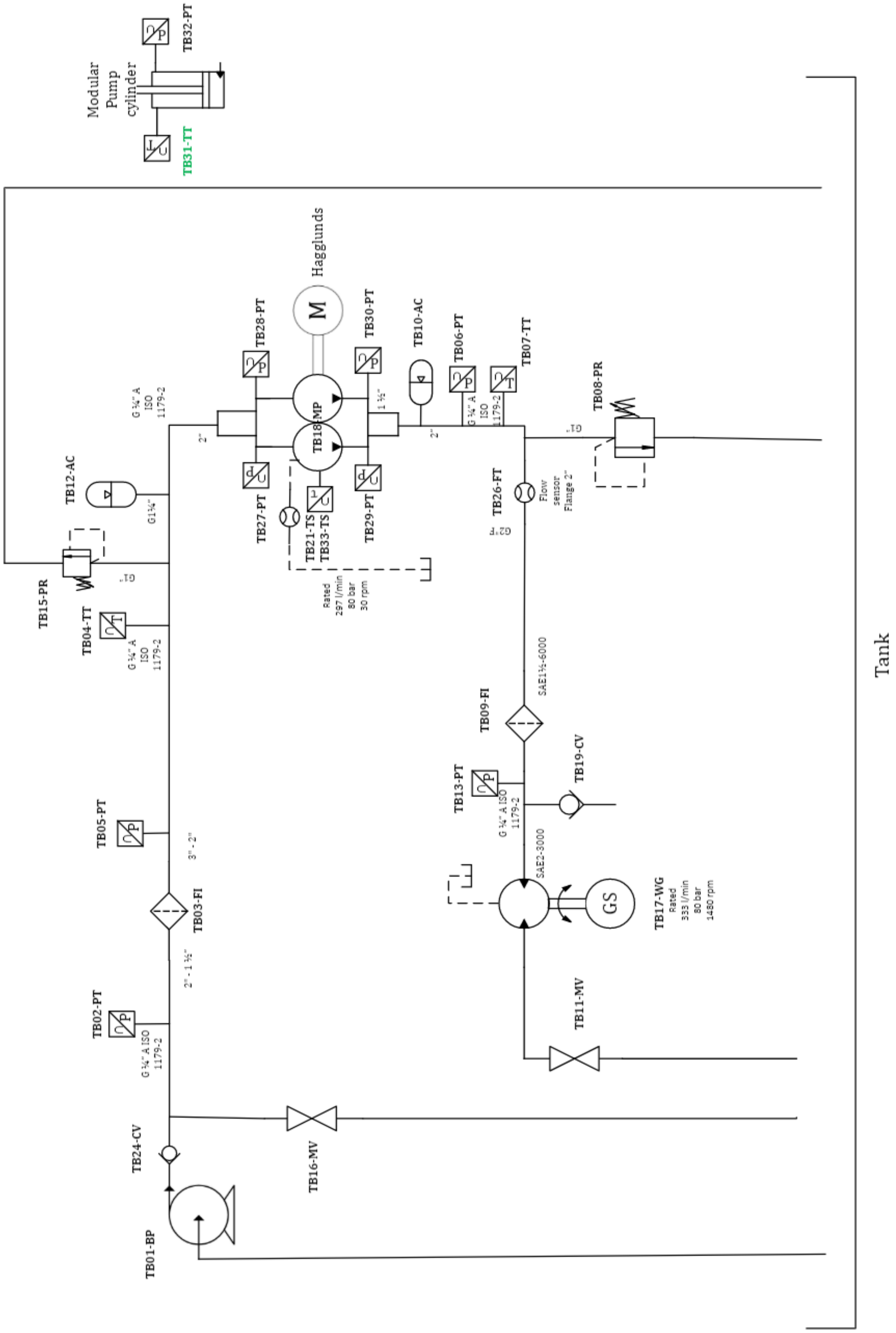

Figure B.3: Piping and instrument diagram of the DOT pump test setup

B.2 Data processing

To determine the performance of the pump measurements are performed at different operating conditions for around 5 minutes per operational condition. This data contains transient data, i.e. data of the changing of conditions. Only steady state conditions are wanted to create the datapoints necessary to determine pump performance. Thus the data has to be filtered so that the transient data is removed and only data of conditions that are steady for a couple of minutes remains. Of this remaining data the averages can be taken to, for example, at a certain rotational speed and output pressure, get the average discharge flow Q_d at this condition.

For each steady rotational speed and output pressure the boost pressure p_{boost}, discharge flow Q_d, input torque T_{in} and temperature T are sought in order to be able to execute the performance calculations. All of the rotational speed data is shown in figure B.4, all of the output pressure data is given in figure B.5.

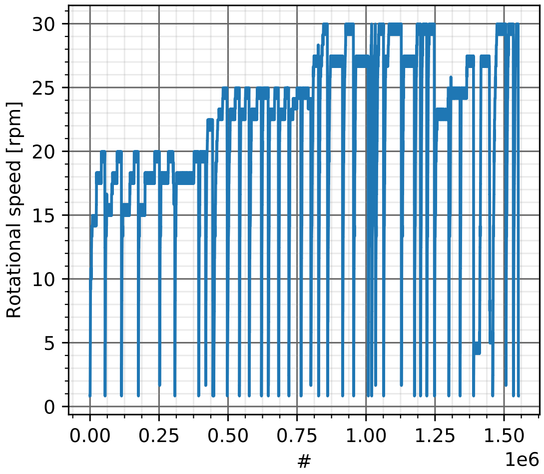

Figure B.4: The unfiltered rotational speed test data of the DOT pump

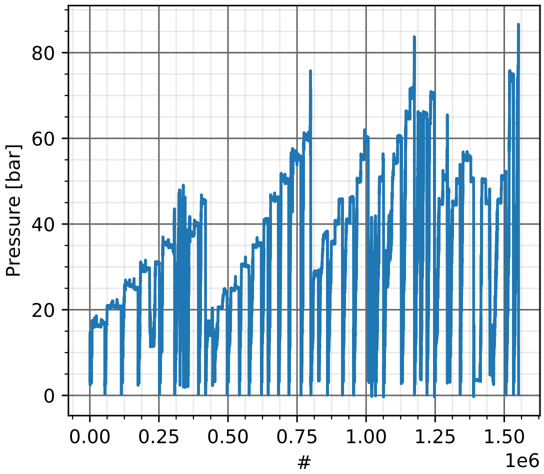

Figure B.5: The unfiltered output pressure test data of the DOT pump

The first filter performed on all the parameters mentioned above is by deleting all data that does not belong to a steady rotational speed. For this, all of the rotational speed data is analyzed in steps of 2 minutes. If the average value of 2 minutes rotational speed data equals to the average of the next 2 minutes of rotational speed data, all of the data in these 4 minutes is saved. If the average value of the next 2 minutes is equal again, this is saved as well. If not, the new average is compared to the next two minutes, to see if a new steady condition is reached. The residual data for rotational speed is depicted in figure B.6. The residual output pressure data is shown in figure B.7.

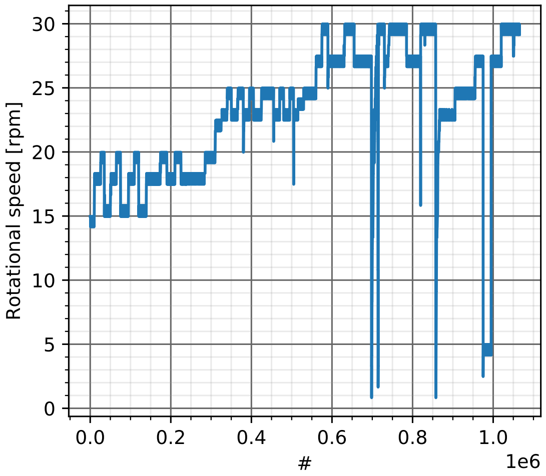

Figure B.6: The rotational speed test data of the DOT pump filtered to bins of 4 minutes constant speed

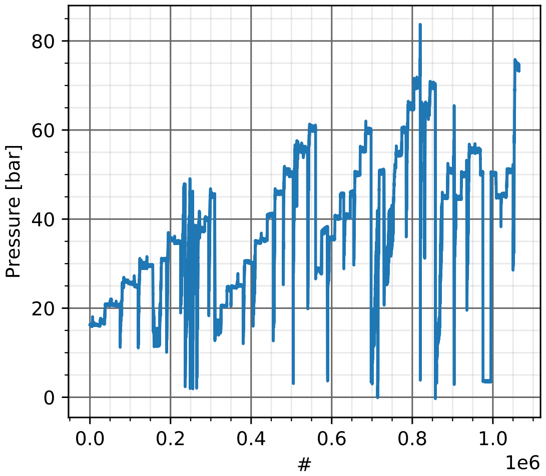

Figure B.7: The output pressure test data of the DOT pump filtered to bins of 4 minutes constant speed

Next the same is done for the residual output pressure. The data is analyzed for 4 minutes of steady output pressure. All of the other data is deleted. The left over rotational speed data is visualized in figure B.8 and the residual output pressure data in figure B.9.

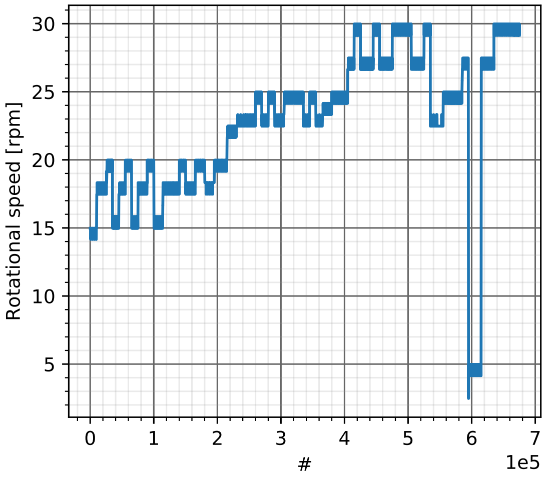

Figure B.8: The rotational speed test data of the DOT pump filtered to bins of 4 minutes constant speed and 2 minutes constant output pressure

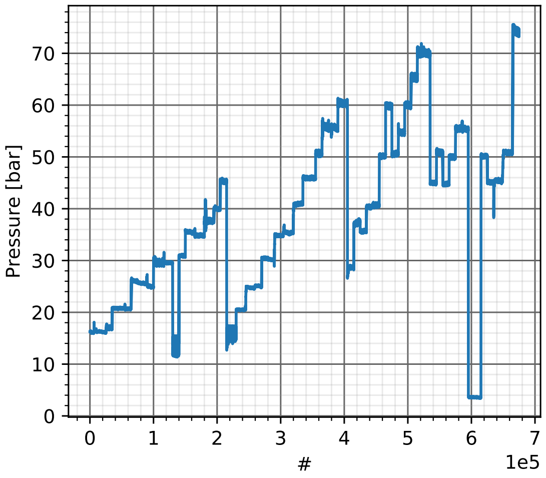

Figure B.9: The output pressure test data of the DOT pump filtered to bins of 4 minutes constant speed and 2 minutes constant output pressure

It can be seen that the rotational speed data, for a steady rotational speed, actually indicates two different rotational speeds. This is more clearly indicated in figure B.10.

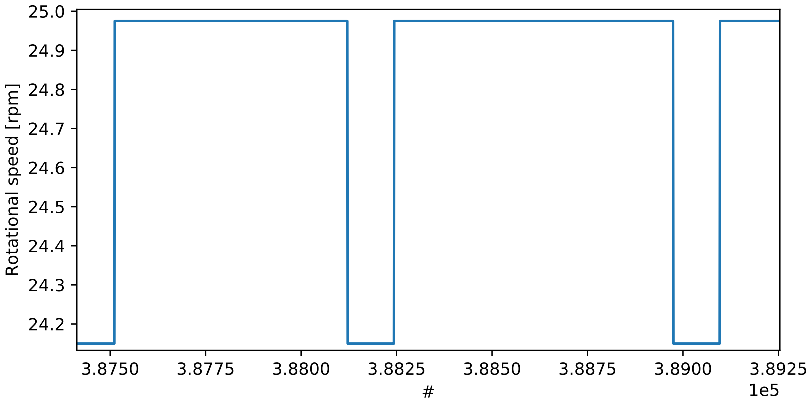

Figure B.10: More detailed measurement performed by the rotational speed sensor

This is because of the way the sensor operates. It is depicted schematically in figure B.11. The sensor has a sampling time dt. It measures how many points crossed the sensor in time dt. A scenario is depicted in figure B.11. It is assumed that in one sampling time dt, one full rotation plus a bit occurs. Thus if the left side of the image is the starting point, the sensors location after dt would be that of the scenario depicted with number 1. It would have measured all 8 points on the circle. After another timestep dt, the sensor would be located at the scenario depicted with number 2. It would thus have measured 9 points in this sampling time dt. This is why the rotational speed data measures one rotational speed as 2 rotational speeds alternating each other. It is assumed that taking the average of these two rotational speeds gives a good estimation of the real rotational speed.

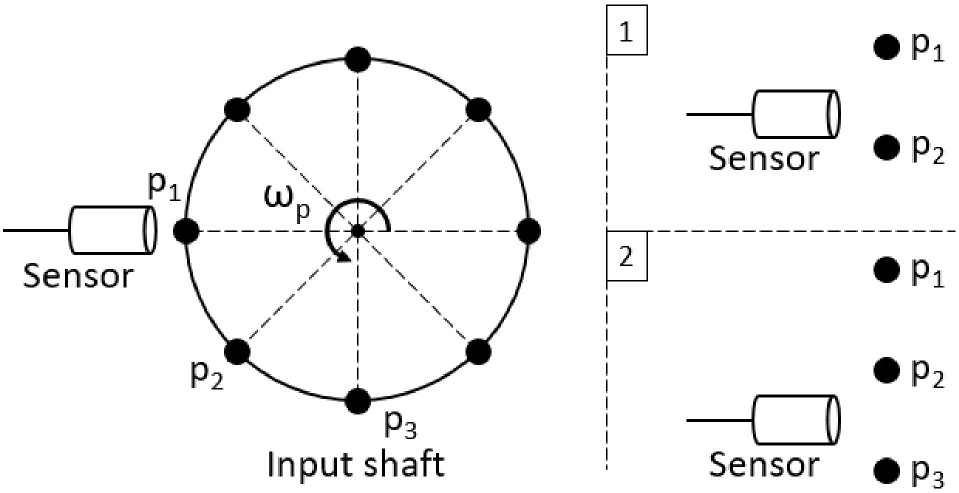

Figure B.11: The working of the rotational speed sensor depicted schematically

The average rotational speed of each measured operational condition which is left after filtering is depicted in figure B.12. The residual average output pressure data is shown in figure B.13.

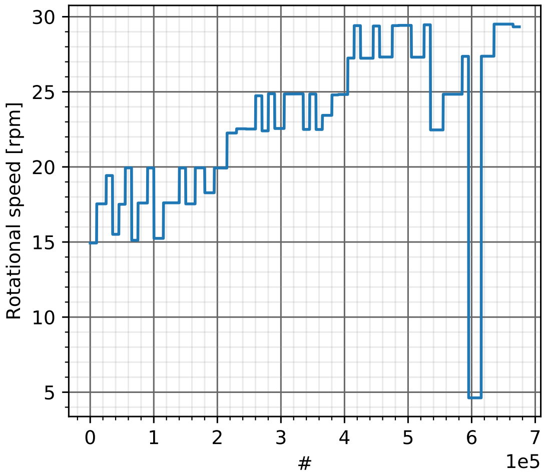

Figure B.12: The rotational speed test data of the DOT pump filtered to bins of 4 minutes constant speed and 4 minutes constant output pressure, averaged

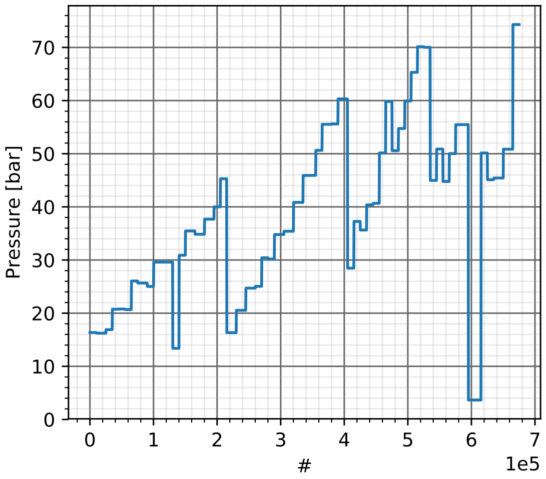

Figure B.13: The output pressure test data of the DOT pump filtered to bins of 4 minutes constant speed and 4 minutes constant output pressure, averaged

The average rotational speed and output pressure for each measured operational condition are then saved as a datapoint. The rotational speed datapoints are given in figure B.14, the output pressure datapoints in figure B.15.

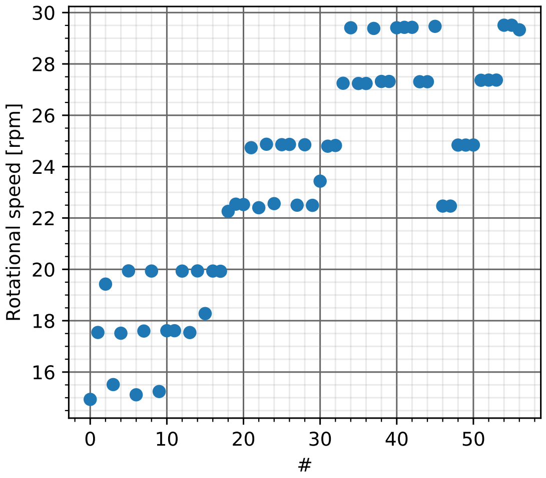

Figure B.14: The rotational speed datapoints obtained by filtering the data to constant rotational speed and output pressure

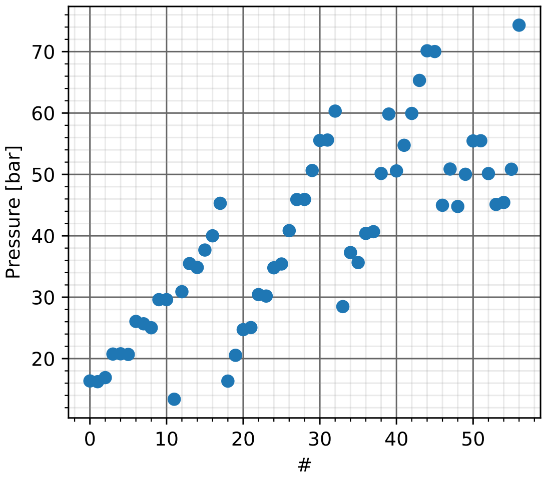

Figure B.15: The output pressure datapoints obtained by filtering the data to constant rotational speed and output pressure

Also the measured discharge flow Q_d and input torque T_{in} corresponding to the filtered rotational speed and output pressure data are averaged into datapoints. The datapoints of the discharge flow are depicted in figure B.16, the datapoints of the input torque in figure B.17.

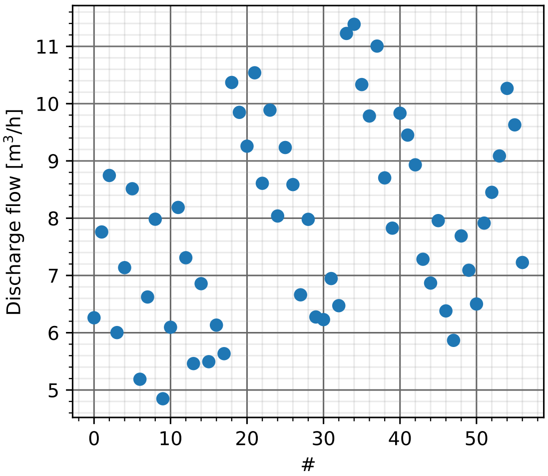

Figure B.16: The discharge flow Q_d datapoints obtained by filtering the data to constant rotational speed and output pressure

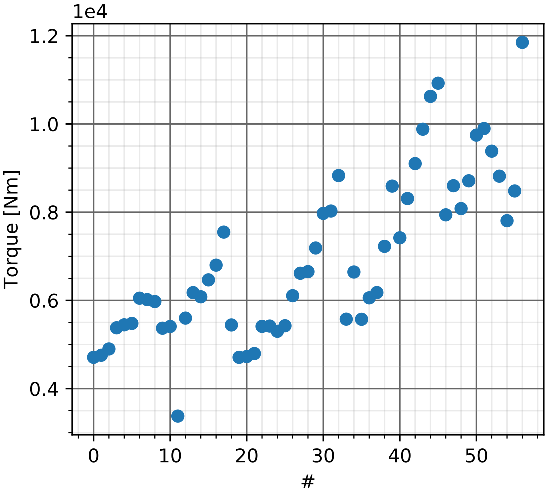

Figure B.17: The input torque T_{in} datapoints obtained by filtering the data to constant rotational speed and output pressure

Appendix C

Model of the Pump Performance

C.1 Piston displacement, speed and camring-roller contact angle

To describe the movement of the pistons two methods have been investigated. The first is a mathematical approach, using sinusoidal functions to describe the movement. Another method is the use of a least square fit to get a description of the movement. Data from the Inventor software is available describing the displacement and velocity of a piston at a pump operating speed of 30 rpm. Figure C.1 shows the approximation of the piston displacement, figure C.2 the approximation of the piston velocity.

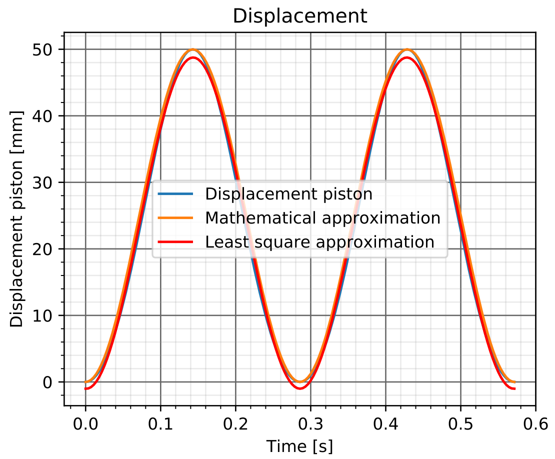

Figure C.1: The displacement of a piston at 30 rpm pump rotation speed estimated analytically and numerically

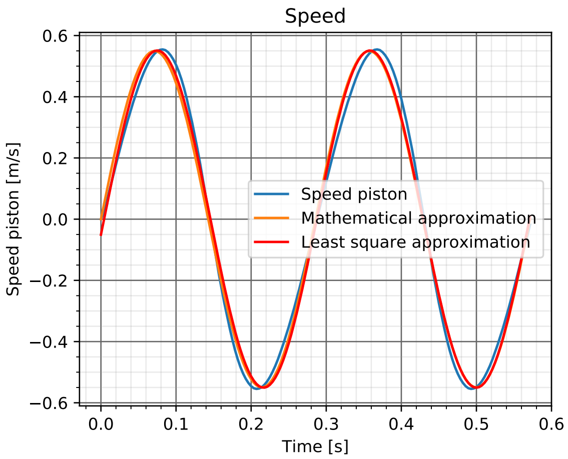

Figure C.2: The velocity of a piston at 30 rpm pump rotation speed estimated analytically and numerically

As seen both methods give a good approximation of the actual displacement and velocity. It is chosen to use the mathematical approximation because this gives an equation which can easily be altered to fit different operating conditions or even different camrings.

Thus to describe the movement of the pistons sinusoidal functions have been composed. These are dependent on the strike length, the rotational speed of the pump and the amount of oscillations a piston makes per pump rotation. For the vertical displacement of the piston equation C.1 is found as following

$$y^p(t) = A \cdot \sin(\omega^{cr} t + n\pi) + b \tag{C.1}$$

with A [m] as the amplitude, ω^{cr} [rad/s] is the angular frequency of the pump, t [s] is the time, $n\pi$ is the phase shift and b is the initial value of the function. Amplitude A is found as the stroke length divided by 2, $A = \frac{l_{strike}}{2}$, initial value b equals amplitude A and the phase shift equals $n\pi = -0.5\pi$. The angular frequency ω^{cr} of the function can be determined with the input rpm of the pump together with the amount of piston oscillations per pump rotation. With those values known the period T_p [s] of the piston can be calculated as in equation C.2.

$$T_p = \frac{60}{n_{cr}} \cdot n_w \tag{C.2}$$

From the period the angular frequency is determined as in equation C.3 below.

$$\omega^p = \frac{2\pi}{T_p} \tag{C.3}$$

With the function for displacement $y^p(t)$ known, the function for piston velocity U^p can be determined by taking the time derivative of the displacement, $\frac{dy^p}{dt}$. Equation C.4 is found.

$$U^p = A \cdot \omega \cdot \cos(\omega t + n\pi) \tag{C.4}$$

Since the test pump uses a camring to translate the rotation of the shaft to the translation in the pistons, the angle between the camring and piston is of importance for force calculations. It is found that the angle follows the same sinusoidal shape as the piston velocity, but with a different amplitude. The amplitude will be the maximum angle the piston makes with the camring, α_{max}. Equation C.5 is found.

$$\alpha = \alpha_{max} \cdot \cos(\omega^{cr} t + n\pi) \tag{C.5}$$

To show the output these equations give for the piston movement, the movement is plotted for maximum rpm of the test pump, for one piston strike. The necessary input values are shown in table C.1. The resulting figures are visualized in figure C.3. Only one piston strike is used to perform all calculations to increase the efficiency of the model.

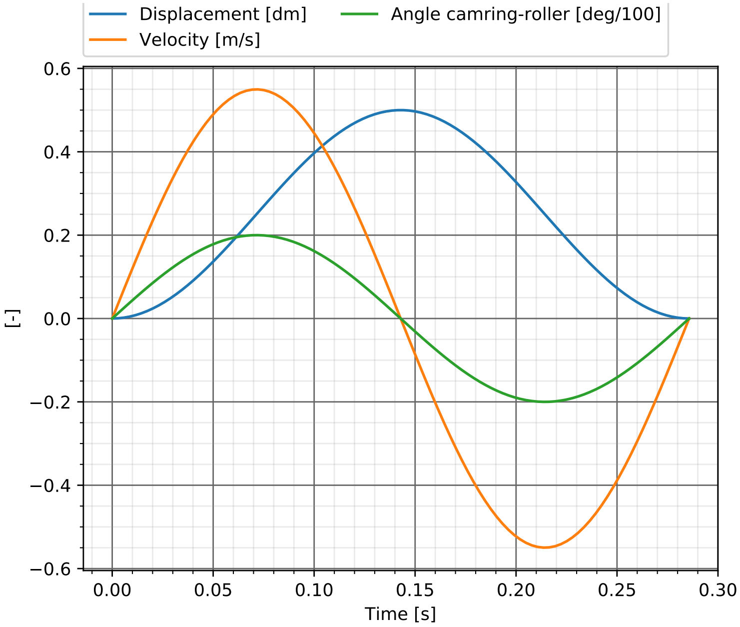

Figure C.3: Te movement of the piston over the camring, including its position, velocity and angle with the camring

$l_{strike}\,[m]$	$n_{cr}\,[rpm]$	n_w	$\alpha_{max}\,[^o]$
0.5	30	7	20

Table C.1: Values for the piston movement to create figure C.3

This movement of the piston is a major input into the model. The location of the piston and its velocity are translated to many other parts where they cause a certain displacement at a certain velocity or rotations.

C.2 Leakage

Leakage flow is determined with the chamber pressure p_c and the location and velocity of the piston inside the cylinder. Figure C.4 shows the distance of the head of the piston to the leakage line during one piston strike. Figure C.5 shows the pressure gradient over the piston during one piston strike. All figures in this section are made at an operating condition of 80 bar and 30 rpm.

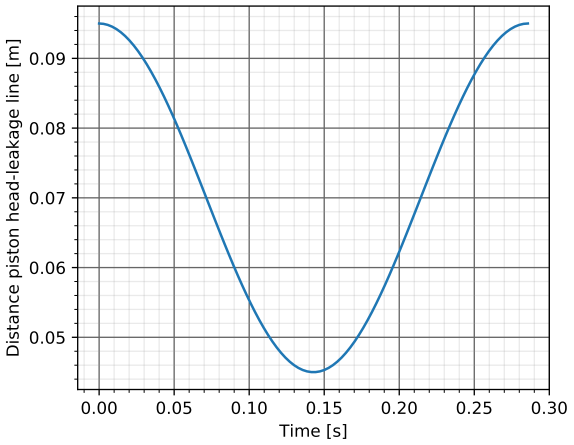

Figure C.4: Distance piston head leakage line during one piston strike

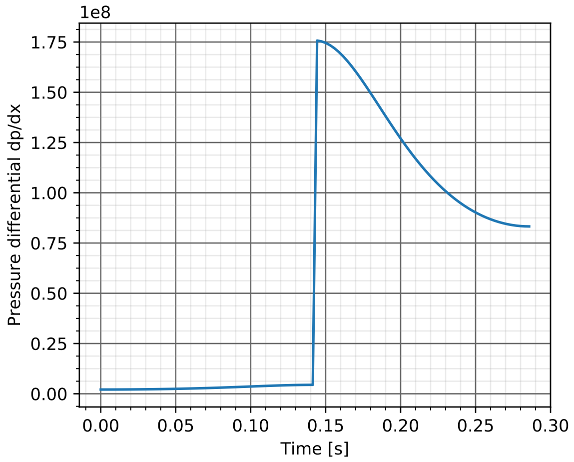

Figure C.5: Pressure gradient $\frac{dp}{dx}$ over the piston during one piston strike

The leakage during one piston strike corresponding to the pressure gradient and piston velocity found for this operating condition is presented in figure C.6. The possibility of misalignment is also taken into account into the model. The leakage that would occur according to the model during the misaligned scenario is depicted in figure C.7 below.

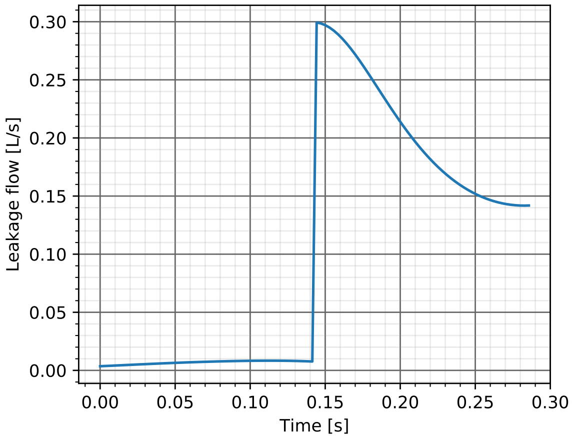

Figure C.6: Leakage during 1 piston strike during normal alignment

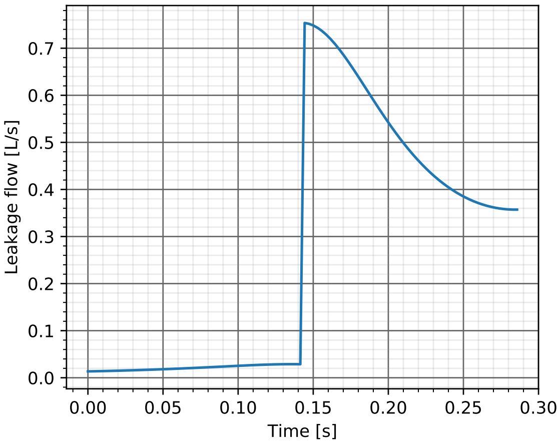

Figure C.7: Leakage during 1 piston strike in the misaligned scenario

C.3 Temperature of Hydraulic Fluid

Both pressure and temperature are found to effect the viscosity of a fluid. The method for determining the viscosity as function of pressure and temperature is discussed in chapter 2. It is found that temperature has the biggest influence on the viscosity. Also, the temperature of the input hydraulic fluid is most likely to alter of these two, as it is dependent on outside conditions. Therefore the influence of temperature on leakage flow per piston at 80 bar and 30 rpm is investigated further. Figure C.8 shows the leakage per piston versus the hydraulic fluid temperature. It is seen that the leakage differs significantly over the presented temperature range. Do note that thermal expansion of the piston and cylinder is not taken into account here. Due to thermal expansion the gap between piston and cylinder could decrease, possibly countering this extra leakage that occurs at higher temperatures.

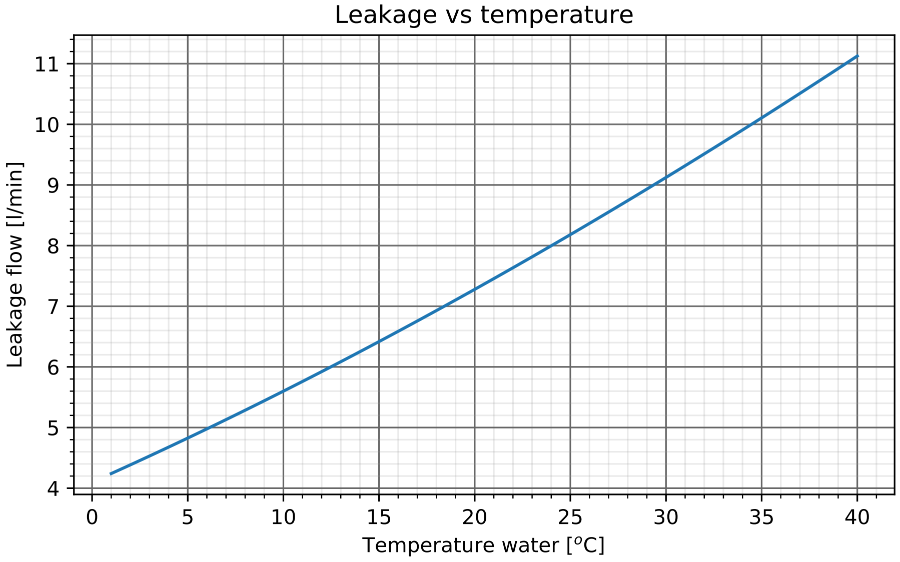

Figure C.8: The leakage of a piston-cylinder interface [L/min] of average gap size correlated to the water temperature

C.4 Shear force

Figures 4.40 and 4.41 in the leakage section show the piston velocity profile and pressure gradient profile of the test pump for the operating conditions of 80 bar and 30 rpm.

As discussed there three points of interest are investigated to check the flow profile in the leakage flow film, which can be seen in figure 4.43. The flow profile should be known for every moment during a piston strike to determine how the shear stress alters at the piston wall.

Next the values of $\frac{dv_x}{dy}$ at the surface of the piston are found with equation 2.29. The flow velocity $v_x(y)$ equals the piston velocity at $y = 0$, and $\frac{dv_x}{dy}$ is found by calculating equation 2.29 just above $y = 0$. Figure C.9 visualizes the found values of the flow gradient during one piston strike at 80 bar and 30 rpm.

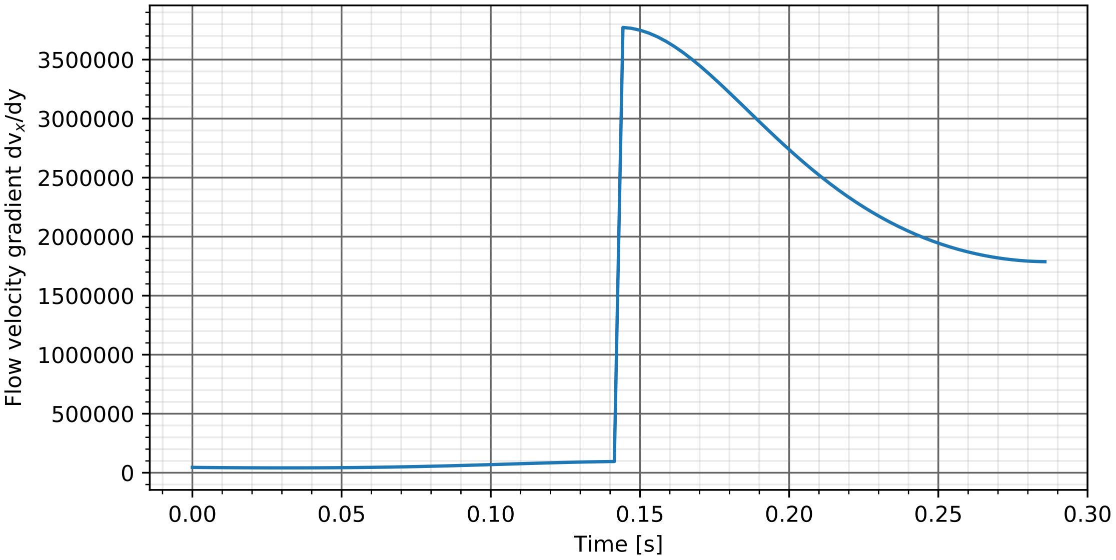

Figure C.9: The leakage flow velocity gradient $\frac{dv_x}{dy}$ just above the piston surface over one piston strike at 80 bar and 30 rpm

Finally the values for the viscous shear τ on the piston surface are found using equation 2.32. The force induced by this shear stress is found using equation 2.33 and are depicted in figure C.10 below.

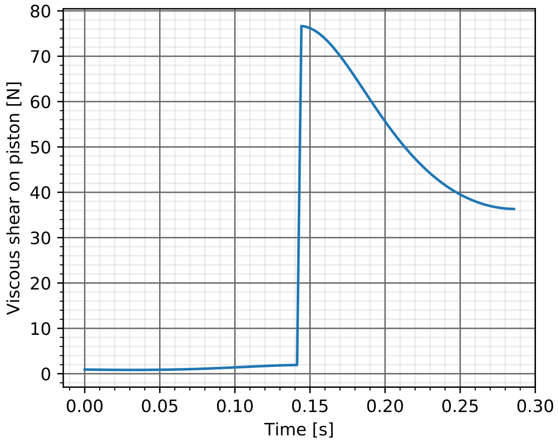

Figure C.10: The viscous shear τ [Pa] induced on the piston during one piston strike at 80 bar and 30 rpm

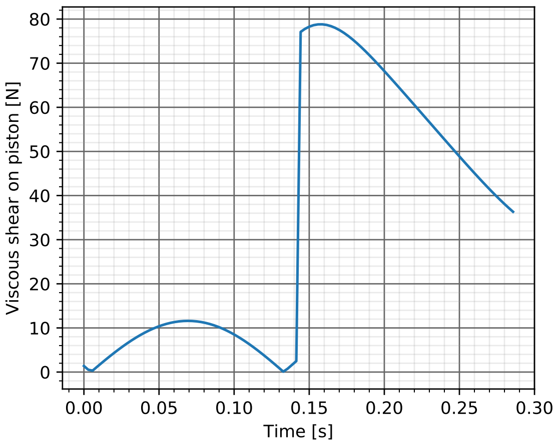

Figure C.11: The viscous shear τ [Pa] induced on the piston during one piston strike at 80 bar and 30 rpm during misalignment

C.5 Piston force

The force induced on the components is determined by the output pressure of the pump and the dimensions of the pistons. Based on the output pressure of the pump, p_d, the chamber pressure inside the cylinders p_c is backtracked through iterations. After an estimate of the output flow Q_d of the pump is made, the pressure drop Δp due to flow in the pump is calculated. This pressure drop is added to the output pressure as the new chamber pressure p_c. This new chamber pressure is then used to calculate the new leakage flow and thus the output flow Q_d, after which a new pressure drop Δp can be found. This iteration is repeated until the change in chamber pressure is insignificant. Based on this chamber pressure and the diameter of the piston, the total force induced by pressure per piston can be determined as in equation C.6.

$$F_{pc} = p_c \cdot A^p = p_c \frac{\pi d^p}{4} \tag{C.6}$$

The spring force resisting piston motion is dependent on the piston location and the initial compression and is determined as in C.7. The resulting spring force during one piston strike at 80 bar and 30 rpm is presented in figure C.12.

$$F_s = k_s u = k_s(l_{strike} - y + u_0) \tag{C.7}$$

In addition to the chamber pressure force and spring force, the viscous shear force F_v and seal friction force F_{sl} resist piston motion. The total force resisting piston motion is therefore found with C.8.

$$F_p = F_{pc} + F_s + F_v + F_{sl} \tag{C.8}$$

The total force resisting piston motion during one piston strike at 80 bar and 30 rpm is depicted in figure C.13.

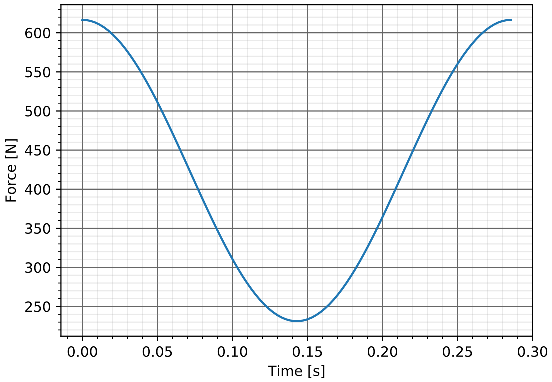

Figure C.12: Force induced on piston by piston spring during one piston strike

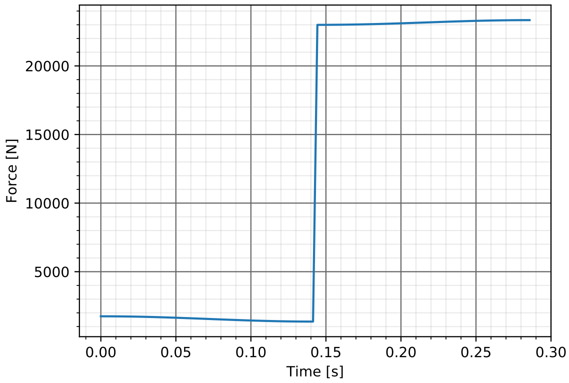

Figure C.13: Total force experienced per piston during one piston strike

C.6 Roller movement, forces and power losses

Two components in the test pump which are directly linked to the piston movement is the camroller and SFM roller. The camrollers roll over the camring in order to translate the rotation of the camring to the translation of the piston with minimal losses. Losses in the roller related to its velocity and the force it endures are rolling resistance and losses in the bearings present in the roller. To determine the rolling speed the piston velocity U^p and the camring-roller angle α are used, which are determined with (C.4) and (C.5). Subsequently the roller velocity can be determined as in (C.9).

$$v_r^r = \frac{U^p}{\sin(\alpha)} \tag{C.9}$$

With the values given in table C.1, the roller velocity v_r^r over one piston strike is depicted in figure C.15.

The side force mitigation system consists of rollers as well, but is constricted to vertical movement. Thus these rollers follow the same movement as the piston, which is depicted in figure C.3.

The forces to which the camrollers and SFM rollers are subject to are derived from the total force necessary for piston motion, F_p, and the angle between the camring and roller. The total normal force on the rollers F_n^r is determined with (C.10), the side force which is mitigated by the side force mitigation rollers is calculated with (C.11).

$$F_n^r = \frac{F_p}{\cos(\alpha)} \tag{C.10}$$

$$F_{\text{side}} = F_p \tan(\alpha) \tag{C.11}$$

The found values for the forces are depicted in figure C.14 below. The power losses which lead directly from these forces and velocities are depicted in figure C.16.

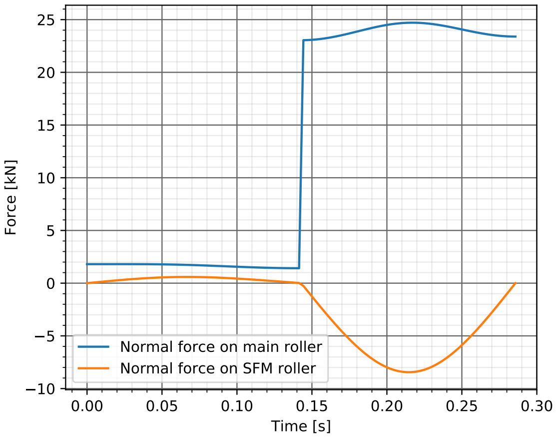

Figure C.14: The forces on a camroller and SFM roller during one piston strike at 30 rpm and 80 bar output pressure

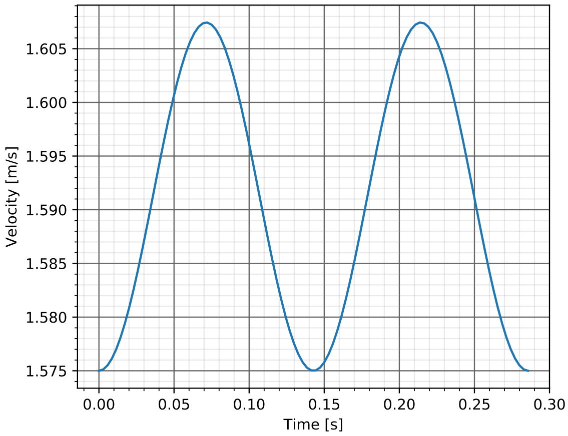

Figure C.15: The velocity of a camroller during one piston strike

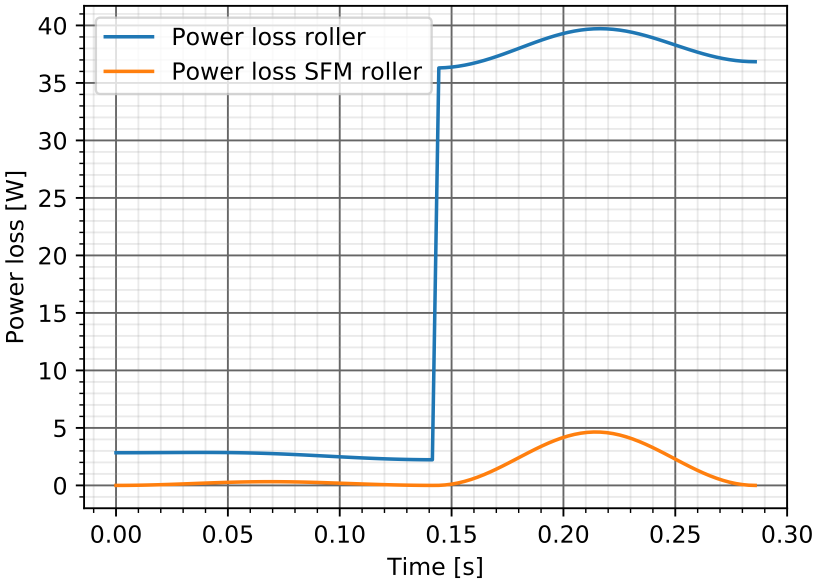

Figure C.16: The power losses due to rolling resistance of the camring roller and the SFM roller

C.7 Bearings

The power losses in the bearings in the pump are determined as described in chapter 2. The losses at 80 bar and 30 rpm in the internal pump bearings, which support the camring on the pump shaft, are presented in figure C.17. The normal force F_n^b on these bearings are assumed to be constant as they carry the weight of the camring and pump housing, thus the losses during one piston strike are constant.

The losses in the bearings present in the rollers and SFM system rollers are shown in figure C.18. Clearly the difference in power losses corresponding to low chamber pressure and high chamber pressure can be distinguished.

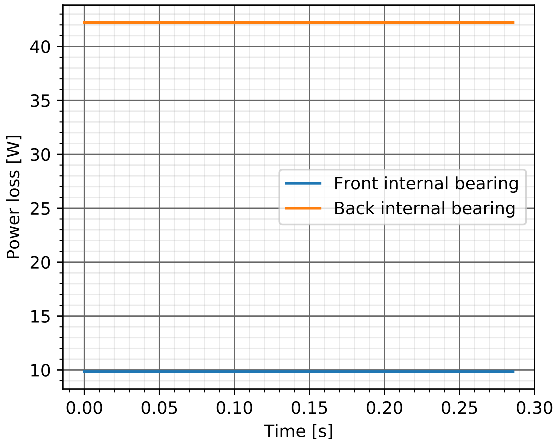

Figure C.17: The power losses during one piston strike of the front and back internal bearings

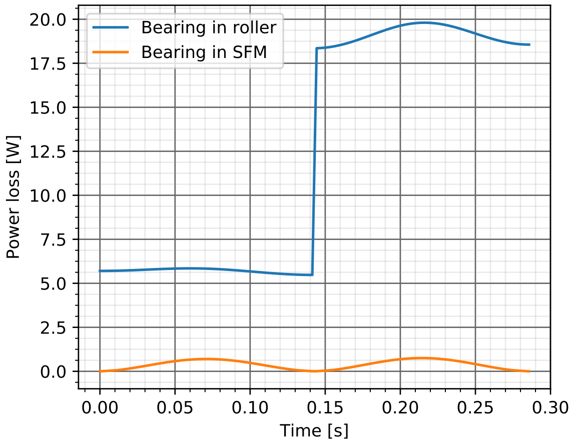

Figure C.18: The power losses during one piston strike of a bearing present in the rollers and a bearing present in the side force mitigation system

Appendix D

Graphical User Interface

In this appendix the graphical user interface (GUI) is presented which is built around the proposed model to conveniently make use of it. Such a GUI is beneficial for the ease of checking the pump performance in the design phase.

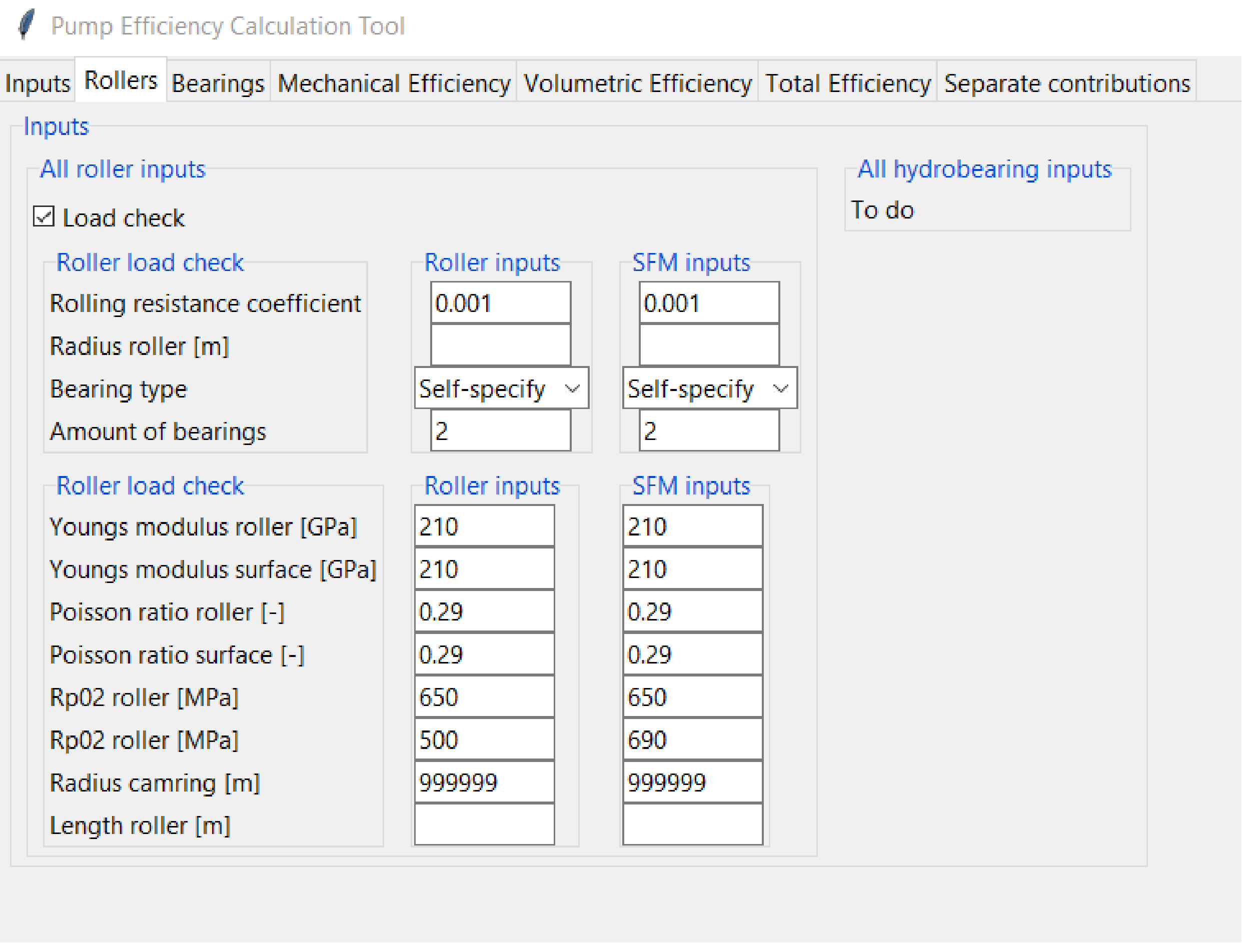

Inputs

All roller inputs

☑ Load check

Roller load check	Roller inputs	SFM inputs
Rolling resistance coefficient	0.001	0.001
Radius roller [m]		
Bearing type	Self-specify	Self-specify
Amount of bearings	2	2

Roller load check	Roller inputs	SFM inputs
Youngs modulus roller [GPa]	210	210
Youngs modulus surface [GPa]	210	210
Poisson ratio roller [-]	0.29	0.29
Poisson ratio surface [-]	0.29	0.29
Rp02 roller [MPa]	650	650
Rp02 roller [MPa]	500	690
Radius camring [m]	999999	999999
Length roller [m]		

All hydrobearing inputs

To do

Figure D.1: The camring and side force mitigation parameters which can be altered to the pump design

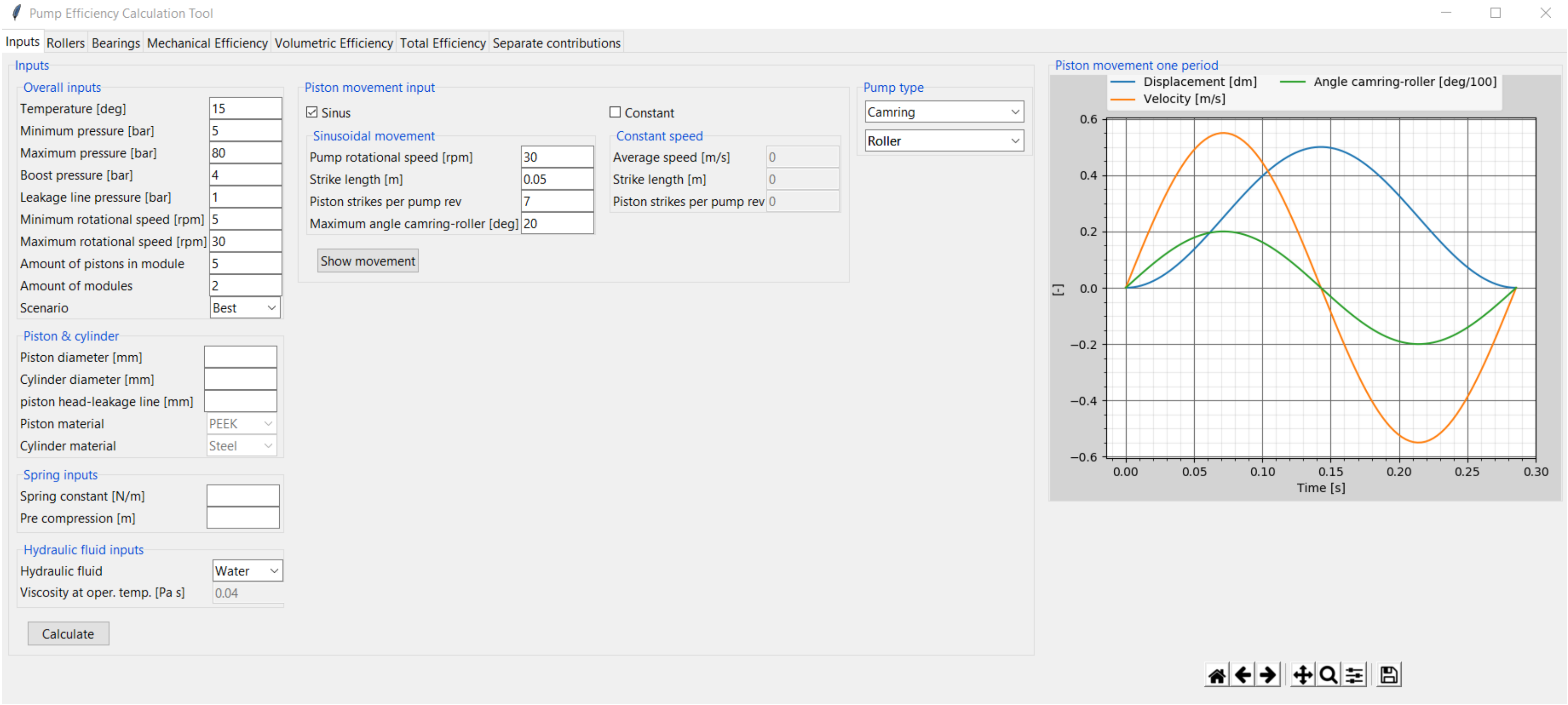

Inputs

Overall inputs

Temperature [deg]: 15
Minimum pressure [bar]: 5
Maximum pressure [bar]: 80
Boost pressure [bar]: 4
Leakage line pressure [bar]: 1
Minimum rotational speed [rpm]: 5
Maximum rotational speed [rpm]: 30
Amount of pistons in module: 5
Amount of modules: 2
Scenario: Best

Piston & cylinder

Piston diameter [mm]:
Cylinder diameter [mm]:
piston head-leakage line [mm]:
Piston material: PEEK
Cylinder material: Steel

Spring inputs

Spring constant [N/m]:
Pre compression [m]:

Hydraulic fluid inputs

Hydraulic fluid: Water
Viscosity at oper. temp. [Pa s]: 0.04

Piston movement input

☑ Sinus

Sinusoidal movement

Pump rotational speed [rpm]: 30
Strike length [m]: 0.05
Piston strikes per pump rev: 7
Maximum angle camring-roller [deg]: 20

☐ Constant

Constant speed

Average speed [m/s]: 0
Strike length [m]: 0
Piston strikes per pump rev: 0

Pump type

Camring
Roller

Figure D.2: The initial input parameters and motion which can be altered to the pump design

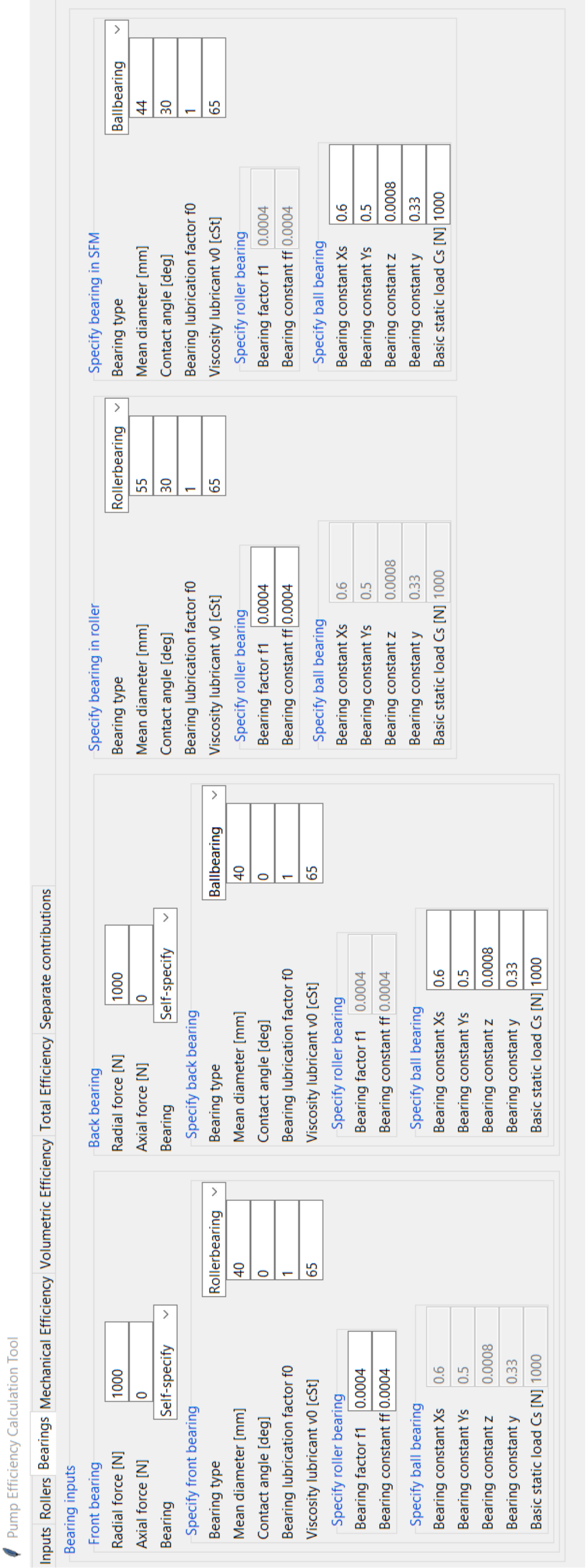

Bearing inputs

Front bearing

Radial force [N] 1000

Axial force [N] 0

Bearing Self-specify

Specify front bearing

Bearing type Rollerbearing

Mean diameter [mm] 40

Contact angle [deg] 0

Bearing lubrication factor f0 1

Viscosity lubricant v0 [cSt] 65

Specify roller bearing

Bearing factor f1 0.0004

Bearing constant ff 0.0004

Specify ball bearing

Bearing constant Xs 0.6

Bearing constant Ys 0.5

Bearing constant z 0.0008

Bearing constant y 0.33

Basic static load Cs [N] 1000

Back bearing

Radial force [N] 1000

Axial force [N] 0

Bearing Self-specify

Specify back bearing

Bearing type Ballbearing

Mean diameter [mm] 40

Contact angle [deg] 0

Bearing lubrication factor f0 1

Viscosity lubricant v0 [cSt] 65

Specify roller bearing

Bearing factor f1 0.0004

Bearing constant ff 0.0004

Specify ball bearing

Bearing constant Xs 0.6

Bearing constant Ys 0.5

Bearing constant z 0.0008

Bearing constant y 0.33

Basic static load Cs [N] 1000

Specify bearing in roller

Bearing type Rollerbearing

Mean diameter [mm] 55

Contact angle [deg] 30

Bearing lubrication factor f0 1

Viscosity lubricant v0 [cSt] 65

Specify roller bearing

Bearing factor f1 0.0004

Bearing constant ff 0.0004

Specify ball bearing

Bearing constant Xs 0.6

Bearing constant Ys 0.5

Bearing constant z 0.0008

Bearing constant y 0.33

Basic static load Cs [N] 1000

Specify bearing in SFM

Bearing type Ballbearing

Mean diameter [mm] 44

Contact angle [deg] 30

Bearing lubrication factor f0 1

Viscosity lubricant v0 [cSt] 65

Specify roller bearing

Bearing factor f1 0.0004

Bearing constant ff 0.0004

Specify ball bearing

Bearing constant Xs 0.6

Bearing constant Ys 0.5

Bearing constant z 0.0008

Bearing constant y 0.33

Basic static load Cs [N] 1000

Figure D.3: All of the bearing parameters which can be altered to the pump design, including internal bearings, bearings in the rollers and bearings in the side force mitigation system

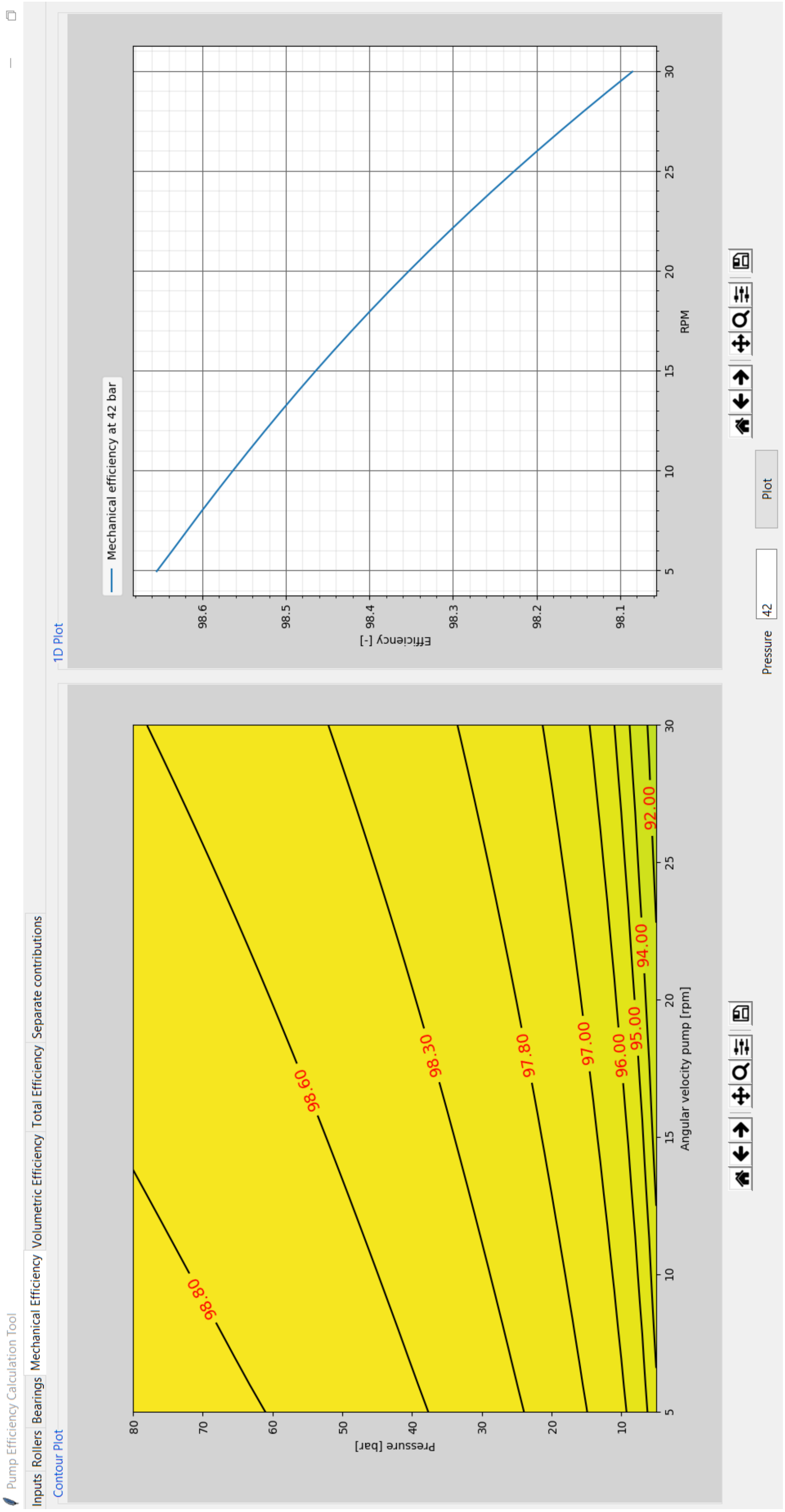

Figure D.4: The mechanical efficiencies based on the entire input operational envelop and pump parameters

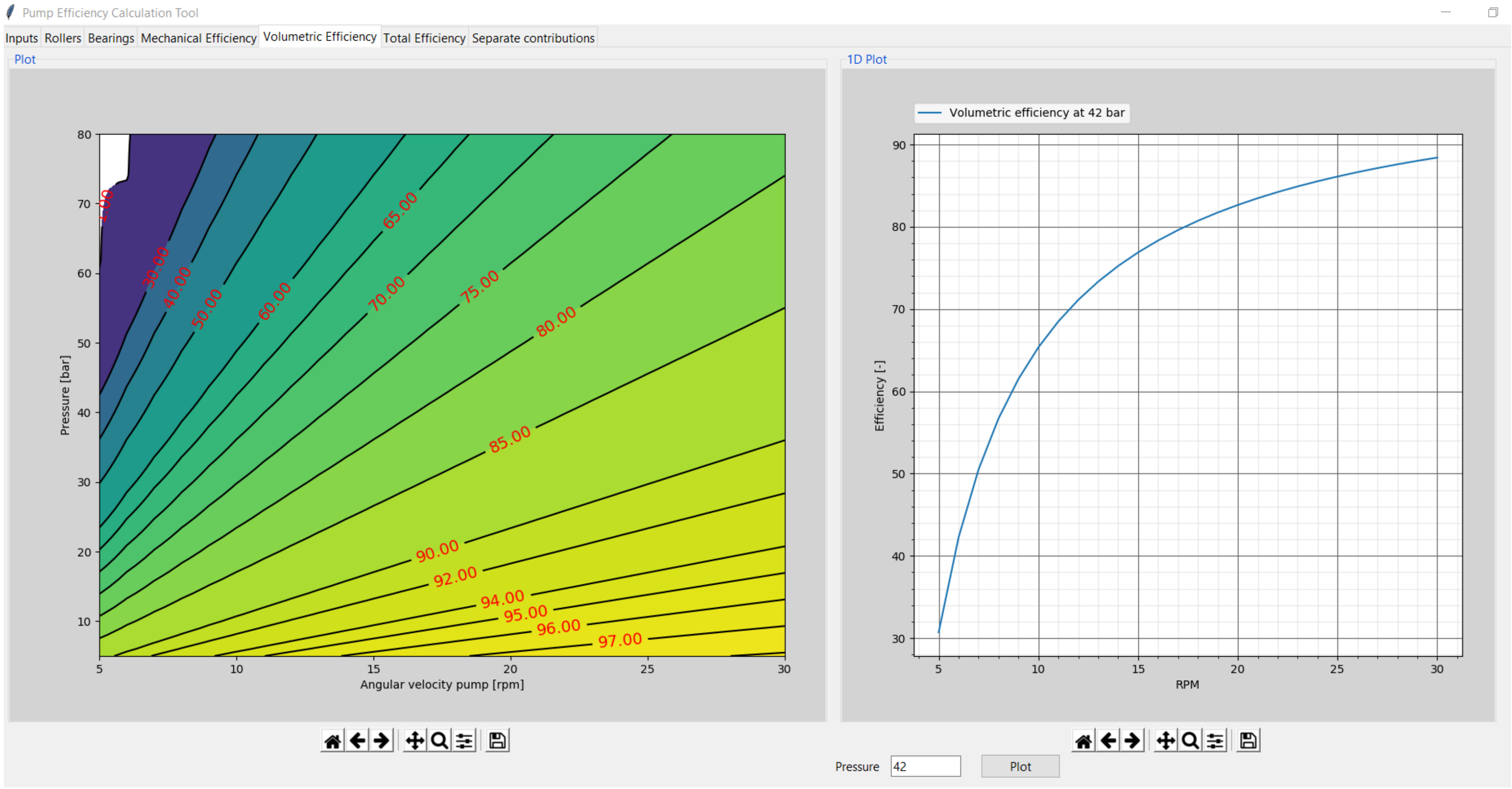

Figure D.5: The volumetric efficiencies based on the entire input operational envelop and pump parameters

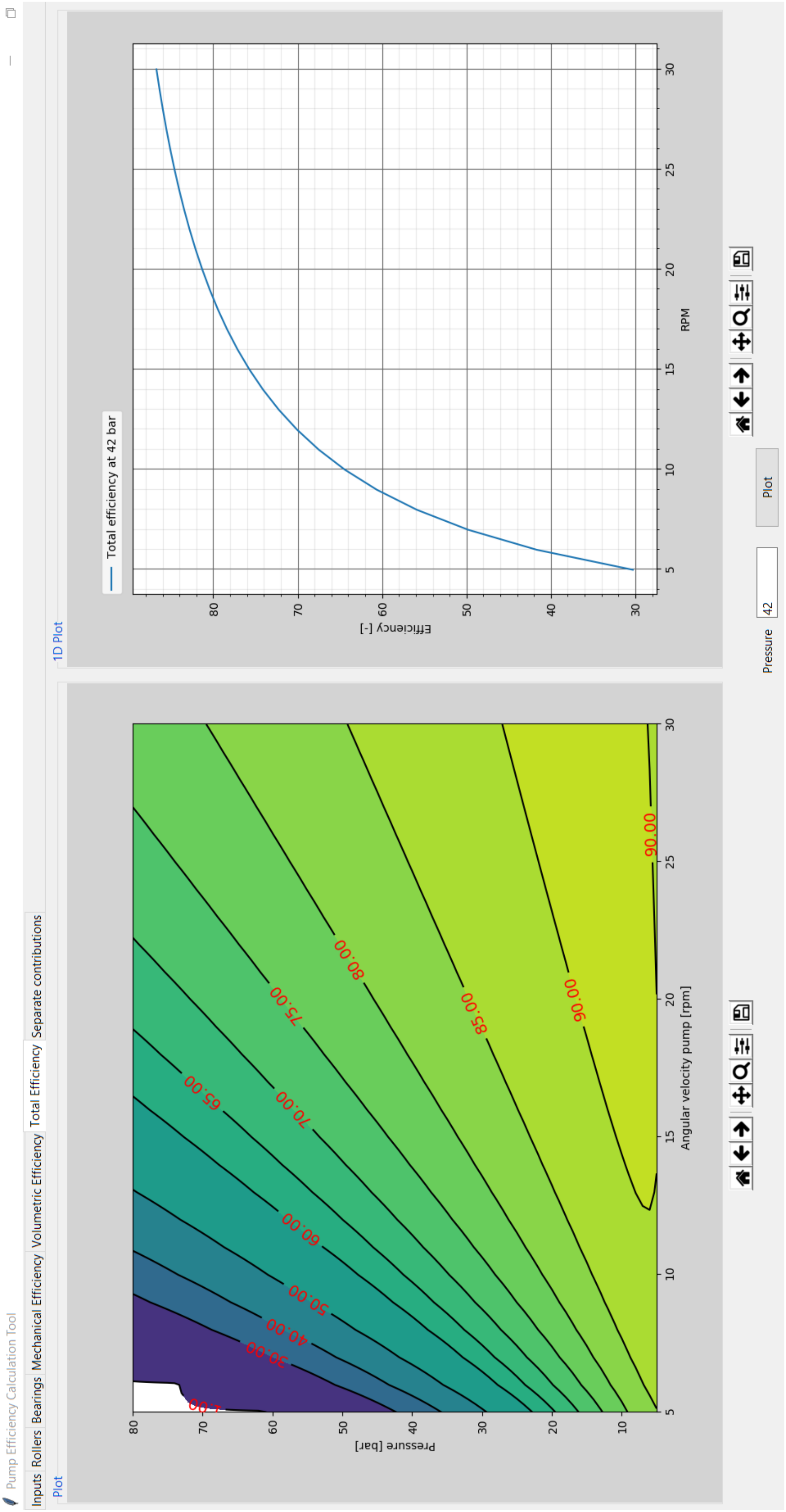

Pressure 42

Figure D.6: The total efficiencies based on the entire input operational envelop and pump parameters

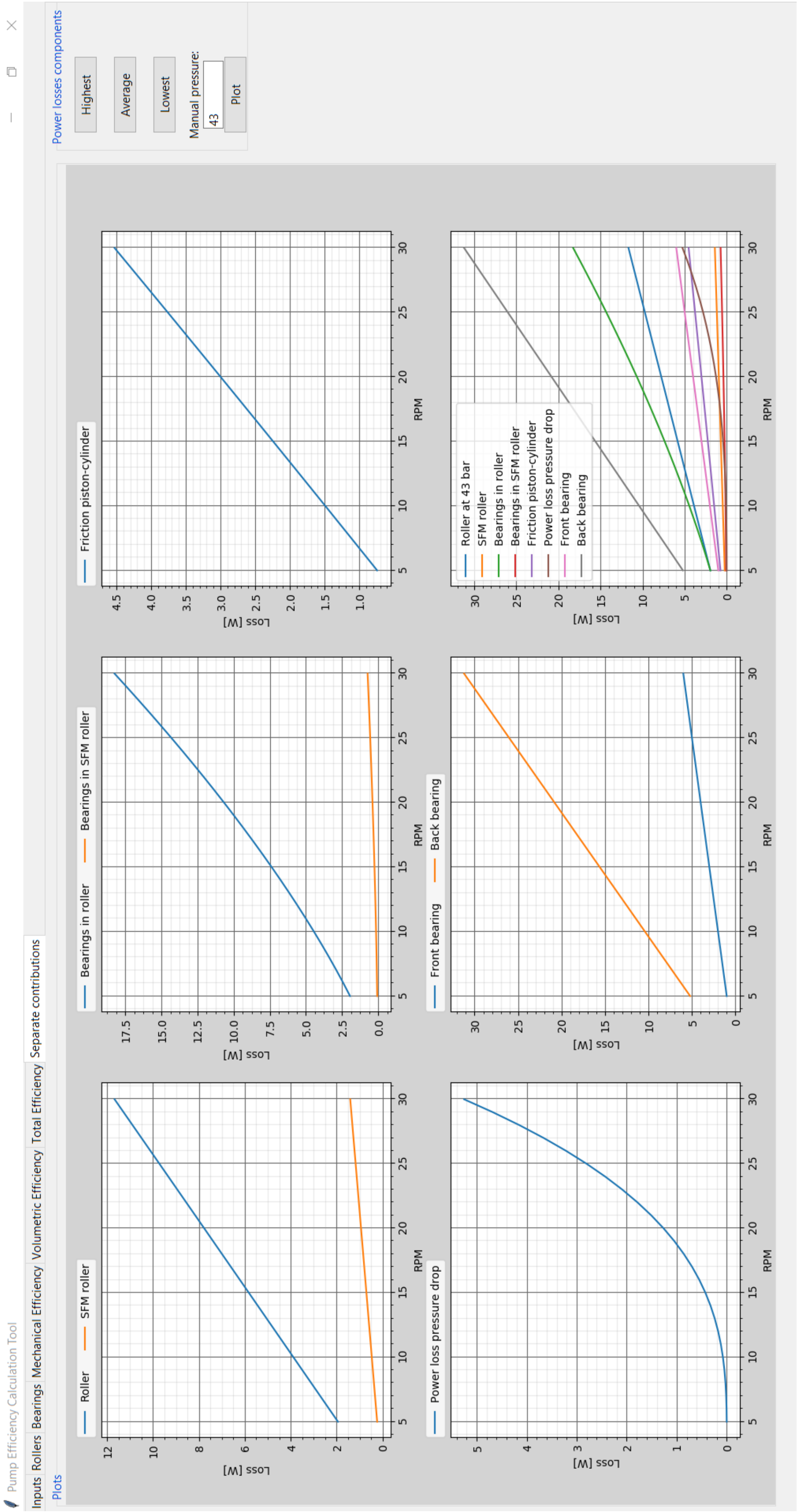

Manual pressure: 43

Figure D.7: The contributions on performance loss of each component based on the entire input operational envelop and pump parameters

Bibliography

[1] Hägglunds, "Compact CA product manual," tech. rep.

[2] Hägglunds. `https://www.boschrexroth.com/en/xc/company/haegglunds-landingpage/haegglunds-landingpage`.

[3] N. Diepeveen, "Design considerations for a wind-powered seawater pump," in *European Offshore Wind Conference Proceedings, EWEA, Marseille, France. Available at: http://www.ewea. org*, 2009.

[4] mekanizmalar, "fixed displacement piston pump." `https://www.mekanizmalar.com/fixed_displacement_piston_pump.html`.

[5] Learnchannel-TV, "Different types of hydraulic pumps and how they work." `http://learnchannel-tv.com/hydraulics/hydraulic-power-unit/hydraulic-pumps/pump-types/`.

[6] N. Gebhardt, "Hydraulikpumpen und-motoren," in *Hydraulik*, pp. 149–194, Springer, 2014.

[7] N. Manring, *Hydraulic control systems.* Wiley New York, 2005.

[8] Mikrocentrum, Werktuigbouw.nl, *Werktuigbouw.nl Formuleboekje.* 2012.

[9] T. Sandberg, C. Ramdén, and M. Gamberg, "Tire temperature measurements for validation of a new rolling resistance model," *IFAC Proceedings Volumes*, vol. 37, no. 22, pp. 589–594, 2004.

[10] Engineering ToolBox, "Rolling resistance." `https://www.engineeringtoolbox.com/rolling-friction-resistance-d_1303.html`, 2008.

[11] N. E. Dowling, *Mechanical behavior of materials: engineering methods for deformation, fracture, and fatigue.* Pearson, 2012.

[12] E. Schuchtar, "Temperature dependence of fatigue crack propagation in hot work die steels," *Theoretical and applied fracture mechanics*, vol. 9, no. 2, pp. 141–143, 1988.

[13] A. Van Beek, "Advanced engineering design," *TU Delft, Delft, The Netherlands*, 2006.

[14] L. H. K. W. Johannes Brändlein, Paul Eschmann, *Ball and Roller Bearings: Theory, Design and Application.* Wiley, 3 ed., 1999.

[15] T. A. Harris and M. N. Kotzalas, *Essential concepts of bearing technology.* CRC press, 2006.

[16] A. Palmgren, "Ball and roller bearing engineering," *Philadelphia: SKF Industries Inc., 1959*, 1959.

[17] Cameron, A Schlumberger Company, “How does it work: Pressure loss.” `https://www.products.slb.com/valves/valve-academy/how-does-it-work-pressure-loss`, 2018.

[18] J. Solorio, “How fittings, valves and strainers affect pressure drop and head loss,” 2018.

[19] Engineering ToolBox, “Water - dynamic and kinematic viscosity.” `https://www.engineeringtoolbox.com/water-dynamic-kinematic-viscosity-d_596.html`, 2004.

[20] M. G. Rabie, *Fluid power engineering/M. Galal Rabie.* New York: McGraw-Hill,, 2009.

[21] J. Bergada, S. Kumar, D. L. Davies, and J. Watton, “A complete analysis of axial piston pump leakage and output flow ripples,” *Applied Mathematical Modelling*, vol. 36, no. 4, pp. 1731–1751, 2012.

[22] Glenn Research Center NASA, “Reynolds number.” `https://www.grc.nasa.gov/www/BGH/reynolds.html`, 2014.

[23] I. Kanpur, “Fluid mechanics, parallel flow in a straight channel,” December 2009.

[24] R. Fitzpatrick, “Flow between parallel plates.” 2016.

[25] T. Stolarski, *Tribology in machine design.* Butterworth-Heinemann, 2000.

[26] University College London, “Fluid mechanics ii, viscosity and shear stresses.” `http://www.homepages.ucl.ac.uk/~uceseug/Fluids2/Notes_Viscosity.pdf`, 2010.

[27] V. L. Popov, *Coulomb’s Law of Friction*, pp. 133–154. Berlin, Heidelberg: Springer Berlin Heidelberg, 2010.

[28] P. Hannifin, “Parker o-ring handbook ord 5700,” *Parker Hannifin Corporation, Cleveland, OH*, 2007.

[29] N. K. Agarwal and C. P. Lawson, “A practical method to account for seal friction in aircraft hydraulic actuator preliminary design,” *Proceedings of the Institution of Mechanical Engineers, Part G: Journal of Aerospace Engineering*, vol. 231, no. 5, pp. 941–950, 2017.

[30] H. E. Merritt, “Hydraulic control systems, 1967,” *John Weily & Sons.*

[31] U. Samland and B. Hollingworth, “The use of new materials in water hydraulics,” in *Proceedings of 4th Scandinavian International Conference of Fluid Power, Finland, Tampere University of Technology Print, Tampere*, pp. 955–64, 1995.

[32] C. Brookes, “The development of water hydraulic pumps using advanced engineering ceramics,” in *Proc. of the 4th Scandinavian Inter. Conf. on Fluid Power*, vol. 26, pp. 965–977, 1995.

[33] G. Lim, P. Chua, and Y. He, “Modern water hydraulics—the new energy-transmission technology in fluid power,” *Applied Energy*, vol. 76, no. 1-3, pp. 239–246, 2003.

[34] M. L. Huber, R. A. Perkins, A. Laesecke, D. G. Friend, J. V. Sengers, M. J. Assael, I. N. Metaxa, E. Vogel, R. Mareš, and K. Miyagawa, “New international formulation for the viscosity of h 2 o,” *Journal of Physical and Chemical Reference Data*, vol. 38, no. 2, pp. 101–125, 2009.

[35] Engineering ToolBox, “Density of liquids versus change in pressure and temperature.” `https://www.engineeringtoolbox.com/fluid-density-temperature-pressure-d_309.html`, 2009.

[36] Engineering ToolBox, "Water - density, specific weight and thermal expansion coefficient." `https://www.engineeringtoolbox.com/water-density-specific-weight-d_595.html`, 2003.

[37] S. Khan, "Calculating the bulk modulus of a fluid." `https://www.maplesoft.com/applications/view.aspx?sid=154172&view=html`, 2006.

[38] W. Wilson, "Rotary-pump theory," *Trans. ASME*, vol. 68, no. 4, pp. 371–384, 1946.

[39] W. E. Wilson, *Positive-displacement pumps and fluid motors.* Pitman Pub. Corp., 1950.

[40] W. Schlosser, "Mathematical model for displacement pumps and motors," *Hydraulic power transmission*, vol. 7, pp. 252–328, 1961.

[41] W. Schlösser, "The overall efficiency of positive-displacement pumps," *Hydraulic pneumatic power*, vol. 15, no. 173, pp. 272–280, 1969.

[42] J. Thoma, "Mathematical models and effective performance of hydrostatic machines and transmissions," *Hydraulic Pneumatic Power*, vol. 23, no. November, pp. 642–651, 1969.

[43] D. McCandlish and R. Dorey, "The mathematical modelling of hydrostatic pumps and motors," *Proceedings of the Institution of Mechanical Engineers, Part B: Management and engineering manufacture*, vol. 198, no. 3, pp. 165–174, 1984.

[44] E. Trostmann, *Water hydraulics control technology.* Routledge, 2019.

[45] G. E. Totten, R. J. Shah, and D. R. Forester, *Fuels and lubricants handbook: technology, properties, performance, and testing.* ASTM International, 2019.

[46] N. Khare, P. Limaye, N. L Soni, and R. J Patel, "Friction and wear characteristics of peek and peek composites in water lubricated slow speed sliding," *Tribology Online*, vol. 10, pp. 84–90, 03 2015.

[47] Minnesota Rubber and QMR Plastics, "Elastomers/materials." `http://www.allsealsinc.com/03_Elastomers-Materials.pdf`, 2003.

[48] Y. Guo, H. Tan, Z. Cao, D. Wang, and S. Zhang, "Mechanical and unlubricated sliding wear properties of nitrile rubber reinforced with micro glass flake," *Polymers*, vol. 10, no. 7, p. 705, 2018.

[49] Bearing Works Inc., *PEEK (Polyetheretherketone) Datasheet*, 8 2016.

[50] University of Minnesota, "Hydraulic diameter for non-circular ducts." `http://www.me.umn.edu/courses/me5341/handouts/essay%209.pdf`, 2009.

[51] J. E. Hesselgreaves, R. Law, and D. Reay, *Compact heat exchangers: selection, design and operation.* Butterworth-Heinemann, 2016.

[52] Christopher E. Brennen, California Institute of Technology, "Couette and planar poiseuille flow." `http://brennen.caltech.edu/fluidbook/basicfluiddynamics/Navierstokesexactsolutions/couetteflow.pdf`, 2006.